核理研研究報告　第33巻　2000年

ISSN 0385-2105

TOHOKU

RESEARCH REPORT OF LABORATORY OF NUCLEAR SCIENCE

Vol.33 2000

TOHOKU UNIVERSITY

Editors

TAMAE, Tadaaki

OHTSUKI, Tsutomu

HAMA, Hiroyuki

Laboratory of Nuclear Science

Tohoku University

1-2-1 Mikamine, Taihaku, Sendai 982-0826

Japan

Pone: +81, 22-743-3400

Fax: +81, 22-743-3401

Web site: http://www.lns.tohoku.ac.jp/

982-0826 仙台市太白区三神峯1-2-1

東北大学大学院理学研究科

附属原子核理学研究施設

電話　022-743-3400

Fax　022-743-3401

Preface

The Laboratory of Nuclear Science (LNS), belonging to the Graduate School of Science, Tohoku University, started in 1966. Since then, it has served as a user's facility available to the scientific community in University, national and international. The basic accelerator of the LNS is a 300-MeV electron linear accelerator (LINAC), which has been working since 1967. In 1995, the construction of a new accelerator which is called 1.2 GeV Stretcher-Booster ring (STB ring) started.

The STB ring was originally designed to be operated under three different modes : (1) the pulse beam stretcher mode, in which a pulsed beam from the LINAC is accepted and a continuous beam is extracted from the STB ring, (2) the booster mode, in which an electron beam from the LINAC is accelerated up to 1.2 GeV, and (3) the storage mode, in which the beam at 1.2 GeV can circulate in the STB ring. The mode (1) is used for low energy (~ 200 MeV) experiments performed at external target stations using the existing experimental equipment such as the large dipole magnetic spectrometer. The mode (2) together with a fast extraction of the beam will be solely used for an injection of a planned 1.8 GeV synchrotron radiation ring which is a future project but not funded, yet. The mode (3) is used for GeV energy nuclear physics experiments performed at an internal target station directly using the circulating beam or at an external target station using GeV tagged photons produced in the ring.

The construction of the STB ring was completed in 1997, and the beam commissioning started. The low energy continuous beam was then available for experiments in 1998. Subsequently the GeV electron beam became available in 1999. Thus, now, the LNS provides continuous electron beams from 0.2 to 1.2 GeV, in addition to the pulsed beams up to 0.25 GeV.

During a period of the construction, no electron beams were available at the LNS except for those with energies below 60 MeV. Some of the nuclear science research have been actively carried out using outside facilities. At the LNS, performed were experiments with various radioactive isotopes produced by low-energy pulsed electron beams from the LINAC. In addition, experiments on low-energy fusion reactions with light nuclei have started by using a low-energy high-current beam generator installed in 1995.

Taking this opportunity of the start of GeV energy experiments, we have decided to modify the quality of this issue 'Research Report of Laboratory of Nuclear Science'. Firstly, the size is changed as you see that new size is the A4 standard. Secondly, in addition to rather complete research reports, short reports which may show the progress of each research annually are encouraged to appear. Thirdly, reports on research activities performed by the LNS staff members but using outside facilities will be also included, in addition to those performed at the LNS by the outside users. Furthermore, writing in English will be more emphasized, although some of the reports were written in English, already, so far.

This issue reports the research activities of the LNS in various fields performed in a fiscal year of 1999 (from April, 1999 to March, 2000), but is the first one after the modification mentioned above. Thus, forms of various reports might not be set to rights. However, we believe the modification contributes to fast exchange of research information, not only domestically but also internationally. We

also believe, the LNS will be successful in promoting productive activities over a variety of nuclear science research fields using electron beams with energies from a few tens of MeV to GeV, high-current keV ion beams and various radioactive isotopes.

Jirohta KASAGI
Director

Research Report of Laboratory of Nuclear Science
Volume 33, 2000

Contents

核理研研究報告　第33巻　目　次

Ⅰ．原子核物理

Ⅱ. 放射化学

Ⅲ. 加速器・放射光

Ⅳ. 平成11年度加速器報告

Ⅴ. 論文リスト

Ⅵ. 課題採択結果

I . Nuclear Physics

Isovector E2/E0 Strength in ^{28}Si Studied by the (e, e'n) Reaction

K. Kino[1], T. Saito[1], T. Nakagawa[1], T. Nakagawa[2] and H.Ueno[3]

[1]*Laboratory of Nuclear Science, Tohoku University, Mikamine, Taihaku-ku, Sendai 982-0826*
[2]*Department of Physics, Tohoku University, Aramaki, Aoba-ku, Sendai 980-8578*
[3]*Department of Physics, Yamagata University, Kojirakawa, Yamagata 990-8560*

We have measured E2/E0 strength in ^{28}Si by the (e, e'n) reaction for excitation energy 20.5~28.0 MeV at three momentum transfers of 0.38, 0.49 and 0.60 fm^{-1}. The E1 and E2/E0 components were separated using the difference of their momentum-transfer dependence. The obtained E1 strength agreed with that of the (γ, n) reaction. A 3.6 MeV wide bump in the E2/E0 component was found at 25.2 MeV. The bump is suggested to be an isovector type comparing the strength of the present work with the isoscalar strength observed in the ^{28}Si(α, α') reaction.

§ 1. Introduction

A systematic study of structures of the giant resonances over the entire nuclei is one of the most important subjects to understand collective behaviors of nucleon many-body systems. However, the isovector giant monopole resonance (GMR) and giant quadrupole resonance (GQR) have not been measured enough especially in light nuclei. The isovector GMR has been tried to measure through many reactions [1-6], and ($\pi^{\pm}$, π^{0}) [1] and (^{7}Li, ^{7}Be) [4] experiments have provided reliable data. The isovector GQR has been mainly studied by the (e, e') reaction[7]. In spite of these experimental efforts, data for light nuclei is still scarce. The higher energy and broader width of the isovector GMR and GQR in light nuclei, which may hide the resonances in the nonresonant processes, make it difficult to investigate them.

Recent ^{28}Si(e, e'α) and ^{28}Si(e, e'p) experiments[8] have reported excessive E2/E0 strength in the excitation energy region just above the isoscalar GMR and GQR and it came to be the isovector E2/E0. On the other hand, the excitation energy of the isovector GMR and GQR accumulated from the data for middle-heavy and heavy nuclei are suggested to be more than 34 MeV which are much higher than the isoscalar ones. In this paper, we report an isovector E2/E0 component of ^{28}Si studied by the (e, e'n) reaction in order to research the isovector GMR and GQR in light nuclei.

We used the (e, e'n) reaction because it has some advantages for studying giant resonances. First, the electron scattering is able to choose momentum transfer independently against excitation energy and components of different multipoles could be separated. Second, the neutron coincidence measurement under the present condition of electron scattering, in which the longitudinal component of virtual photons is dominant, gives little contribution from the direct-knockout process and provides more promising data for study of the giant resonances.

§ 2. Experiment

The measurement has been performed using the continuous electron beam from the Stretcher Booster Ring at Laboratory of Nuclear Science of Tohoku University. A target of chemically pure silicon with thickness of 118.8 mg/cm^2 was used. Scattered electrons were momentum-analyzed using a magnetic spectrometer and detected by a combination of a vertical drift chamber and plastic scintillators. Emitted neutrons were measured using eight NE213 liquid scintillation detectors, which were placed at θ_n=58°, 83°, 108°, 133°, 158°, 213°, 238° and 263°. The detectors were shielded by concrete, paraffin and lead from the huge amount of-ray and neutrons in the experimental hall. Each detector was 0.85cm distant from the center of the scattering chamber allowing the neutron energy to be determined by the TOF method. The excitation energy spectra for ω=20.5~28.0 MeV were measured at a scattering angle of θ_e=28° at incident energies of 149.5 and 197.5 MeV and at θ_e=35° at an incident energy of 197.5 MeV corresponding to the momentum transfers of 0.38, 0.49 and 0.60 fm^{-1}, respectively.

§ 3. Results and Discussion

Figure 1 shows an example of the missing energy spectrum. The neutron decay from the giant resonance region in ^{28}Si was dominantly through n_0, n_1 and n_2 channels where n_0, n_1 and n_2 correspond to neutron decay to the 5/2$^+$ ground state, 1/2$^+$ first and 3/2$^+$ second excited states, respectively, in the residual nucleus ^{27}Si. In the analysis n_0, n_1 and n_2 have been treated together because the energy resolution of the missing energy spectra is insufficient to separate them.

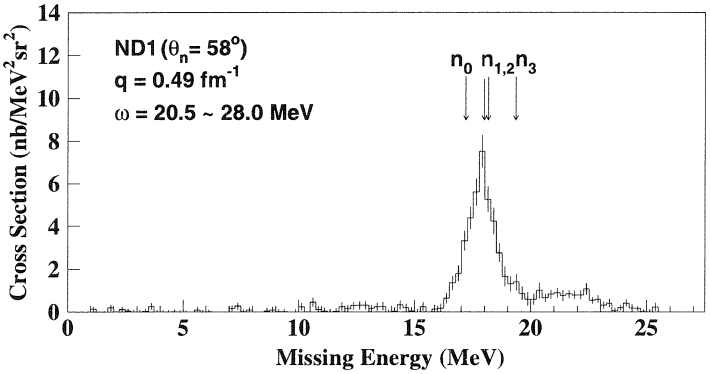

Fig.1. A typical missing energy spectrum of the ^{28}Si(e, e'n) reaction.

The ^{28}Si(e, e'n$_{0+1+2}$) reaction cross sections for each excitation energy under the three different momentum transfers were obtained. The E1, E2 and E0 excitations are expected to be dominant under the present experimental condition. The E1 and E2/E0 components were separated using their momentum-transfer dependence assuming the following :

$$|F(q,\omega)|^2 = a_{E1}(\omega) \cdot |F_{E1}(q)|^2 + a_{E2/E0}(\omega) \cdot |F_{E2/E0}(q)|^2 \quad (1)$$

Here, $a_{E1}(\omega)$ and $a_{E2/E0}(\omega)$ are strength of E1 and E2/E0 components at excitation energy ω. The momentum-transfer dependence of the form factors, $|F_{E1}(q)|^2$ and $|F_{E2/E0}(q)|^2$, were obtained from the

Goldhaber-Teller[9] and Tassie[10] models, respectively. The momentum-transfer dependence of E0 is too similar to the E2's to distinguish them. Figure 2 shows the decomposed form factors into the E1 and E2/E0 components.

The obtained E1 and E2/E0 components are shown in Fig.3. The E1 strength for the (e, e'n_{0+1+2}) reaction agrees well with that for the (γ, n_{total}) reaction at $\omega \leq 23$ MeV. The form factor of the E1 component for the (γ, n_{total}) reaction was derived under the assumption that the (γ, n_{total}) reaction is dominated by E1 and the Goldhaber-Teller model was used to reduce the form factor at the same momentum transfer of the present work. A disagreement between the (e, e'n_{0+1+2}) and (γ, n_{total}) reactions at $\omega \geq 24$ MeV seems to be due to the contributions of decay processes to highly excited states.

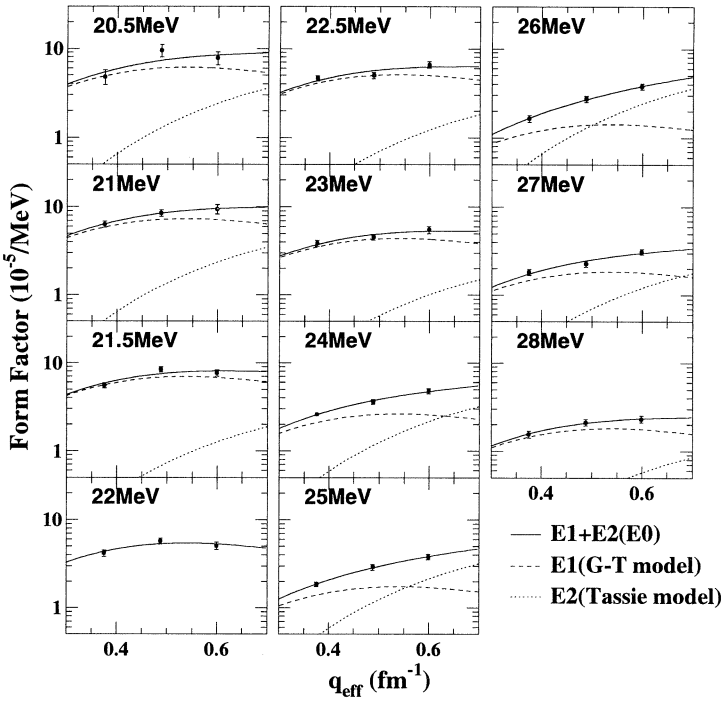

Fig.2. Decomposition of the form factor into E1 and E2/E0 components. Dashed lines are E1 components and dotted lines are E2/E0 ones.

In the E2/E0 component we found a bump with a width of 3.6 MeV at 25.2 MeV. Figure 4 is a comparison of the present E2/E0 strength with the isoscalar GMR and GQR strength for the ^{28}Si(α, α') reaction[11]. The observed E2/E0 spectrum tends to decrease from ω=20.5 to 22.0 MeV and resembles to the isoscalar GQR strength by the (α,α') reaction. Compared with electron scattering, it is more similar to the (e, e'α) spectrum[8] which contains mainly isoscalar strength than to the (e, e'p)'s[8]. According to this result, the structure below 22.0 MeV of present work seems to reflect the isoscalar GQR. The bump found at 25.2 MeV was interpreted to be isovector type because there seems to be no structure in the isoscalar strength at the same excitation energy. This interpretation is consistent with the observed isovector strength above 25 MeV in the ^{28}Si(^{7}Li,^{7}Be)^{28}Al reaction[12] as seen in Fig.5. The strength of the ^{28}Si(^{7}Li,^{7}Be)^{28}Al reaction in the figure is the ΔS=0 component of that reaction and the contribution of the GDR has been already subtracted.

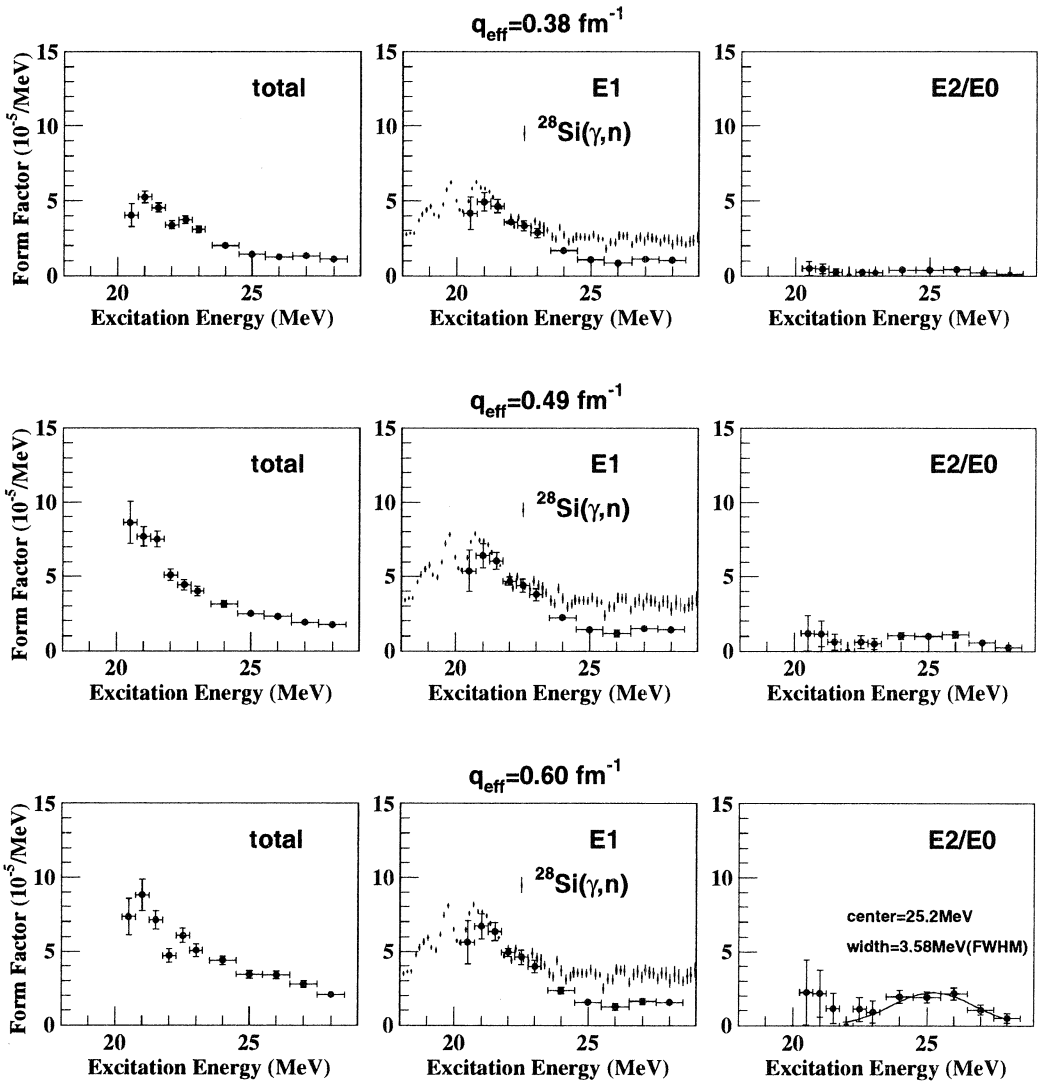

Fig.3. Result of the decomposition of Fig.2. The left side is the obtained form factor and the center and the right side are the decomposed E1 and E2/E0 form factors, respectively. The ^{28}Si(γ , n) data in the center is the deduced form factor using the Goldhaber-Teller model[9] from the ^{28}Si(γ , n_{total}) reaction[13].

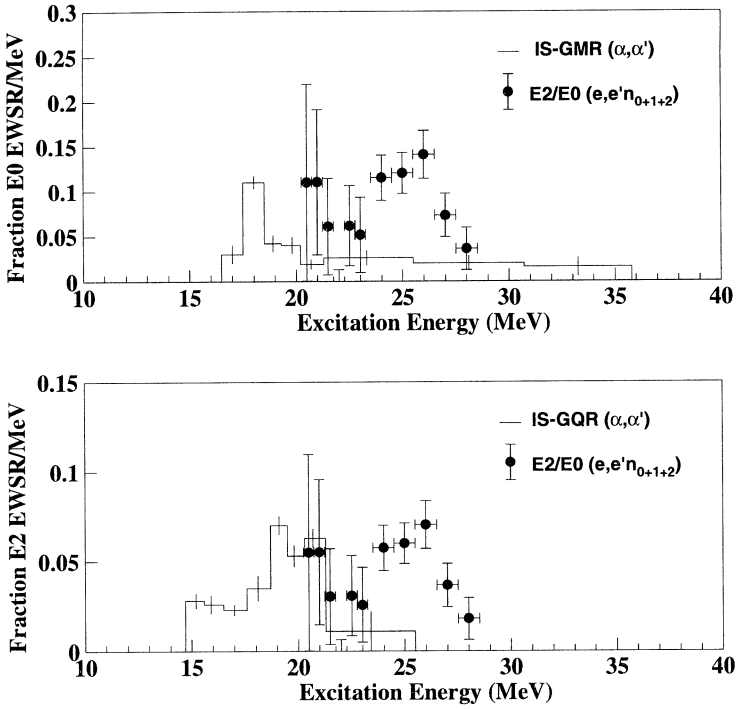

Fig.4. Comparison of the present E2/E0 strength with the isoscalar strengths by the ^{28}Si(α, α') reaction[11].

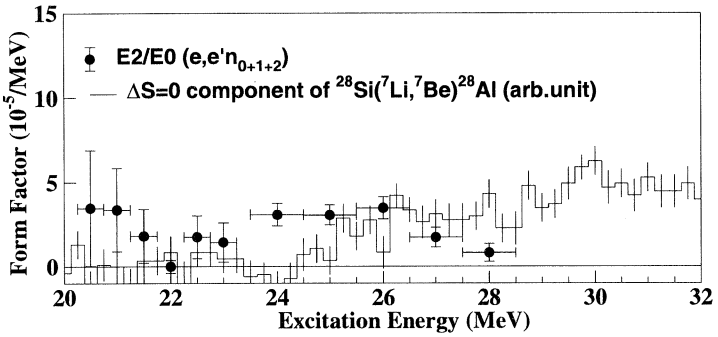

Fig.5. Comparison of the present E2 /E0 strength with the $\Delta S = 0$ strength of the ^{28}Si(^{7}Li,^{7}Be)^{28}Al experiment[12]. The contribution of the GDR has been subtracted in the latter.

The obtained strength in EWSR [14] of the bump are listed in Table 1 for the cases of E0 and E2. If it is assumed to be fully E0 strength or fully E2 strength, it exhausts 46.9% of the isovector E0 EWSR or 23.4% of the isovector E2 EWSR. However, we must notice that the isoscalar GMR contains some strength in the higher excitation energy as known in Fig.4 and the (e, e'n) reaction is sensitive equally to isoscalar and isovector.

We found an existence of the isovector E2/E0 strength in ^{28}Si at lower excitation energy than the extrapolation by the data of middle-heavy and heavy nuclei. However, in order to manifest the entire structure of the isovector GMR and GQR, a measurement through the (e, e'n) reaction at higher excitation energy is desired.

Table 1. Strength of the ^{28}Si(e, e′n_{0+1+2}) reaction in EWSR. Errors are statistical only.

	EWSR (e^2fm^4MeV)	Present work $\omega=22.5\sim28.0$ MeV (e^2fm^4MeV)	Ratio (%)
Isovector E0	5497	2570 ($\pm$300)	46.9 ($\pm$5.4)
Isovector E2	5468	1280 ($\pm$150)	23.4 ($\pm$2.7)

§ 4. Conclusion

The ^{28}Si(e, e′n_{0+1+2}) cross section has been measured at $\omega=20.5\sim28.0$ MeV and $q=0.38$, 0.49 and 0.60 fm^{-1}. The n_0, n_1 and n_2 decay were dominant. E1 and E2/E0 components at each excitation energy were separated using a difference in momentum-transfer dependence. The obtained E1 strength and structure were in agreement with those of the (γ, n_{total}). A 3.6 MeV wide bump was found at $\omega=25.2$ MeV in the E2/E0 component. It was interpreted to be isovector type because no such bump is seen in the isoscalar GMR and GQR strength obtained by the ^{28}Si(α,α') reaction. The present strength exhausts 46.9% isovector E0 EWSR or 23.4% isovector E2 EWSR.

We would like to thank the linac crew of the Laboratory of Nuclear Science of Tohoku University for providing high quality electron beam.

References

[1] A. Erell, J. Alster, J. Lichtenstadt, and M.A. Moinester : Phys. Rev. C**34** (1986) 1822.

[2] T.D. Ford *et al.* : Phys. Lett. **B195** (1987) 311.

[3] I. Lhenry : Nucl. Phys. **A599** (1996) 245c.

[4] S. Nakayama *et al.* : Phys. Rev. Lett. **83** (1999) 690.

[5] R.G.T. Zegers *et al.* : Phys. Rev. C**61** (2000) 054602.

[6] R.G.T. Zegers *et al.* : Phys. Rev. Lett. **84** (2000) 3779.

[7] A. van der Woude, in *Electric and Magnetic Giant Resonances in Nuclei in International Review Nuclear Physics Vol 7, 1991,* edited by J. Speth (World Scientific Publishing Company, Singapole 1991), p. 185.

[8] Th. Kihm *et al.* : Phys. Rev. Lett. **56** (1986) 2789.

[9] M. Goldhaber and E. Teller : Phys. Rev. **74** (1948) 1046.

[10] L.J. Tassie : Aust. J. Phys. **9** (1956) 407.

[11] D.H. Youngblood, H.L. Clark and Y.W. Lui : Phys. Rev. C**57** (1998) 1134.

[12] S. Nakayama *et al.* : Phys. Rev. C**46** (1992) 1667.

[13] J.T. Caldwell, R.R. Harvey, R.L. Bramblett and S.C. Fultz : Phys. Lett. **6** (1963) 213.

[14] S. Kamerdzhiev, J. Speth and G. Tertychny : Nucl. Phys. **A624** (1997) 328.

Study of ^{12}C(e, e′p) Reaction at an Energy Transfer of 60 MeV

Y. Sato[1], T. Tamae[1], T. Yokokawa[1]*, Y. Asano[1], K. Hirota[1], M. Kawabata[1]†, R. Kimura[2], O. Konno[1]‡, H. Miyase[2], I. Nakagawa[1]§, I. Nishikawa[1], H. Tsubota[2] and H. Yamazaki[1]

[1]*Laboratory of Nuclear Science, Tohoku University, Mikamine, Taihaku-ku, Sendai 982-0826*
[2]*Physics Department, Graduate School of Science, Tohoku University, Aramaki, Aoba-ku, Sendai 980-0845*

The (e, e′p) cross section has been measured at an energy transfer of 60 MeV and a momentum transfer of 104.1 MeV/c, using a 197 MeV continuous electron beam. The reduced cross section at missing momenta between 81.3 and 321.2 MeV/c obtained from the experiment is compared with a distorted-wave impulse approximation (DWIA) in a reasonable agreement. This result demonstrates a high reliability of the DWIA calculation in this energy region, and supports the discussion that a large difference between the experimental data and the DWIA calculation in the (γ, p) reaction is related to the non-nucleonic degrees of freedom such as meson exchange currents.

§ 1. Introduction

In the quasi-elastic region, the (e, e′p) reaction is well understood in the framework of the direct-knockout (DKO) model. This model is based on an assumption that a virtual photon couples to a single proton in a target nucleus. On the other hand, for the photo-nuclear reaction in the energy region of E_γ = 60～100 MeV, contributions of the meson exchange currents (MEC) are known to be large. However, there is another argument [2,3] that in this region the contribution of the the DKO to the photo-nuclear reaction is as large as to the quasi-elastic (e, e′p) reaction.

Ireland and Steenhoven [4] discussed the contribution of the MEC's in the (γ, p) reaction by comparing the quasi-elastic (e, e′p) and (γ, p) reactions in the same framework. The DKO calculation for the (γ, p) reaction underestimated the data by a factor of 6. They explained this discrepancy from the contribution of the MEC's; the real photon, which contributes the (γ, p) reaction, has only a transverse component and interacts with the MEC's, whereas the virtual photon in the (e, e′p) reaction has a large longitudinal component, which interacts with a charge of the nucleon. Quasi-elastic (e, e′p) and (γ, p) data they used in their discussion, however, were much different in the kinematical condition, i.e. different energies and different momentum transfers. It means the DKO calculation of both reactions can not always be dealt with the same framework. They mentioned the importance of (e, e′p) and (γ, p) reactions in the same kinematical condition for isolation of the MEC's. Very recently there has been another argument [5] that meason exchange current contributions may not be large

*Present address : Iwanami Shoten Publishers, 2-5-5 Hitotsubashi, Chiyoda-ku, Tokyo 101-8002.
†Present address : Department of Physics, School of Science, Osaka University, Toyonaka, Osaka 560-0043.
‡Department of Electrical Engineering, Ichinoseki National College of Technology, Hagiso, Ichinoseki 021-8511.
§Present address : Laboratory of Nuclear Science, MIT, Cambridge, MA 02139, USA.

when treated in a relativistic framework. Thus the (e,e'p) experiment in the kinematical condition close to the (γ, p) experiment is important to resolve this long-standing problem. Several years ago we measured the cross section of the ^{12}C(e, e'p) reaction in a low energy region (ω = 40 MeV, q = 69 and 129 MeV/c), and compared with the DWIA calculation [6]. Although the DWIA calculation with specific sets of optical potential parameters accounted for the measured cross section, the calculated values considerably diverge for choice of parameters. In the present experiment, we chose the transferred energy to be 60 MeV, same energy as in the photo-reaction; the final state interaction is expected to be same for both of the (e, e'p) and photo-reactions.

§ 2. Experimental Procedure

The experiment was performed using a 197 MeV continuous electron beam from a stretcher-booster ring (STB). Electrons scattered with a 9.2 mg/cm^2-thick natural carbon foil were analyzed with a magnetic spectrometer (LDM) at 30°. A missing energy was set at ω = 60 MeV. A corresponding momentum transfer is 104.07 MeV/c. Ejected protons were measured with SSD counter telescopes composed of four SSD's (one 50 μm and three 1 mm) at nine angles out of the scattering plane (ϕ_p = 90°). A 3 mm-thick aluminum disk was installed in front of each telescope, in order to degrade the energy of particles. The thickness was optimized so that the highest resolution was achieved for measurement of the particle energy.

Because of a trouble on data acquisition of a vertical drift-chamber (VDC), we used information of time difference of signals at both ends of back-up scintillators to fix the momentum of scattered electrons. The resulting energy resolution in missing energy spectra, about 3 MeV at FWHM, is not enough to separate the (e, e'p$_0$) and the (e, e'p$_1$) events. Events for $E_m \leq 17.5$ MeV have been treated as (e, e'p$_0$) events. An error caused by the separation is estimated as about 10% for the (e, e'p$_0$) reaction from fitting with Gaussian curves.

§ 3. Results and Discussion

The measured cross sections and corresponding reduced cross sections are listed in Table 1. In the plane-wave impulse-approximation (PWIA), the (e, e'p) cross section can be factorized in the form :

$$\sigma_{e,e'p} = K \sigma_{e,p} \rho_{e,e'p}(p_m), \tag{3.1}$$

where K is a kinematic factor and $\sigma_{e,p}$ is the off-shell electron-proton scattering cross section [7]. The reduced cross section $\rho_{e,e'p}(p_m) \equiv |f(p_m)|^2$ is referred as the momentum distribution of the proton in the nucleus.

Open squares in Fig.1 show the reduced cross sections obtained from the present experiment; closed triangles and closed circles are the results of the (e, e'p) experiment [8] in quasi-elascitc scattering and the (γ, p) experiment [4], respectively. In the figure, results of the DWIA calculation made for the present experiment using three sets of optical-potential parameters [9-11] are also shown; the parameters are listed in Table 2. The parameter set in ref. [10] was used also in the calculation for the (γ, p) experiment [4] . The calculations agree with the experimental results within a factor of two; this agreement appears to be better than for the previous experiment [6] made at a transferred energy

Table 1. Differential cross section and reduced cross section of the $^{12}C(e, e'p_0)$ reaction.

(θ_p, ϕ_p)	p_m (MeV/c)	Differential Cross Section (nb/MeV/sr^2)	Reduced Cross Section $\rho(p_m)$ (MeV/c)$^{-3}$
(0°, −)	181.33	11.08±0.80	(3.19±0.23)×10^{-9}
(12°, 90°)	184.67	9.69±0.75	(2.79±0.22)×10^{-9}
(24°, 90°)	194.19	7.67±0.67	(2.21±0.19)×10^{-9}
(36°, 90°)	208.59	4.27±0.50	(1.23±0.15)×10^{-9}
(48°, 90°)	226.30	3.13±0.57	(9.06±1.64)×10^{-10}
(72°, 90°)	265.94	0.430±0.147	(1.25±0.43)×10^{-10}
(84°, 90°)	285.66	0.330±0.140	(9.62±4.11)×10^{-11}
(96°, 90°)	304.26	0.371±0.166	(1.10±0.49)×10^{-10}
(108°, 90°)	321.19	0.202±0.147	(6.04±4.38)×10^{-11}

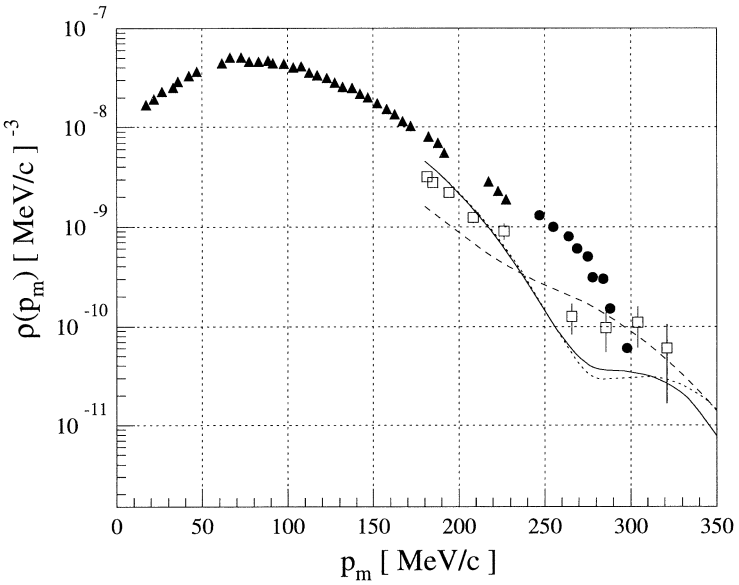

Fig.1. Reduced cross sections of $^{12}C(e, e'p)$ and (γ, p) reactions. Closed triangles represent the data of the quasi-elastic (e, e'p) reaction[8]. Closed circles are data from (γ, p) reaction[4]. Open squares show the results of the present (e, e'p) experiment, and lines are results of the DWIA calculation corresponding to the present kinematics: solid line (ref. [9]), dashed line (ref. [10]), dotted line (ref. [11]).

of 40 MeV.

The result of the present experiment that the (e, e'p) cross section is reasonably described by the DWIA calculation at ω = 60 MeV supports the argument that a large difference between the data and the DWIA calculation in the (γ, p) experiment must be an evidence of the MEC's. The relativistic calculation is under way to give a solution to the longstanding discussion.

We wish to thank the accelerator group and the computer group for their assistance during the measurements. We also express our thanks Mr. K. Matsuda for his help in manufacturing detector holders. We would like to thank Dr. C. Giusti and Dr. G. van der Steenhoven for helping us to carry out the DWIA calculation with the computer code DWEEPY. We also thank Dr. H. Sherif and Dr. J. Johansson for their discussion on the relativistic calculation.

Table 2. Parameters of the optical potentials used in the DWIA calculation.

	ref. [9]	ref. [10]	ref. [11]
V (MeV)	38.0	39.30	38.60
r_0 (fm)	1.2	1.20	1.15
a_0 (fm)	0.5	0.61	0.73
W (MeV)	11.0	6.23	7.15
r_W (fm)	1.2	1.40	1.25
a_W (fm)	0.5	0.69	0.44
V_{ls} (MeV)		21.50	0.75
r_{ls}(fm)		1.00	0.75
a_{ls} (fm)		0.65	0.07

References

[1] J.R.M. Annand *et al.,* Phys. Rev. lett. **71** (1993) 2703.

[2] S. Boffi, R. Cenni, C. Giusti and F.D. Pacati, Nucl. Phys. **A420** (1984) 38.

[3] G. Benenti, C. Giusti and F.D. Pacati, Nucl. Phys. **A574** (1994) 716.

[4] D.G. Ireland and G. van der Steenhoven, Phys. Rev. C**49** (1994) 2182.

[5] J.I. Johansson and H.S Sherif, Rhys. Rev **56** (1997) 328.

[6] I. Nakagawa *et al.,* Research Report of LNS, Tohoku Univ. **29** (1996) 21.

[7] M. Cavinato, M. Marangoni, and A.M. Sarius Z. phys. A-Atoms Nuclei **335** (1990) 401.

[8] G. van der Steenhoven *et al.,* Nucl. Phys. **A480** (1988) 547.

[9] H.G. Pugh *et al.,* Phys. Rev. **155** (1967)1054.

[10] J.R. Comfort and B.C. Karp, Phys. Rev. C**21** (1980) 2162.

[11] J.A. Fannon *et al.,* Nucl. **A97** (1967) 263.

Strongly Enhanced DD Fusion Reactions at Very Low Energies in Solids

H.Yuki, T. Baba, T. Noda, T. Ohtsuki, A. Lipso and J. Kasagi

Laboratory of Nuclear Science, Tohoku University, Mikamine, Taihaku, Sendai 982-0826

Abstract : The interplay between a nucleus and its environment is known to play an important role in nuclear reactions when the incident energy has been reduced far below the Coulomb barrier, where the cross section described by the Gamow function decreases drastically due to the steep drop in the quantum mechanical penetration of the barrier. For the fusion reactions in metals, experimental techniques were developed in which target nuclei were implanted in a metal. The DD fusion reactions were studied, so far, and an enhancement in the rate of the D(d, p)T fusion reaction over the Gamow function was found for deuterons in Ti and Yb. Here we report on further measurements of the D+D reactions in other materials. Of particular interest is the fact that the reaction rate of the D+D reactions at 2.5 keV in PdO is 50 times larger than in Ti, and the deduced screening potential amounts to 600 eV. This cannot be explained by bound-electron screening which may give a potential of 20 eV at most, but suggests the existence of an additional, and important, mechanism. Perhaps there is a fluidity of deuterons in metals that also reduces the Coulomb barrier between the interacting deuteron pair. An exhaustive study of nuclear reactions in metal would be very significant ; one would then not only simulate nuclear fusion reactions in a stellar plasma where the nuclei are immersed in a sea of electrons, but also explore the limitations of nuclear fusion at room temperature.

§ 1. Introduction

Low-energy nuclear reactions with light nuclei have shown that the cross sections are affected by electrons surrounding the interacting nuclei[1-5]. These cross sections are somewhat larger than those of bare nuclei without electrons. The enhancement is called the electron screening effect and is described quantitatively by the screening potential U_s. The greater the enhancement, the larger the value of U_s is. For the D+D reaction with a gas target, the screening potential was deduced as U_s = 25 $\pm$5 eV[3] by comparing the experimental cross section with the prediction based on the Gamow function and the parameterization of ref [6].

For the nuclear reactions in metals, experimental techniques were developed in which target nuclei were implanted in a metal[7,8]. The screening potential in a metal was first deduced for the D+D reaction in Ti by measuring the proton yield in the D (d,p) T reaction[9]. The result, U_s = 19 $\pm$12 eV, is almost the same as for the gas target. For the subsequent measurement with Yb, however, U_s = 81 $\pm$10 eV was deduced[10] ; this is certainly larger than expected for deuterium atom and molecule [11]. Thus, we have continued the measurements for various metals to find the mechanism of the enhancement as well as to look for more favorable metal for the DD fusion reaction. In the present work, we report on a series of the measurements of the D(d,p)T reactions in PdO, Pd, Fe, Au and Ti for 2.5 < E_d < 10 keV.

§ 2. Experimental Procedure

The measurements were performed using a low-energy ion beam generator[9]. A deuteron beam intensity of several hundred mA was collimated by passing through two slits so as to fix the beam position and size; the beam spot on the target was 4 mm in diameter.

For the DD fusion reactions, foils of Ti, Fe, Pd, Au and PdO/Pd/Au were bombarded. Commercially available metallic foils with thickness of 0.2 to 1 mm were bombarded as targets. They were annealed in vacuum at about 800℃ for several hours. The PdO/Pd/Au foil was prepared in such a way that a rolled Pd foil with thickness of 40-50 mm was annealed in an oxygen flame at about 1000℃ and Au was electrochemically deposited on one side of the foil.

The PdO surface side was bombarded and the thickness of PdO layer measured by the SEM technique was about 30 nm. The targets were cooled during the bombardments by liquid nitrogen and the temperature of the foil surface was monitored by a thermocouple. The total dose of the deuteron beam was deduced from the electric current on the target, with a small correction for secondary electron emission.

In order to detect protons emitted in the D(d,p)T reactions, a ΔE-E counter telescope consisting of 50- and 200-μm thick Si surface barrier detectors was used. The front face of the ΔE detector was covered with a 15-μm thick Al foil to prevent electrons and scattered deuterons from hitting the detector. The telescope was placed at 2cm from the target and at 90° to the beam direction. Requiring a coincidence between the ΔE and E detectors completely eliminated electrical noise and enabled unambiguous identification of protons from the D (d,p)T reaction.

§ 3. Behavior of Deuterons in Solids during the Bombardment

The proton yield is proportional to the number of projectiles and targets as well as the reaction cross section. In the present case, deuterons impinging upon the metal play a dual role, projectiles and targets of the reaction. Since the fusion enhancement factors we seek are obtained from only the energy dependence of the proton yield, it is not necessary to know the absolute number of targets. But it is necessary to keep that number reasonably constant as the deuteron energy is varied. Hence, a method for controlling the number of target deuterons had to be developed.

We have measured the proton yield from the D(d,p)T reaction in our targets under various conditions and deduced the dependence of the number of targets on the deuteron dose, metal temperature and beam current. Furthermore, deuterium depth profiles were obtained by the elastic recoil detection method[12] for 5 keV deuteron implantation into Pd and PdO.

Here, we briefly show the important results concerning the number of the target deuterons during the bombardment. (1) The number of the target deuterons increases when the metal foil does not contain deuterium initially, and at a certain fluence reaches saturation, in confirmation of that reported in ref [13]. (2) The saturation number of deuterons depends strongly on both the host metal and on the temperature, as shown in Fig.1, where the proton yields versus target temperature are plotted for a deuteron bombardment energy of 10 keV. In general, the larger the fluidity of the deuteron is, the smaller the number becomes. (3) The depth profiles of deuterons implanted into Pd and PdO show

that the deuteron density increases with depth into the surface and saturates at a depth being much greater than the range of the bombarded deuteron.

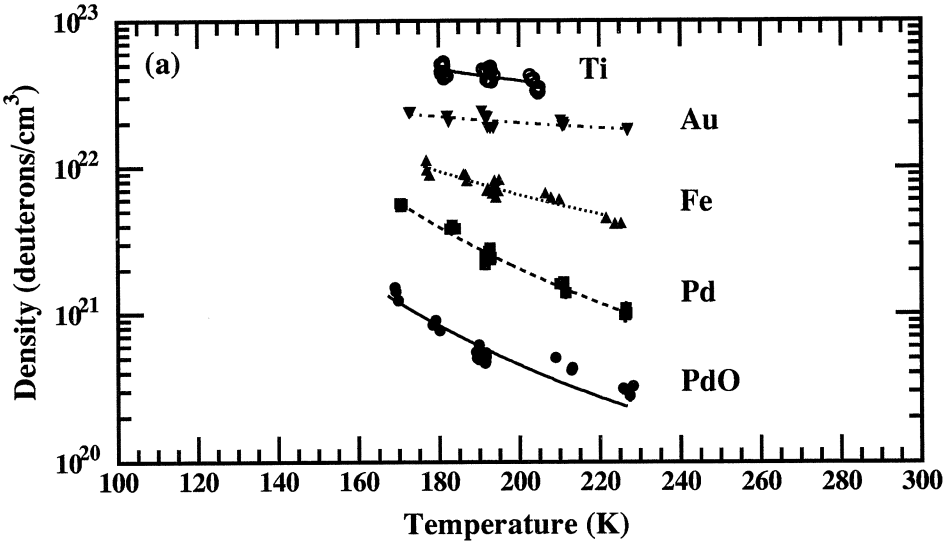

Fig.1. Saturation density of deuterons versus target temperature.

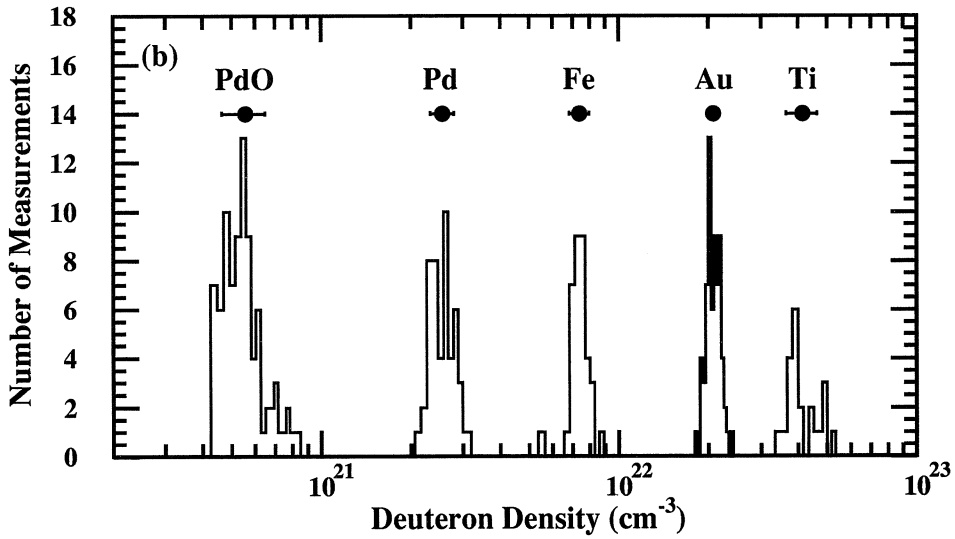

Fig.2. Stability of deuteron density in various metals during the bombardments.

Therefore, the measurements of the excitation function of the D(d,p)T reaction in metal have been carried out by controlling and monitoring the number of the target deuterons as follows.

Prior to the measurement, the metal foil was bombarded by 10 keV deuterons with a beam current of 60 μA until the proton yield together with the temperature of the metal becomes constant. This basically ensures the saturated condition on the deuterium concentration at the equilibrium temperature; we always confirmed that proton emission rate converged to nearly same number whether initially the foil contained no deuterons or was full of them. At other bombarding energies, the beam current must be adjusted so as to keep the input power (and, hence, the temperature) constant; the temperature of the target was always monitored. In this way, the number of target deuterons was hold constant during the measurement. Nevertheless, the proton yield at 10 keV was measured at frequent intervals to verify this constancy. During the accumulation of the data at 2.5 keV, for example, such measurements were carried out more than ten times (a few minutes at 10 keV, a few hours at 2.5 keV, again and again). The proton yield is, then, always divided by the yield at 10 keV measured just before and after the run. This procedure of normalization gives the relative reaction rate as a function of the bombarding energy.

In order to examine the stability of the deuteron target density during the measurements, we show, in Fig.2, a histogram of the deuteron density in metal deduced from the frequent measurements at 10 keV, 22 times for Ti, for example, by using the cross section of the bare D(d,p)T reaction [6] and assuming the constant density distribution for deuterons. Solid circles plotted at the upper part show the most probable values with a one standard deviation error. It should be emphasized that the deuteron density is very stable during the measurements; the values scatters only within 20% even for the high fluidity host materials, PdO and Pd. The present method of sampling the deuteron density is justified by the fact that the effective depth contributing to the D+D reaction is very small (5 nm for 2.5 keV and 15 nm for 10 keV, for Pd metal) and more than 70% of the yield at 10 keV originates from the first 5 nm layar.

§ 4. Reaction Rates

In the upper half of Fig.3, plotted are the relative yields of the D(d,p)T reaction in metals against the bombarding energy. Figure 3 (a) shows results of two independent measurements for PdO, Fig.3 (b) results for Pd and Fe, and Fig.3 (c) for Au and Ti. As expected from the bare D+D reaction, the yields decrease very rapidly as the bombarding energy decreases. However, it is clearly seen that the yield at lower energies very much depends on the host metal ; the largest yield is observed in PdO followed by Pd, Fe, Au and Ti, in order. Since the projectile deuterons are slowed down in the metal and the reactions can occur until the deuteron stops, the observed proton yield Yp at the bombarding energy Ed (the thick target yield) isgiven by

$$Y_p = A \int N_D(x)\, \sigma(E)\, (dE/dx)^{-1}\, dE ,$$

where $N_D(x)$, $\sigma(E)$ and dE/dx are number density of target deuterons as a function of depth beneath the

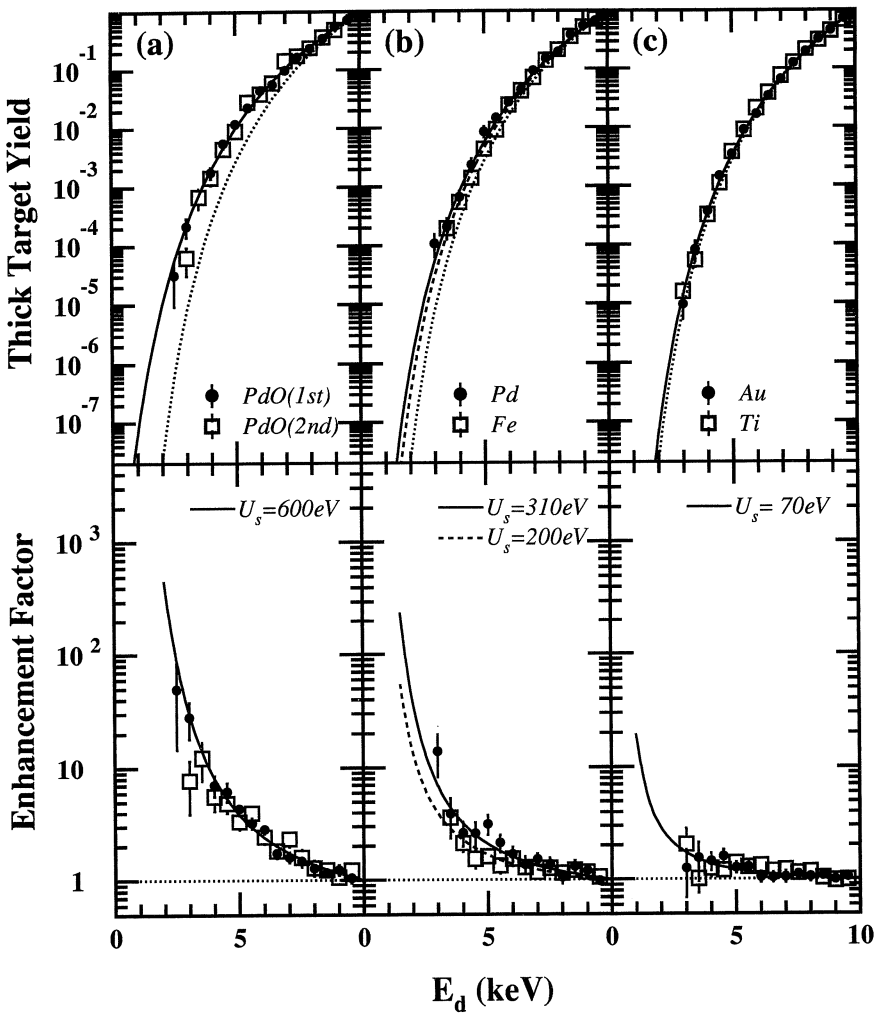

Fig.3. Relative yields of the D (d,p)T reaction in metals against the bombarding energy. In the lower part, the ratios of the experimental yield to the standard calculation are shown.

surface, the reaction cross section and the energy dependent stopping power for the deuteron, respectively. The solid line in Fig.3 indicates a standard thick target yield corresponding to the bare D+D reaction, *i.e.,* without any enhancement of the reaction rate.

In the calculation, constant target density is assumed for $N_D(x)$ and the parameterization of Bosch and Hale [6] is used for σ(E). Further, the graphs of dE/dx vs. E of Anderson and Ziegler [14] are employed. Their assumption that the electronic stopping power is proportional to the projectile velocity at low energies has been confirmed down to deuteron energies as low as 1 keV for various metals [15]. As seen in Fig.3, the standard calculation without any enhancement completely fails to explain the data at the lower energies, especially for PdO, Pd and Fe.

In the lower part of Fig.3, we plot the ratio of the experimental yield to the standard calculation (no enhancement) in order to make comparisons more clearly. As seen, the reaction rate in PdO is enhanced very much, about 50 times larger than the standard at E_d = 2.5 keV. On the other hand, the deduced enhancement is very small for Au and Ti. Since the fact that the enhancement increases as the bombarding energy decreases is a feature of the reaction characterized with a screened Coulomb potential [16], we have naively attempted to parameterize the enhanced reaction rate by a screening

potential (U_s) which reduces the Coulomb barrier between two deuterons. The cross section $\sigma_b(E)$ of the fusion reaction between bare nuclei can be expressed as sb $\sigma_b(E) = SE^{-1} \exp(-2\pi\eta)$, where S is the astrophysical S-factor and $2\pi\eta = 2\pi Z_1 Z_2 \alpha (\mu/2E)^{1/2}$ is the Sommerfeld parameter (Z_1 and Z_2 = atomic numbers of the interacting nuclei, μ = reduced mass and E = center-of-mass energy). The penetration through a screened Coulomb barrier at projectile energy E is equivalent to that of bare nuclei at energy $E_{eff} = E + U_s$ and thus the fusion cross section increases as ss $\sigma_s(E) = \sigma_b(E_{eff})$.

We calculated thick target yields for various values of U_s as described in [9], and determined the values of Us to give the best fits to the enhancement factor data. These fits are shown by the curves in Fig.2. The results are U = 600 ± 20, 310± 20, 200 ± 15, 70 ± 10 and 65 ±10 eV, respectively, for PdO, Pd, Fe, Au and Ti. The errors only include the statistical ones. Systematic errors originate from various sources : uncertainty of the bombarding enegy ± 13 eV), fluctuation of the deuteron density (±60 eV for PdO, ±30 eV for Pd, ±20 eV for Fe and Ti and ±10 eV for Au), uncertainty of the depth dependence of the deuteron density (+20 eV) and ambiguity of the stopping power (±30 eV).

§ 5. Discussion

Since the screening potential caused by electrons in metal is only several tens of eV [17], the presently deduced values for PdO, Pd and Fe can never be due to the electron screening alone. Of

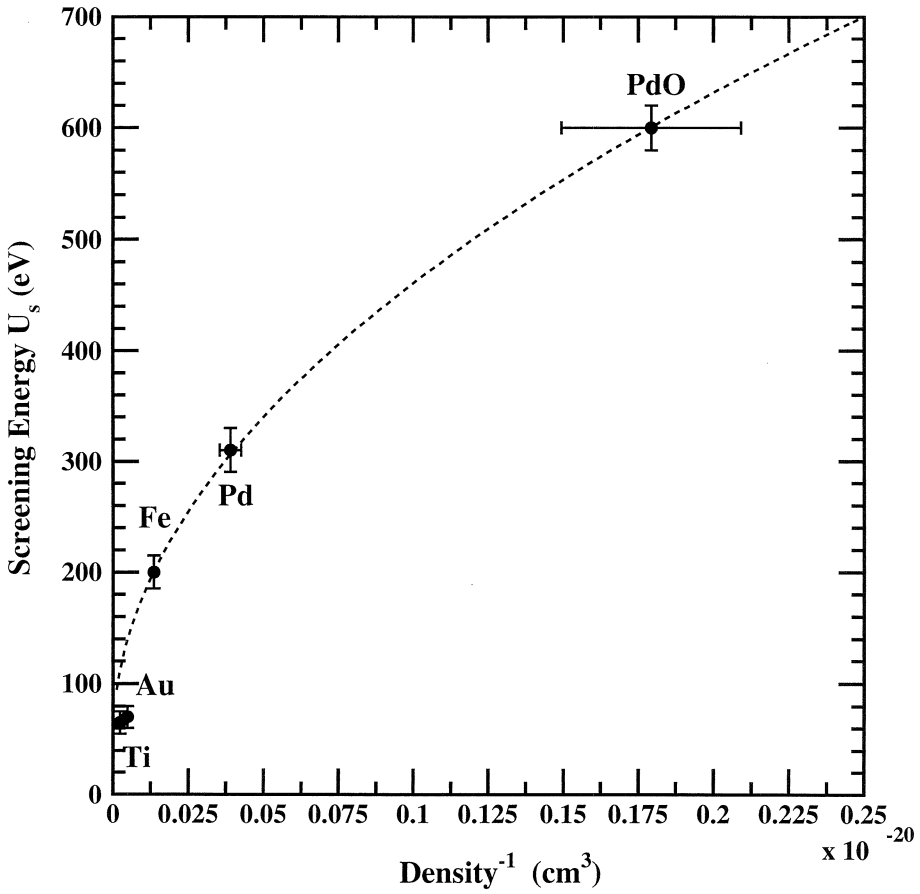

Fig.4. Deduced screening potential versus (deuteron density)$^{-1}$.

particular interest is the existence of a strong correlation between the screening potential and the deuteron density in metal during the bombardment, as shown in Fig.4, where the deduced screening potentials are plotted against (density)$^{-1}$. The deuteron density during the bombardment is an index of the fluidity of deuteron; it might be proportional to the inverse of the density. Thus, we infer that for the D+D reaction in metal at very low energies there exists a significant screening mechanism, the effect of which increases drastically with an increase of the fluidity of deuteron in metal, in addition to the electron screening known previously.

For Pd metal, the deuteron density during the bombardment is much lower than that achieved in electrochemical loading, where atomic ratio D/Pd becomes 0.95. This peculiarity may be connected with deuterium diffusivity in metals under D^+ bombardment. In general diffusivity or mobility decreases with increasing deuterium concentration, because with increasing deuterium concentration the number of vacant interstitial positions into which the deuteron can jump diminishes. The diffusion constants of deuteron for ordinary condition at $T = 300^\circ$K are $\sim 5 \times 10^{-7}$, $\sim 4 \times 10^{-5}$ and $\sim 3 \times 10^{-13}$cm^{2}s^{-1} in Pd, Fe and Ti, respsctively[18]. Enhanced deuteron diffusivity has also been reported under stress and under deuteron implantation. Although the mechanism to increase the diffusion is not understood completely, the diffusion constant can easily be changed under such special conditions. In the present work, thus, it is said very roughly that large diffusivity of deuteron results in low deuteron density.

A classical picture of screening has been discussed in a growth process of colloidal particles in electrolyte solution, for example in the textbook of electromagnetism [19]. In this case, an essential point is the fact that both negative and positive ions are fluid and, hence, their electric charges can be distributed so as to satisfy simultaneously the Poisson equation and the statistical distribution. As a result, the Coulomb repulsion is reduced not only by the negative ions but also by the positive ions. A jellium model for the electrostatic screening with the electron and D^+ gas in metal[20], being an extension of the above consideration, shows that the screening potential due to the fluid deuterons can be one order of magnitude larger than that due to the electrons because of the difference between Boson (d) and Fermion (e) statistics. Thus, we suggest the possibility of such a dynamic mechanism during the D^+ bombardment into the metal ; there, the fluidity of deuterons must play a decisive role.

§ 6. Conclusions

It is most important in this work that the DD fusion reaction can be enhanced extraordinarily when the reaction occurs in a particular host material such as PdO. The anomalously large screening potential, U_s = 600 eV deduced for PdO, clearly indicates the existence of a new mechanism to enhance the reaction rate. The value U_s = 600 eV gives a good fit to the PdO data of Fig.4 from 10 keV down to 2.5 keV. The existence of such a large screening potential may affect the astrophysical scenarios, in which the atoms are in most cases completely stripped of their atomic electrons and the nuclei are immersed in a sea of free electrons, as D^+ surrounded by conduction electrons in metal.

Moreover, if the reaction cross section can be extrapolated to thermal energies with the same screening potential and with the same deuteron density we had, 1.2×10^{21}/cm^3, then one can presume

the DD fusion rate to be $> 10^7$ $sec^{-1}cm^{-3}$ at room temperature.

It may be possible in the future to explore such conditions, first by increasing the beam intensity to directly measure the reaction rate below 2.5 keV.

References

[1] S. Engstler *et al.*: Z. Phys. **A342** (1992) 471.

[2] P. Prati *et al.*: Z. Phys. **A350** (1994) 171.

[3] U. Greif *et al.*: Z. Phys. **A351** (1995) 107.

[4] C. Arpesella *et al.*: Phys. Lett. **B389** (1996) 452.

[5] D. Zahnow, C. Rolfs, S. Schmidt and H.P. Tratvetter: Z. Phys. **A359** (1997) 211.

[6] H.S. Bosch and G.M. Hale: Nucl. Fusion **32** (1994) 611.

[7] J. Kasagi, T. Ohtsuki, I. Ishii and M. Hiraga: J. Phys. Soc.Japan **64** (1995) 777.

[8] J. Kasagi *et al.*: J. Phys. Soc. Japan **64** (1995) 3718.

[9] H. Yuki *et al.*: J. Phys. Soc. Japan **66** (1997) 73.

[10] H. Yuki *et al.*: J. Phys. G: Nucl. Part. Phys. **23** (1997) 1459.

[11] T.D. Shoppa *et al.*: Nucl. Phys. **A605** (1996) 387.

[12] S. Morimoto, S. Nagata, S. Yamaguchi and Y. Fujino: Nucl. Instr. and Meth. **B48** (1990) 478.

[13] J. Roth, W. Eckstein and J. Bohdansky: Radiation Effects **48** (1980) 231.

[14] H.H. Anderson and J.F. Ziegler: Hydrogen Stopping Powers and Ranges in All Elements (Pergamon, New York, 1977).

[15] J.E. Valdes *et al.*: Nucl. Instr. and Meth. **B73** (1993) 313.

[16] H.J. Assenbaum, K. Langanke and C. Rolfs: Z. Phys. **A237** (1987) 461.

[17] S. Ichimaru: Rev. Mod. Phys. **65** (1993) 255.

[18] Y. Fukai and H. Sugimoto: Adv. Phys. **34** (1985) 263.

[19] R.P. Feynman, R.B. Leighton and M.L. Sands: The Fyenman Lectures on Physics (Addison-Wesley Pub. Co. Inc., 1965).

[20] S.N. Vaidya and Y.S. Mayya: Jap. J. Appl. Phys. **28**, (1989) L2258.

Enhanced ^{6,7}Li+d Reactions in Pd

T. Baba, T. Noda, M. Shimokawa, J. Taguchi, H. Yuki and J. Kasagi

Laboratory of Nuclear Science, Tohoku University, Mikamine, Taihaku-ku, Sendai 982-0826

As is described in the previous report [1,2], low energy nuclear reactions in metal have been systematically investigated. So far, we focused on the D+D reactions in various metals and found that the DD fusion rate in PdO and Pd is enhanced very much. Although the mechanism to enhance the reaction rate is not understood, we have naturally explored other reactions, i.e., ^{6,7}Li(d, α) reactions, which may be enhanced in Pd, as well.

The experimental setup was similar to those reported in [2]. Used were deuteron beams with energies between 30 and 75 keV from the low-energy high-current ion beam generator operated in the acceleration mode. The target was a foil of Pd-Li alloy ($PdLi_x$($x\sim0.07$)), which was prepared by Sakamoto with a method of arc melting Pd and Li. The target was kept at low temperature, during the bombardment, between -80 and -70℃ to prevent the Li target from escaping from the spot where the beam bombards. Alpha particles emitted in the ^{6,7}Li(d, α) reactions were detected by a ΔE-E counter telescope consisting of 30- and 100-μm thick Si detectors. Al foil of 10 μm in thickness covered the front face of the ΔE detector in order to prevent secondary electrons and scattered deuterons from hitting the detector. The counter was placed at 125° with respect to the beam direction and subtended a solid angle of 0.14 sr. Requiring a coincidence between ΔE and E detectors completely eliminated electrical noise and enabled unambiguous identification of α-particles.

We have measured α-particle yields, as a function of bombarding energy, emitted in the ^{6,7}Li(d, α) reaction in Pd. In order to verify the constancy of the number of Li in Pd, the α-particle yield at 75 keV was measured at frequent intervals. The yield at each bombarding energy was, then, always divided by the yield at 75 keV measured just before and after the run. This procedure of normalization gives the relative reaction rate as a function of the bombarding energy.

In Fig.1, we show results of the ^{6,7}Li(d, α)^{4,5}He reaction in Pd; relative excitation function normalized to the yield at 75 keV. As expected, the yield steeply goes down as the bombard-ing energy decreases. Since the projectile deuterons are slowed down in the metal and the reactions can occur until the deuteron stops, the observed α-particle yield at the bombarding energy is the integrated one down to the zero energy (thick target yield). We estimated a standard thick target yield by using the reaction cross section parameterized reported by Engstler et al.[3] and the stopping cross sections by Andersen and Ziegler[4]. Solid lines in Fig.1 show the standard thick target yield corresponding to the bare ^{6,7}Li+D reaction, i.e., without enhancement. As seen, the standard calculation without any enhancement completely fails to explain the data at the lower energies. It is concluded that the reaction rate in Pd is very much enhanced not only for the D+D reaction but also for the ^{6,7}Li+D reaction. We deduced the values of V_s to give the best fits to the excitation data. These fits are shown

by the dotted curves in Fig.1. The results are V_s= 1.55±0.40 and 1.76±0.30 keV, respectively, for the ^{6}Li (d, α)^{4}He and ^{7}Li (d, α)^{5}He reactions in Pd. Since the screening energy due to the bound electrons is only about 0.3 keV, these values in Pd are really large. Although the origin of the enhancement is not known, yet, we have inferred that it might be related with the fluidity of deuteron in solids, as discussed in ref.[1].

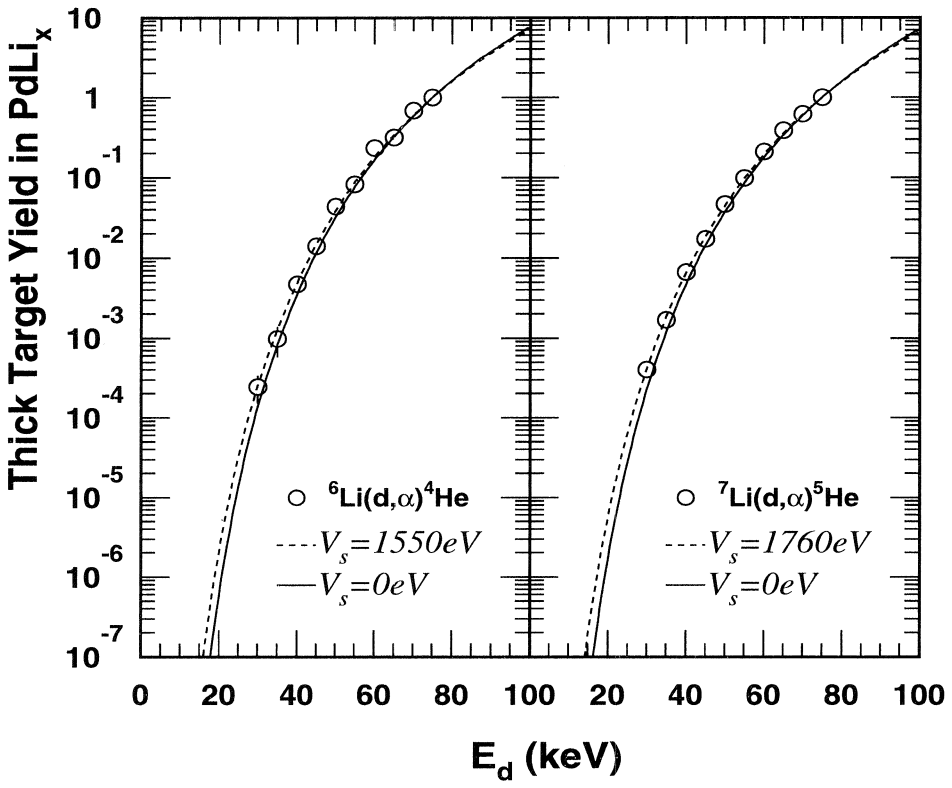

Fig.1. Relative yields of the ^{6,7}Li(d, α)^{4,5}He reaction in Pd against bombarding energy.

References

[1] H. Yuki *et al.*: JETP Lett. **68** (1999) 765 ; in the present Research Report of LNS.

[2] H. Yuki *et al.*: J. Phys. Soc. Japan **66** (1997) 73.

[3] S. Engstler *et al.*: Z. Phys. **A342** (1992) 471.

[4] H.H. Andersen and J.F. Ziegler: Hydrogen Stopping Powers and Ranges in All Elements (Pergamon, New York, 1977).

The 200 MeV Bremsstrahlung Tagged Photon Beam at LNS-Sendai

A. Saito[1], M. Chiba[1], H. Kanda[1], R. Kimura[1], Y. Kobayashi[1], O. Konno[2], K. Maeda[1], H. Matui[2], H. Miyase[1], A. Miyamoto[2], T. Ohtsuki[2], T. Suda[1], T. Tamae[2], Y. Terasaki[2], T. Terasawa[2], H. Tsubota[1], M. Tsuruta[2] and H. Yamazaki[2]

[1]*Physics Department, Graduate school of Science, Tohoku University, Sendai 980-8578*
[2]*Laboratory of Nuclear Science, Tohoku University, Sendai 982-0826*
[3]*Institute of Physical and Chemical Research (RIKEN), 2-1 Hiragana, Wako 351-0098*

We describe the 200-MeV bremsstrahlung photon tagging system, which was installed in the experimental Hall-1 at the Laboratory of Nuclear Science, Tohoku University. This system produces tagged photons from high duty electron beams supplied by Stretcher Booster Ring. The tagged photon energies are over a range from 20% to 80% of the incident electron energy. We carried out commissioning to examine the performance of the tagged photon beams produced by the 198 MeV electron beam. We demonstrated that the tagged photons can be employed for photonuclear reaction experiments with a momentum resolution $\Delta p/p \sim 1\%$ at the tagged photon intensity $I \leq 5 \times 10^6$.

§ 1. Introduction

Real-photon induced nuclear reactions in an energy range from Giant Dipole Resonance (GDR) to near the pion threshold have extensively been studied at the Laboratory of Nuclear Science, Tohoku University (LNS-Sendai) using the Sendai STretcher Ring (SSTR) [1] and the photon tagging system [2]. The characteristic features in this energy region are excitations of the giant resonance (GR), the one-nucleon direct-knockout (DK) and the two-nucleon photon absorption due to the meson exchange current (MEC). During the experiments with SSTR, we have shown MEC plays a dominant role for the photon absorption process above GR [3-9]. Although we tried to investigate the two nucleon state through MEC by (γ, $2N$) reactions, sufficiently qualified data have not been obtained. In the Δ-resonance region, the (γ, $2N$) reactions have been studied at Tokyo [10,11] and Mainz [12]. They have shown that the photon energy dependence in the exclusive cross sections is scale to that of the deuteron photodisintegration cross section. Consequently, the photon absorption by the two nucleons is thought to dominate the photonuclear reaction process above GR and can be applied to study the two nucleon states in nuclei.

The facility was once closed during the period of 1994 − 1998 to upgrade from SSTR to Stretcher Booster Ring (STB). The functions of STB are the pulsed beam stretcher, the energy booster and the beam accumulator. The real-photon induced experiments became to be carried out with the maximum electron energies of 0.3- and 1.2-GeV using the stretcher and the booster-accumulation mode, respectively.

In order to use the extracted 0.3-GeV stretched beam for the real-photon induced nuclear reaction experiments, we constructed a new beam line and a upgraded photon tagging system. This article reports the performance of the new beamline and the photon tagging system, and the representative results of the tagger commissioning.

§ 2. Experiment

2.1 LNS/STB Tagging system

The electron beams stretched by STB are delivered to the experimental Hall-1 through a newly constructed beam transport line called BL-V. The schematic BL-V layout is shown in Fig.1, together with STB and the experimental Halls. BL-V consists of three straight sections and two 90° deflecting system. The beams are transported by achromatic designed components with four dipole-magnets, four pairs of quadrupole-magnets and five beam-steering coils. Brass collimators were placed at the first and second straight section. The beamline length from STB to the tagger is about 80-m long. The beam spot size is monitored at the middle of second straight section, and the bremsstrahlung target position with photo-luminescence plates (ZnS). A plastic scintillation counter located just behind the second quadrupole-magnet, which is used to monitor the loss and the time structure of the electron beam. The beam ducts are made of 50 mm-diameter aluminum tube. They are evacuated by four ion pumps and three turbo-molecular pumps to a vacuum presser of $\sim 10^{-5}$ Pa.

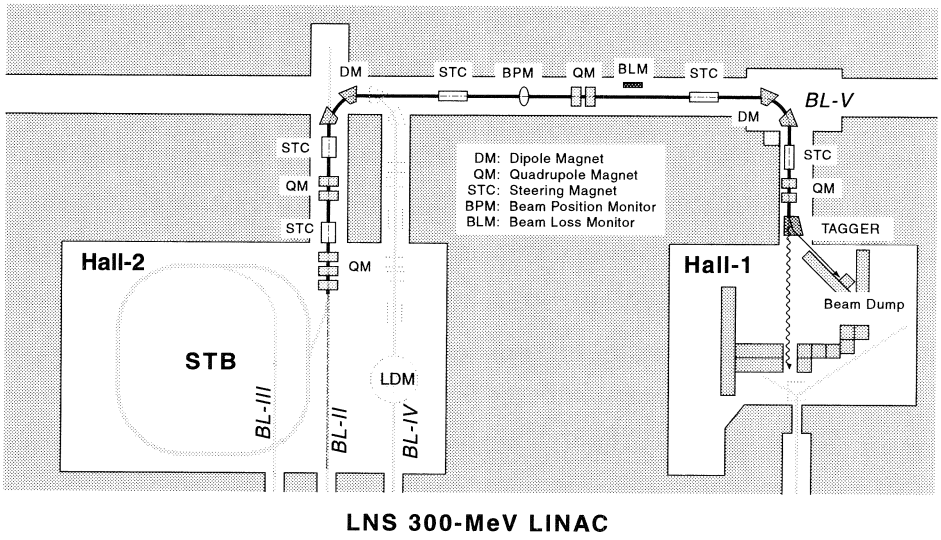

Fig.1. Schematic layout of BL-V. Gray lines show beam lines and STB. Solid line is BL-V.

As shown in Fig.2, the photon tagging system is located at the end of BL-V in Hall-1. The electron beams produce photons in a bremsstrahlung target placed at the entrance of the tagger. The photons irradiate the nuclear reaction target placed in Hall-1. The primary electron beam is stopped in the well-shielded beam dump. A thin-wall chamber, which is placed in front of the beam stopper, is used to monitor the beam intensity.

2.2 Tagging spectrometer

The tagging spectrometer is composed of a bremsstrahlung radiator, a dipole magnet and electron counters. As shown in Fig.2, the incident electrons are impinged on a target in a radiator box, where

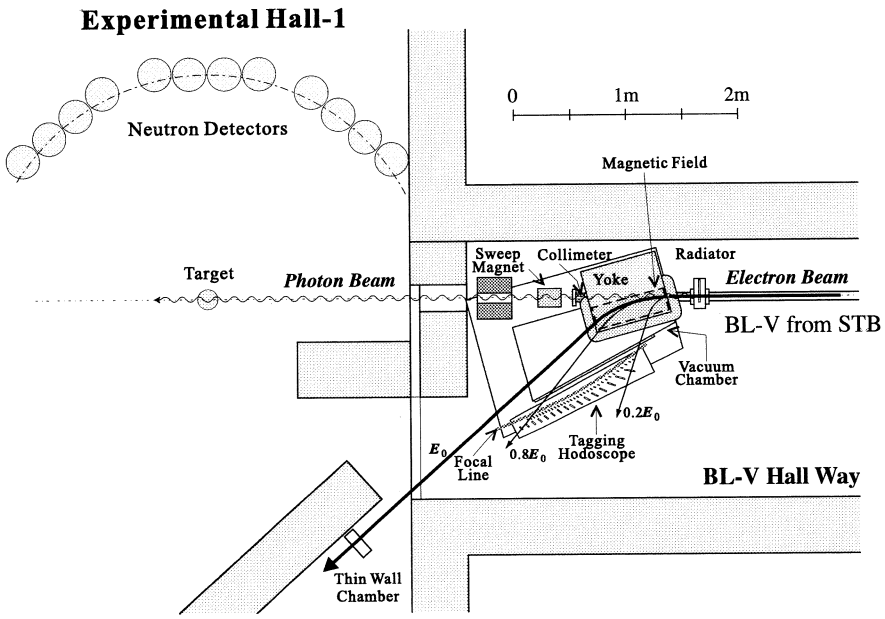

Fig.2. Layout of the photon tagging system and the neutron detector setup.

three bremsstrahlung radiator; a gold (3 μm), a platinum (10 μm) and an aluminum (80 μm) foils, and a ZnS beam monitor, are mounted on a rotatable device.

The tagged photon energy E_γ is determined as,

$$E_\gamma = E_0 - E_e - E_{recoil}, \tag{1}$$

where E_0 and E_e is the incident and outgoing electron energy, respectively. Since the transferred energy to the recoil nucleus E_{recoil} is negligibly small, the tagged photon energy E_γ is uniquely determined by E_0 and E_e, The incident electron energy E_0 is controlled by the STB operation and the BL-V condition. The energy of the post bremsstrahlung recoil-electron E_e is analyzed in a magnetic field. The magnetic field is generated by a simple rectangular-pole-shape magnet with 50 mm gap. This magnet allows a broad momentum acceptance, and puts the position of the focal plane far away from the magnetic field. The second order matrix calculation of the electron trajectories showed the momentum resolution $\Delta p/p \sim 1 \times 10^{-3}[\mathrm{mm}^{-1}]$ at the middle of the focal plane.

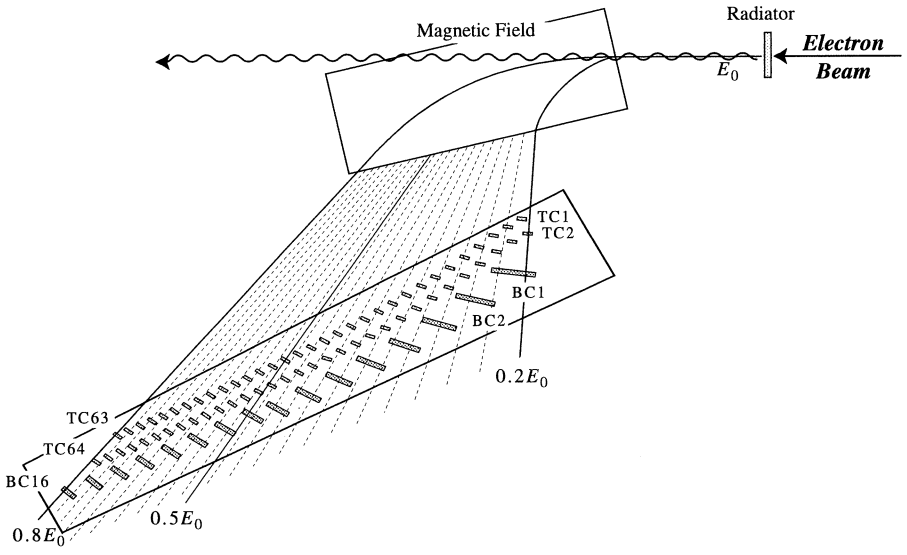

Fig.3. Bremsstrahlung recoil-electron trajectories in the tagger and the array of tagging and tagging-backup counters.

A plastic-scintillator hodoscope was used for the focal plane detector. It consists of 64-channnel tagging counters (TC) and 16-ch tagging-backup (BC) counters covered the energy range from 0.2 to 0.8 E_0. The widths of TC vary from 6.6 to 18.3 mm to achieve equal momentum acceptance of $\Delta p / p_0 \sim 9.3 \times 10^{-3}$, where p_0 is the incident electron momentum. When the higher energy electrons than 250 MeV become available at BL-V, the tagger energy range will be $E_\gamma^{MAX} = E_e - 30$ MeV to $E_\gamma^{MIN} = E_e - 130$ MeV keeping the energy resolution $\Delta E_\gamma \sim 1.5$ MeV. As shown in Fig.3, 32 TCs (F-TC) are located on the focal line of the tagging magnet and another 32 TCs (B-TC) placed just behind them. The horizontal beam-expanse at the B-TC position is calculated to be less than 0.5 mm, which is small enough compared with the position resolution.

The array of BC is used to reduce the accidentals that mainly come from electron hits of the beam line components. Sixteen units of a BC and four TCs are placed on the recoil-electron trajectories. The coincidence between a BC and a corresponding TC signal restricts the electron trajectory and efficiently, and gets rid of backgrounds.

2.3 Data acquisition

The tagger signals are processed by sixteen 4 channel Quad-Tag Modules (QTM). Each QTM accepts independent four linear signals from TC. After the TC signals are amplified and discriminated, they are strobed by a timing signal from the corresponding BC. Each QTM channel produces two strobed, one discriminated and one delayed (106 ns)-strobed TC timing signals. There is a logical sum-out [$\Sigma 4$] of four strobed TC signals in QTM. As shown in Fig.4, the trigger signal of the tagger side is,

$$[\Sigma 64] = \sum_{i=1}^{16} [\Sigma 4]_i \tag{2}$$

$$= \sum_{i=1}^{16} \sum_{j=1}^{4} [TC]_{4i-j+1} \tag{3}$$

where $[\Sigma 4]_i$ is the i-th QTM strobed sum-out.

In Fig.5, a sample circuit diagram for the (γ, np) experiment using liquid scintillation counters (LS) for neutrons and a multilayer range telescope (RT) for protons. The event trigger signals from LS and RT side are obtained by the coincidence between the timing signals from LS and RT. The first trigger signals for the data taking are generated by the event trigger signals in coincidence with [$\Sigma 64$] from the tagger as,

$$[\mathrm{ET}] = [\Sigma 64] \otimes ([\mathrm{LS}] \otimes [\mathrm{RT}]) \otimes [\overline{\mathrm{veto}}], \tag{4}$$

where [$\overline{\mathrm{veto}}$] is any veto signals from the cletectors and the accelerator.

We use a CAMAC+PC/LINUX system to take online data. As shown in Fig.6, the data encoded in CAMAC modules are collected through CC7700 CAMAC crate controller (CC) and ISA-bus interface. The data taking software, which was developed under the LINUX operating system, collects, analyzes and records the raw data.

When the collector receives a LAM signal from CAMAC, it starts to transfer the raw data from CAMAC. The recorder writes the forwarded data from the collector on the shared memory and stores them on the DVD-Ram drive. The analyzer displays the data on the monitor screen and refreshes the

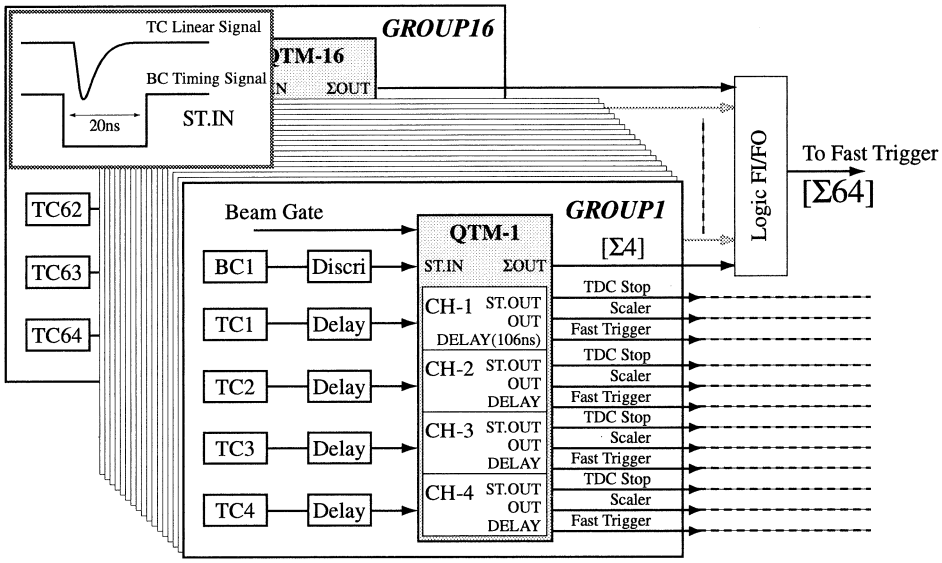

Fig.4. Schematic diagram of the tagger electronics.

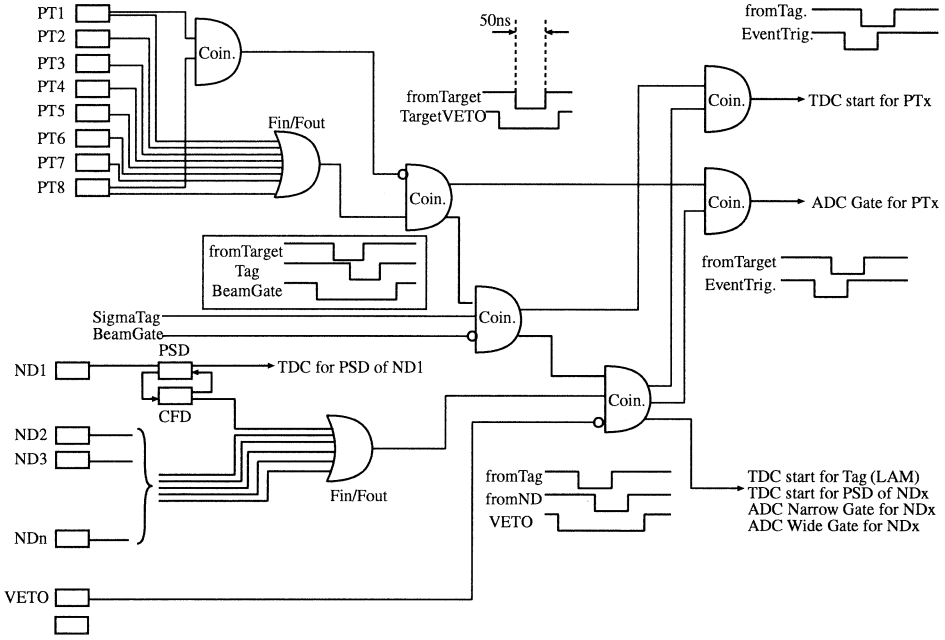

Fig.5. A typical circuit diagram for the (γ , np) experiment.

screen every few seconds. These processes are controlled by the process controller, which is controlled via a visual interface panel displayed on the monitor screen.

§ 3. Tagger Commissioning

The performances of the tagging system were examined by offline tests and commissioning experiments using a 198 MeV electron beam from LNS/STB. In the first stage of commissioning, relative timings among [TC] and [TC-BC] were verified. After the tuning of tagger counters, we measured several performance data of the tagging system such as the off/on ratio, the tagging efficiency and the count rate dependence.

3.1 Radiator off/on ratio

In addition to the electrons from the radiator, the background radiations hit TC and BC. Their

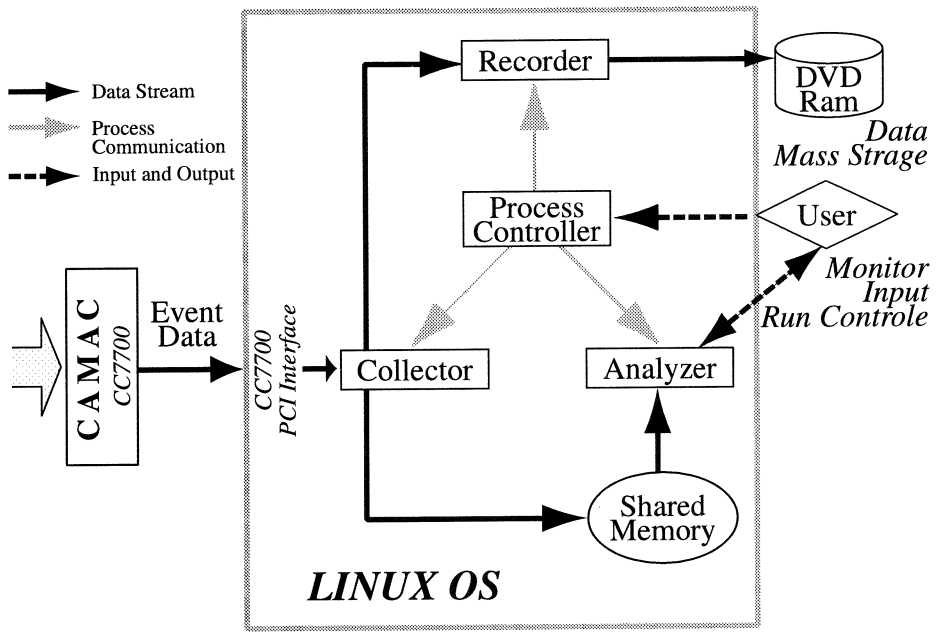

Fig.6. Flow diagram of online data taking system. Event data from the CC7700 crate controller and PCI-interface are processed by a online software under the LINUX Operation System. The online software consists of a collector, an analyzer, and a recorder and a process controller. The raw and histogram data are mass-storaged on DVD ram-disk.

main contributions are the room background from the transport line and the electron beam dump, and the hits of electron beam halo on the radiator holder. In order to estimate the background, we measured the ratio of each TC counting rate with (ON) to without (OFF) the radiator. In Fig.7, we show TC counts of ON (A) and OFF (B), and the ratio of OFF to ON (C), where the 3 μm Au target (10^{-3} radiation length) was used. As shown in Fig.7(C), the average counts ratio of OFF to ON is less than 5%. Although this value must be reduced by the more careful tunings of the STB and BL-V parameters, it might be endured to carry out the photonuclear reaction experiments.

3.2 Tagging efficiency

The tagging efficiency is defined as the ratio of the photon number to the electron counts. We employed a lead glass Cherenkov detector (20 radiation length) to count the tagged. The tagging efficiency of i-th counter is obtained as,

$$\varepsilon_i = \frac{N_i^{TB}(\text{on}) \otimes N^C(\text{coin.}) - N_i^{TB}(\text{on}) \otimes N_i^C(\text{acc.})}{N_i^{TB}(\text{on}) - N_i^{TB}(\text{off})} , \quad (5)$$

where N are the counts of rm [TC] $\otimes$ [BC] (TB) and the Cherenkov counter (C) with the conditions of radiator [on] and [off], and coincidence [coin] and accidental [acc.] events. The obtained photon tagging efficiency is shown in Fig.8, where the open circles are experimental result and the closed circles with error bar represent the results of a GEANT simulation.

3.3 Counting rate dependence

The counting rate dependence of the tagging efficiency must be very important to determine the absolute values of the cross section. Since the stability of the D.F. strongly depends on the STB condition, we have to monitor the fluctuation of the D.F. during the measurements to correct for the

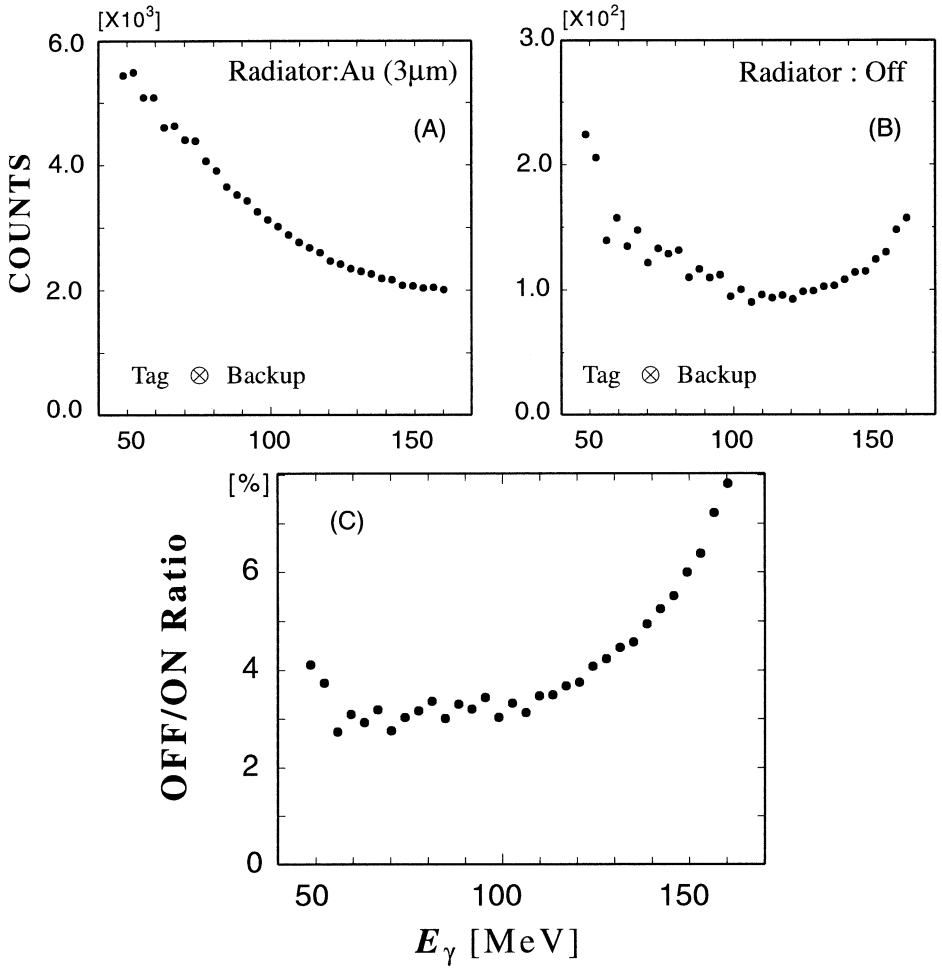

Fig.7. [TC] ⊗ [BC] counts of each tagging counters. (A) and (B) are radiator-on with 3 μ m Au radiator and radiator-off, respectively. (C) shows the counts ratio of the radiator-off to radiator-on. These figures show the data for the even numbered tagging counters placed on the focal line.

tagging efficiency. The relation between the D.F. and the counting rate is,

$$\text{D.F.} = \frac{N_i \cdot N_j \cdot \tau}{N_{acc}}, \qquad (6)$$

where N_i and N_j are the counting rate of any two TCs, N_{acc} is the accidental coincidence rate between $[TC]_i$ and $[TC]_i$ with the resolving time of τ. Unfortunately, the average beam D.F. was 20-30% during the tagger commissioning. We found the $[\Sigma 64] \sim 1.4 \times 10^6$ at the 100% equivalent D.F. is the maximum photon number without any serious corrections for the tagging efficiency.

§ 4. Conclusion

The LNS 200 MeV bremsstrahlung photon tagging system was installed in LNS/Hall-1. We have shown the required performances are satisfied to carried out any real-photon experiments in the photon energy range between GR and Δ-resonance. We need an additional STB tune to improve D.F. for the planned ^{40}Ca(γ, n) and ^{12}C(γ, np) experiments.

When the STB operation become to keep up with the slow extraction combined with the booster mode, the high-duty electron beam can be transported to the Hall-1 with a minor modification of BL-V.

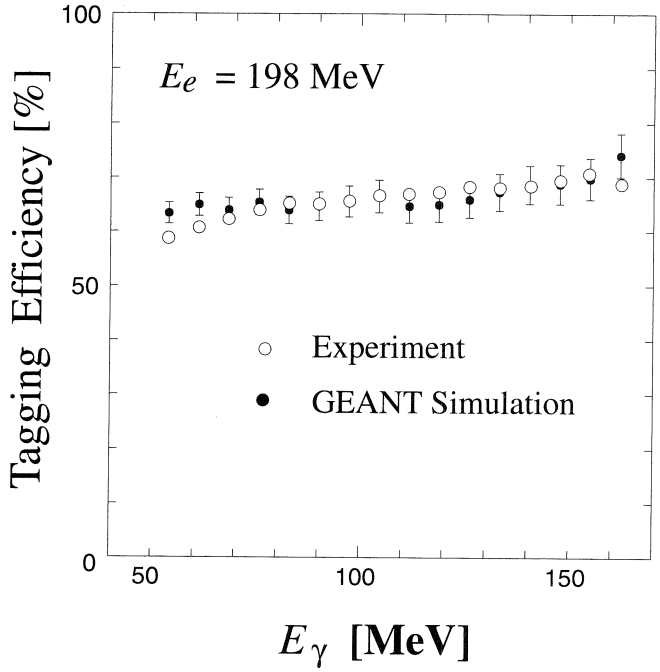

Fig.8. Photon tagging efficiency

The summary of the present tagger commissioning and the typical parameters of the elec-tron beams and the LNS photon tagging system is tabulated in Table 1 . As shown in the table, the high-resolution photon beams can be use for the photonuclear reaction experiments above the Δ-resonance using the presently developed photon tagging system.

This article is an interim report for the tagger and BL-V commissioning that were carried out in accordance with the LNS-proposal #2273.

Table 1. Parameters of photon tagging system at BL-V.

	Present Commissioning	Typical Stretcher Mode	Typical Booster Mode
Electron energy (E_0)	198 MeV	250 MeV	500 MeV
Duty factor	~30%	80%	80%
Tagging range	40-160 MeV	$0.2E_0$-$0.8E_0$	370-470MeV
Tagging resolution	1.8 MeV	$9.3\times10^{-3}E_0$	1.5 MeV
Tagging efficiency	0.65	0.7	0.8
Tagged photon rate	1.4×10^6 s^{-1}	5×10^6 s^{-1}	5×10^6 s^{-1}

References

[1] T. Tamae, M. Sugawara, K. Yoshida, O. Konno, T. Sasanuma, M. MutoY. Shibazaki, T. Tanaka, M. Hirooka, K. Yamada, T. Terasawa, S. Ura-sawa, T.Ichinohe, S. Takahashi, H. Miyase, Y. Kawazoe, S. Yamamoto and Y. Torizuka: Nucl. Instr. and Meth. **A264** (1988) 173.

[2] T. Terasawa, K. Mori, Y. Fujii, T. Suda, I. Nomura, O. Konno, T. Ichinohe, Y. Torizuka, K. Maeda, P.D. Harty, G.J. O'Keefe, M.N. Thompson: Nucl. Instr. and Meth. **A248** (1986) 429.

[3] P.D. Harty, M.N. Thompson, G.J. O'Keefe, R.P. Rassool, K. Mori, Y. Fujii, T. Suda, I. Nomura, O. Konno, T. Terasawa, Y. Torizuka: Phys. Rev. C**37** (1988) 13.

[4] T. Suda, O. Konno, I. Nomura, T. Suzuki, T. Terasawa, Y. Torizuka, J. Yokokawa, K. Maeda, J. Eden, G.O'Keefe, R. Rassool, M. Thompson, J. Kim: J. Phys. Soc. Jpn. **57** (1988) 5.

[5] J. Yokokawa, O. Konno, I. Nomura, T. Suda, T. Suzuki, T. Terasawa, Y. Torizuka, K. Maeda, J. Eden, D. McLean and M. Thompson: J. Phys. Soc. Jpn. **57** (1988) 6955.

[6] J.A. Eden, G.J. O'Keefe, R.P. Rassool, D.J. McLean, M.N. Thompson, T. Suda, I. Nomura, J. Yokokawa, O. Konno, T. Terasawa, Y. Torizuka: Phys. Rev. C**44** (1991) 753; Erratum Phys. Rev. C**46** (1992) 385.

[7] D.A. Sims, S. Karataglidis, G.J. O'Keefe, R.P. Rassool, A.D. Bates, M.N. Thompson, S. Ito, H. Matsuyama, S. Sazaki, O. Konno, T. Terasawa, T. Suda, K. Maeda: Physical Review C**45** (1992) 479.

[8] S. Ito, K. Maeda, T. Fukuda, O. Konno, T. Suda, M. Takeya, T. Terasawa: Nucl. Instr. and Meth. **A354** (1995) 475.

[9] K. Mori, P.D. Harty, Y. Fujii, O. Konno, K. Maeda, I. Nomura, G.J. O'Keefe, J. Ryckebusch, T. Suda, T. Terasawa, M.N. Thompson, Y. Torizuka: Phys. Rev. C**51** (1995) 2611.

[10] T. Emura, I. Endo, S. Endo, H. Itoh, S. Kato, M. Koike, K. Maeda, T. Maki, S. Maruo, K. Maruyama, Y. Murata, K. Niki, C. Rangacharyulu, A. Sasaki, T. Suda, Y. Sumi, Y. Wada, K. Yoshida: Phys. Lett. **286B** (1992) 229.

[11] K. Maruyama, K. Niki, Y. Sumi, T. Emura, I. Endo, S. Endo, H. Itoh, S. Kato, M. Koike, K. Maeda, T. Maki, Y. Murata, C. Rangacharyulu, A. Sasaki, T. Suda, Y. Wada, K. Yoshida, and the TAGX Collaboration: Phys. Lett. **393B** (1997) 295.

[12] I.J.D. MacGregor, T.T-H. Yau, J. Ahrens, J.R.M. Annand, R. Beck, D. Branford, P. Grabmayr, S.J. Hall, P.D. Harty, T. Hehl, J.D. Kellie, T. Lamparter, M. Liang, J.A. MacKenzie, S. McAllister, J.C. McGeorge, R.O. Owens, J. Ryckebusch, M. Sauer, R. Schneider, D.P. Watts: Phys. Rev. Lett. **80** (1998) 245.

[13] J.C. McGeorge, I.J.D. MacGregor, S.N. Dancer, J.R.M. Annand, I. Anthony, G.I. Crawford, S.J. Hall, P.D. Harty, J.D. Kellie, G.J. Miller, R.O. Owens, P.A. Wallace, D. Branford, A.C. Shotter, B. Schoch, R. Beck, H. Schmieden and J.M. Vogt: Phys. Rev. C**51** (1995) 1982.

Conceptual Design of the 1.2 GeV Photon Tagging System (STB Tagger)

H. Yamazaki, K. Hirota, T. Kinoshita, T. Nakabayashi, A. Katoh, T. Katsuyama, T. Itoh and J. Kasagi

Laboratory of Nuclear Science, Tohoku University, Taihaku, Sendai 982-0826

At the Laboratory of Nuclear Science (LNS or KAKURIKEN), Tohoku University, 1.2 GeV electron synchrotron called Stretcher-Booster-Ring (STB-ring) has been in operation. Our collaboration has been constructing the photon tagging system (STB tagger) in these years. The tagged photon beam is almost ready to use the physics experiment with its energy range from 0.8 GeV to 1.1 GeV

Quantum-chromodynamics (QCD) is a fundamental theory of the hadronic interactions. In the recent nuclear physic, it is very important to explain the properties of nucleus on the basis of QCD. Presently, QCD cannot be solved exactly because of the strong coupling constant. Therefore, many theoretical models are proposed, which contain the basic element of QCD in a simplified form. The experiment using GeV energy tagged photons is one of the useful tools to distinguish the appropriate QCD model. In this situation, GeV photon beams become available in various laboratories. Their properties of tagged photon beams are summarised in Table 1. A number of GeV photon experiments, which can contribute to the QCD based nuclear physics, are proposed. The details of experiments will not be discussed here, but some of the topics are listed below.

- N* properties in nuclear medium
- Meson properties in nuclear medium
- Strangeness photoproduction in nuclei

The property of nucleon resonance in nuclear medium is one of the most important issues in the QCD based nuclear physics. The detailed experimental studies on the nucleon resonances in nuclei, such as their masses and widths, are highly desirable by using exclusive reaction. Thus, our collaboration are going to study the property of nucleon resonances in nuclei systematically through meson photoproduction, especially the property of $S_{11}(1535)$ in nuclei through $(\gamma, \eta p)$ reaction on nuclei. In this experiment, it is necessary to determine the incident photon energy in order to identify the nucleon resonance in nuclei. Bremsstrahlung photons have continuous energy spectrum. In

Table 1. The properties of GeV tagged photon beams.

	Energy (GeV)	Intensity	Duty cycle
Tohoku	1.2	5×10^6	60~90%
SPring-8	2.4	5×10^6	100%
MAMI-B	0.8	10^7	100%
GRAAL	1.8	10^7	100%
TJNAF	4.2	10^7	100%

order to obtain an quasi-monochromatic photon, the photon tagging method is employed. An energy of photon is determined by analyzing the momentum of the recoil electron. To carry out this experiment, the required performance of the photon tagging system are listed below. First, the energy resolution of the tagged photons must be less than 30 MeV. The width of S_{11} in free space is 150 MeV/c^2, so it is desirable that the energy resolution of photon is 5 times smaller than the resonance width. Second, the fluctuation of the photon intensity must be less than 10%, because chance coincidence rate should be controlled low enough. Third, the photon intensity must be more than 5×10^6 par one second, because the cross section of the N* formation by photon is not so large compared with the hadronic reactions. To satisfy these requirements, we produced the new internal photon tagging system, which consists of the solid fiber radiator, the compact tagging counter installed in the bending magnet.

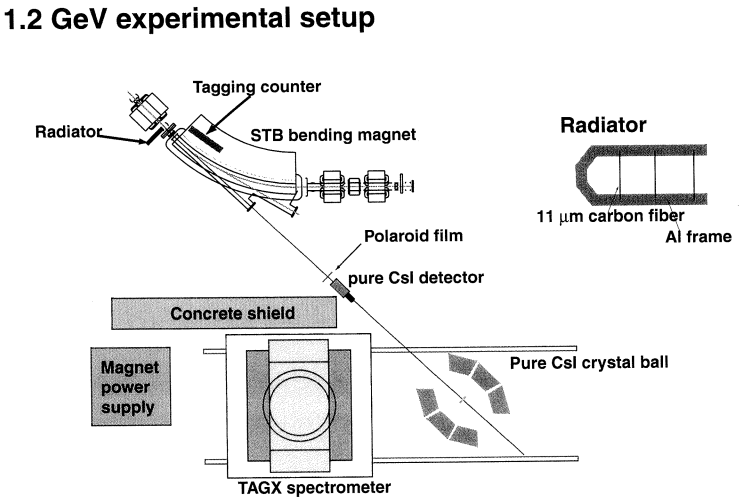

Fig.1. Schematic drawing of the 1.2 GeV tagged photon beam line.

The injected electrons with 200 MeV of energy are accelerated up to 1.2 GeV in 1 second and stored in STB-ring. After the acceleration the photon production target (radiator) are inserted into electron beam. The radiator consists of a carbon fiber with 11 μm of diameter. The spatial distribution of the electrons can be estimated as the normal distribution. The size of the electron beam at the reaction point is about 0.8 mm at one standard deviation(σ). When the intensity of the circulating current is 3 mA, the number of electrons which pass through a radiator are 15 nA at the radiator position of 3.5σ outside from the center of the electron beam. The intensity of the tagged photon beam reduces exponentially with the fixed radiator position. The almost constant flux of the tagged photon can be obtained by slowly moving the carbon fiber to electron center orbit. The flat top period is about 5 seconds. Details of the radiator systems will be reported in the following section.

One of the bending magnets of STB-ring is used as an analyzing magnet, Thus, the tagging counters should be inserted into the bending magnet. Tagging counter system must be constructed with compact volume; less than 10 cm in width and 20 cm in height. At the acceleration period, the magnetic field in the bending magnet is ramped up from 0.2 T to 1.3 T. The tagging counter system should be made of an insulator in order to avoid a disturbance of the magnetic field caused by the eddy

current. Scintillations are extracted from the bending magnet through the plastic optical fiber with 3.5 m long and are fed into the photo-multiplier tube. The energy range of the tagged photon is from 0.8 GeV to 1.1 GeV, and the energy resolution is about 6 MeV, when the energy of electron is 1.2 GeV. The other photon energy range from 0.68 to 0.85 GeV will be obtained with the electron energy of 0.93 GeV. The tagged photon intensity is about 1 times 10^7 par one second, and its efficiency is more than 80%. Details of the photon tagging system and the performance of the tagged photon beam will be reported in next year.

Development of a Movable Radiator System for the STB Tagger

K. Hirota, O. Konno, H. Yamazaki, T. Kinoshita and J. Kasagi

Laboratory of Nuclear Science, Tohoku University, Sendai 982-0826

The 1.2 GeV tagged gamma system (STB Tagger) is, now, being developed for various experiments with GeV photons, such as (γ , η) and (γ , K) reactions. As is mentioned in the previous report [1], the STB Tagger is designed so as to use a bending magnet (BM4) of the STB ring as a momentum analyzer of recoil electrons, and a radiator being the target of a electron beam to produce photon is placed at 325 mm upstream from the entrance of the BM4. A sequence of the STB ring operation for the tagged photon experiment is as follows (1) injection of a 200 MeV electron beam from the LINAC, (2) 0.5 sec for a circulation of the beam at 200 MeV, (3) 1.1 sec for an acceleration of the beam up to 1.2 GeV, (4) several sec (typically 6 sec) for a circulation at 1.2 GeV and (5) 1.1 sec lower the magnet current. Thus, in order to construct such a tagged photon system with using a component of the synchrotron ring, the system should be compact and the fact that the electron beam is circulating in the ring even in the acceleration period should be considered.

We have employed a radiator system with a solid target, since a gas jet target system requires a huge vacuum system and is much costly. Then the following requests must be satisfied: (1) the radiator can be easily removed from the beam position not to interrupt the beam except for the 1.2 GeV circulating period, (2) its position can be adjusted with in 0.002 mm so that the photon intensity is controlled by changing the position, (3) the radiator must be thin and low-z material to produce photons with intensity of about 10^7, and (4) the deformation and deterioration of the radiator due to heat and radiation must be small to be fit for a long-time frequent use.

Figure 1 shows a view of the radiator system, which is inserted between the quadrupole magnet and the bending magnet BM4. The pulse motor (0.36° /step) is controlled by IBM-PC, and the step of movement is 2 μm. The movable distance is 100 mm, and the maximum velocity of the radiator is 80

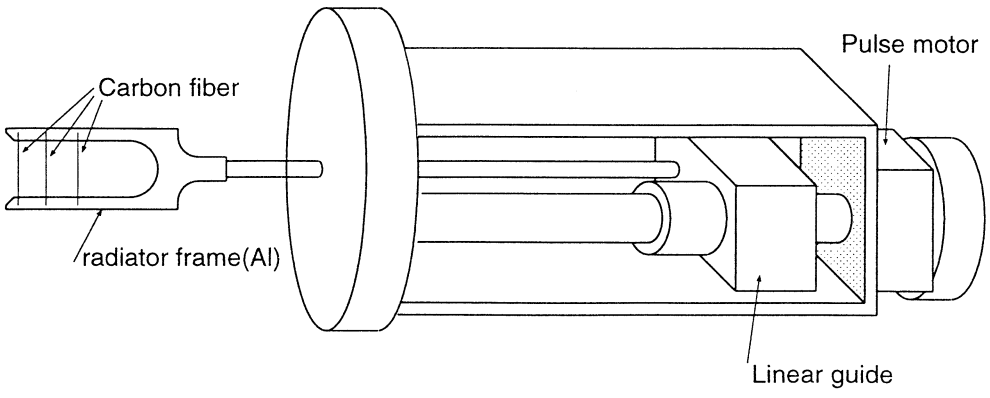

Fig.1. Schematic view of the radiator system of the STB Tagger.

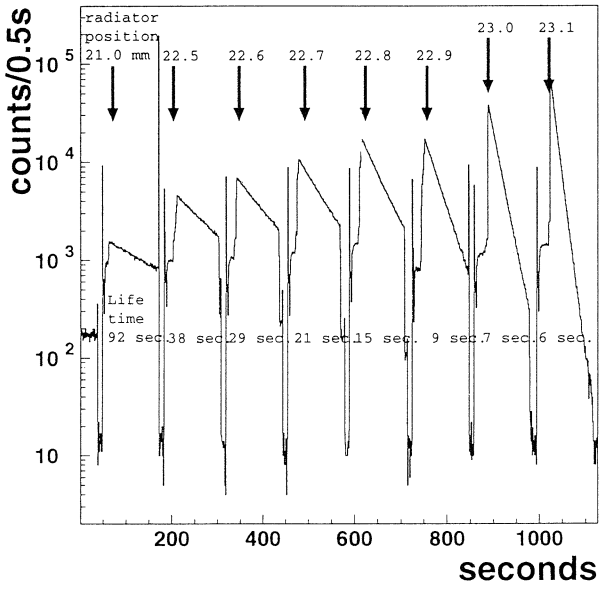

Fig.2. Photon yield vs. time for various radiator position.

mm/s. The radiator target is a carbon fiber with a diameter of 11 μm, fabricated by Kureha Chemical Industry Co., which is made of pitch. This pitch-made fiber has an advantage over the normal fiber, usually made of polyacrylonitrile, of the point that the coefficient of thermal expansion is almost zero or slightly positive. Then, it might be possible to keep the position reproducibility well and to lengthen the lifetime as the radiator. Three fibers are mounted on the frame; the distance between them is 19 mm.

The performance of the radiator system was tested with a 1.2 GeV electron beam. Figure 2 shows the photon yield versus time for various radiator position. As seen, the counting rate of the emitted gamma rays is the maximum at the time that the radiator insert to the beam line (the arrow point), and exponentially decays. The decay constant becomes large as the radiator position moves to the beam central orbit. It was found that the photon emission of about 10^6/sec can be obtain with the mean lifetime of 6 sec, as shown in Fig.2.

It is concluded that the movable radiator system essentially works well, the lifetime of the radiator seems very long, the position of the radiator can be precisely controlled, and this results in easily controlling of the number of emitted photons. A full-automatic control mechanism, which enables the number of photons constant by moving the radiator position, are now being developed.

References

[1] H. Yamazaki *et al.*: in this Research Report of LNS.

Design and Construction of Multi-detectors System with 148 Pure CsI Scintillators (SCISSORS)

K. Hirota[1], H. Yamazaki[1], T. Kinoshita[1], J. Kasagi[1] and H. Orihara[2]

[1]*Laboratory of Nuclear Science, Tohoku University, Sendai 982-0826*
[2]*Cyclotron and Radioisotope Center, Tohoku University, Sendai 980-8578*

As is described in other reports [1], the STB Tagger has been developed to produce real photons up to 1.1 GeV. The photon beam has interesting characteristics; a high energy resolution (ΔE = 3 MeV for the goal), and an energy range covering various meson production thresholds such as π, η, ρ, ω and K, all channels of great interest. One of the main projects using the STB Tagger is, thus, to study meson photoproduction and nucleon resonances. For this purpose and to extend our studies on η-meson photoproduction [2], we have designed and constructed a multi-detector system, which, mainly, aims at observing neutral mesons through a 2γ decay channel.

This is a cooperative development performed by the LNS and the CYRIC (Cyclotron and Radio Isotope Center, Tohoku University), and, hence, the detector system will be used not only at the LNS but also at the CYRIC where it will be mainly used for measurements of high energy gamma rays and π meson emissions in heavy ion reactions. Therefore, we considered the following points as strong restrictions for the detector system; (1) gamma rays with energy up to 1 GeV are measurable by each detector with a reasonable energy resolution, (2) each detector has a good time resolution, (3) the granularity of the system is small enough to obtain a good invariant mass resolution, (4) this is the first phase toward a 4π detector system (because of the limited budget), but the system covers large solid angles as possible, and (5) the system can be easily transfered and assembled from the one experimental vault to the other (a distance between the LNS and the CYRIC is about 8 km).

We have employed a pure CsI crystal as a scintillator because of its good features [3]; high stopping power, good energy and time resolution and good cost performance. A unit of the system is like a honeycomb, i.e., the structure of six-sided cells. It consists of 37 pure CsI crystals and the system of the first phase is composed of 4 units (148 scintillators). The system is called SCISSORS (Sendai CsI Scintillator System On Radiation Search).

In Fig.1 we show the structure of a pure CsI scintillation detector. As shown the crystal is in shape of a tapered hexagonal prism ; the length of a side is 27.5 mm in front and 42.5 mm in back and the

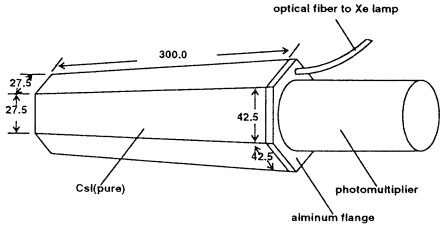

Fig.1. CsI scintillation detector.

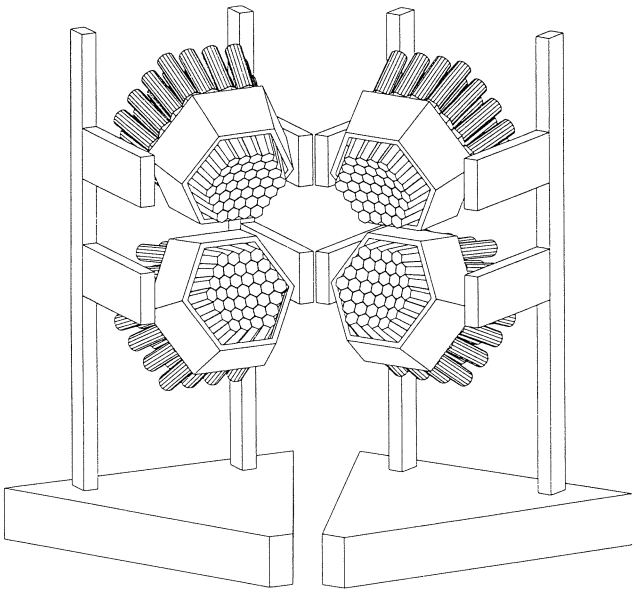

Fig.2. View of the CsI detector system, CSISSORS.

depth is 300 mm, corresponding to 16 radiation length. All surfaces of the crystal are polished to the optical grade and covered with a Teflon tape acting as a reflector. The crystal is inserted into a housing made of 1-mm thick Al plate, for the mechanical protection as well as the light shield. Since the main emission from a pure CsI crystal is 305 nm in wavelength, a photomultiplier (PMT) of EMI 9814WB, 2-inch tube with UV glass window, is employed. An optical fiber is glued on the crystal, in order to check gain stability of the PMT for a long term run.

Fig.2 shows an assembly of the detector system, SCISSORS. As shown, two units of the honeycomb are mounted on an arm plate which can rotate around the target. The distance from the target to the detector fronts can be adjusted, only for both units together. The angle to the horizontal plane and the height of the honeycomb can be adjusted separately. The taper of each crystal is originally designed so as to form a pseudo-spherical surface with 55-cm radius. Four units of detectors, then, subtend a solid angle of 0.96 sr.

The performance of SCISSORS is discussed based on a simulation by the code GEANT3. Although the energy leak from the rear is only 3% of the incident energy, that from the sides amounts to 15%, for a 1-GeV gamma ray bombardment on a single crystal. In this case, the calculated spectrum shows a peak at 820 MeV having a large tail to lower energies, and the energy resolution is only 150 MeV FWHM. Summing up the energies deposited in surrounding detectors is essential to improve the energy resolution. The total energy deposited in seven detectors (bombarded one and six surroundings) amounts to 90% of the incident one, and the energy resolution is really improved to 50 MeV FWHM. Thus, it can be said that the multi-detector system, SCISSORS, is expected to be a good detector to measure neutral mesons as well as high energy gamma rays.

References

[1] Reports on the STB Tagger in this Research Report of LNS.

[2] T. Yorita *et al.*: Phys. Lett. **B476** (2000) 226.

[3] H. Yamazaki *et al.*: Nucl. Instr. Meth. **A391** (1997) 427.

Beam Irradiation Test for Focal Plane SSD at Jefferson Lab

T. Takahashi[1], M. Ukai[1], K. Watanabe[1], T. Miyoshi[1], Y. Fujii[1], T. Watanabe[1], K. Dobashi[1], H. Yamaguchi[1], K. Maeda[1], H. Tamura[1], O. Hashimoto[1] and K.A. Lan[2]

[1]*Department of Physics, Graduate School of Science, Tohoku University, Sendai 980-8578*
[2]*Physics Department, University of Houston, TX, U.S.A.*

Radiation hardness was investigated for a silicon strip detector (SSD) to be used as a focal plane detector of the scattered electron spectrometer in a series of experiments at Jefferson Lab. for hypernuclear spectroscopy by the (e, e'K^+) reaction. The SSD was irradiated up to the dose of 150 kGy with a 200 MeV electron beam at the low energy tagged photon facility of Laboratory of Nuclear Science. After the irradiation, only slight increase of the noise level was observed, although the leak current increased linearly with the dose. It was confirmed that the SSD can be operated without any serious degradation of the performance under expected dose of 10 - 15 kGy during the 3 months experiment.

§ 1. Introduction

Experiments to carry out high-quality hypernuclear spectroscopy by the (e, e'K^+) reaction is under preparation at Jefferson Lab. (Jlab). Among them, E89-09 [1] and E97-08 [2] use Hypernuclear Specteometer System (HNSS) in Hall C. Since the zero-degree tagging method is employed in these experiments in order to maximize virtual photon flux, counting-rate of electron-arm detectors is as high as 2×10^8Hz due to huge numbers of electrons from bremsstrahlung. A compact SSD system was designed and fabricated as the focal plane detector system that accepts such high-count rate electrons[3]. In the present test experiment, we intended to examine the radiation hardness of the SSD by directly irradiating it with the 200 MeV electron beam prior to the Jlab experiments.

Two types of the damage of the SSD due to radiation are known. One is so-called bulk damage in which incident radiation knock out atoms of crystal lattice by non-ionizing energy loss (NIEL). These defects act as generation and recombination centers of carriers, thus, reducing the carrier's lifetime and increasing the leak current. The other is surface one in which the charge generated by ioniing radiations is accumulated close to Si/SiO_2 interface in SiO_2. The accumulated charge makes flat band voltage and full depletion voltage higher and increase the leak current. In the case of JLab experiment, since the radiation is high energy (~300 MeV) electrons which have one order of magnitude less NIEL than hadrons [4], bulk damage is expect to be negligible compared with surface one.

§ 2. Focal Plane SSD and Front-end Electronics

In order to obtain radiation resistance, we made the following considerations in designing the SSD with Hamamatsu Photonics;

Table 1. SSD specification

effective area	72×50 mm^2
strip pitch	0.500 mm
strip width	0.360 mm
number of readout strips	144
electrode width	0.352 mm
poly-Si resister	10 MΩ
strip capacitance	$\leq$ 20 pF

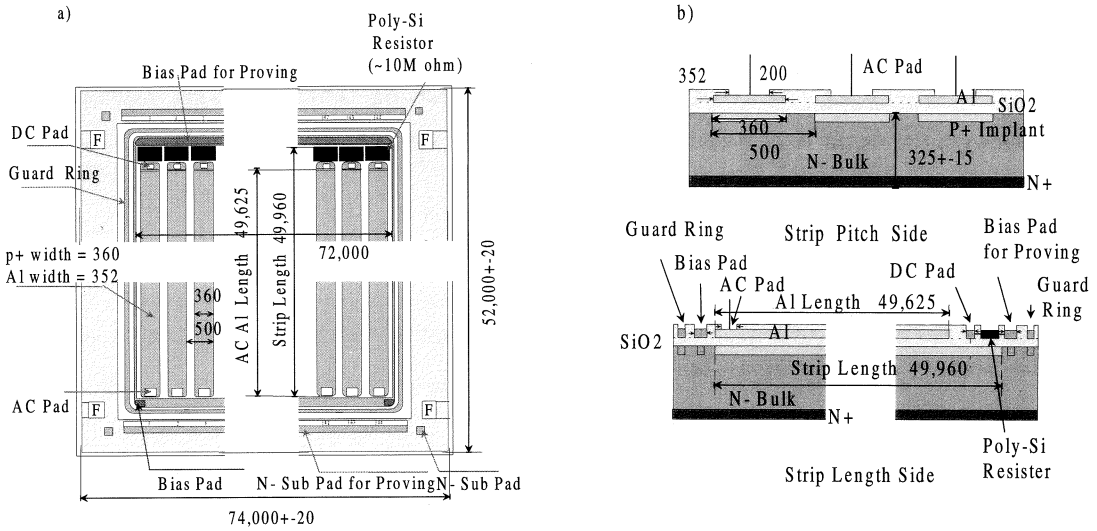

Fig.1. Front (a) and side (b) views of the SSD. All number in figures is in an unit of μm.

1. AC-coupled readout

   The leak current will be increased by the radiation damage. The signals are read out through the capacitor which is made of Al-electrodes, SiO_2, and p^+ pads (MOS structure), to prevent the increased leak current going directly to preamplifier and reducing dynamic range.

2. Bias voltage

   Since the present SSD requires 1-dimensional readout, positive bias voltage is applied to the n-side so as to avoid strong electrical field in SiO_2. Every p-strip is grounded through a built-in resister (~10 MΩ) made of poly-Si and electrically separated each other.

3. Width of Al-electrodes and p-strips

   According to Ref. [5], breakdown voltage (voltage where leak current is suddenly increased) becomes higher when width and length of Al-electrode are narrower and shorter than that of p-pads. Widths of an Al-electrode and a p-pad are chosen to be 352 μm and 360 μm, respectively.

4. Guard-ring structure [6]

   One of the most serious problems in the MOS structure is micro-discharge due to locally strong electrical field at the edge region. In our SSD, the p-side of the sensitive area is surrounded by a floating guard-ring which reduces field strength at the edge region.

Specifications of the SSD are listed in Table 1. Front and side views of the SSD structure are shown in Fig.1.

Since counting-rate per strip is expected to be 10^5 Hz or higher, only discriminated timing signals are read out. For this purpose, we use TEKZ chip [7] which contains 64-channel fast amplifier, shaper, and discriminator in a single package. The TEKZ was developed for ZEUS silicon strip detector by University of California, Santa Cruz group. The SSD and 3 TEKZ's are mounted on the Front End Board (FEB). The bias line is soldered between n^+ layer of the SSD and FEB electrode, while the ground and signal lines are wire-bonded to the FEB electrodes. Since the TEKZ output logic signal of 800mV height and 40 ns width can not directly drive long cables and TDC's, they are converted to ECL logic signals by an ECL driver board of 48 channels/board. The ECL driver boards are housed in a special box which supplies FEB and ECL driver's power as well as SSD bias. The output ECL signals will send to and be read by FASTBUS multi-hit TDC's (LeCroy 1877) in JLab experiment. In the present experiment, we used drift chamber time digitizing system which contains single-width TDC's (LeCroy 4291B, 4298, and 4299).

§ 3. Methods to Monitor Noise Level

Two different methods were used to monitor noise level of the SSD. Random noise scan (RNS) method is to measure singles rates by changing the threshold under no signal input. From the relation [8],

$$N = N_0 \exp\left(-\frac{q_{\mathrm{th}}^2}{2\sigma^2}\right) \tag{1}$$

where N is singles rate, q_{th} is threshold charge corresponding to threshold voltage, noise level is obtained.

The other one is noise level scan (NLS) using test pulse supplied to TEKZ test input. Fitting the occupation curve obtained by changing threshold or test pulse height with an error function, noise level is obtained.

§ 4. Beam Irradiation Test and Results

Beam irradiation test was done at low energy tagging channel course without exciting the magnet in January, 2000. The 200 MeV pulsed electron beam collimated to 8 mm ϕ was bombarded to the SSD. During the irradiation, readout electronics was powered off but SSD bias on. Irradiated beams were measured with Faraday cup located downstream of the SSD. Relative doses between separated irradiation were also checked by activation of Au foils put on the exit of collimator by measuring 355keV γ-ray from $^{196}\mathrm{Au} \rightarrow {}^{196}\mathrm{Pt}^*$. At some intervals of irradiation, we measured leak current of the SSD and noise levels by two methods described above.

Results are plotted in Figs.2-4. Dose was evaluated by assuming uniform distribution of 8mm ϕ beam size and minimizing ionizing energy deposit of the electrons. The leak current increase linearly with dose. R. Wunstorf *et. al.* reported that surface leak current is saturated around 50 kGy without

bias during the irradiation and the saturation value was $2\,\mu A/cm^2$[9]. In the present measurement with bias, such a saturation was not observed. Note that our leak current is the value corresponding to whole SSD and direct comparison of the values is difficult because of spot irradiation in the present test.

The noise level from NLS shows no change by dose as shown in Fig.3. Besides, there is no clear difference in noise level change between strips irradiated (ch.81-93) and not (ch.40, 50). The noise level from RNS, however, shows increase by dose (Fig.4). This may owe that NLS method is sensitive to the noise of electronics part and the noise from the SSD is indirectly inspected through the change of strip capacitance parallel to test input capacitor. In conclusion, the RNS method is better to monitor radiation damage than the NLS and can be used in JLab experiment. No clear degradation of an efficiency was observed in cosmic-ray measurement after beam time.

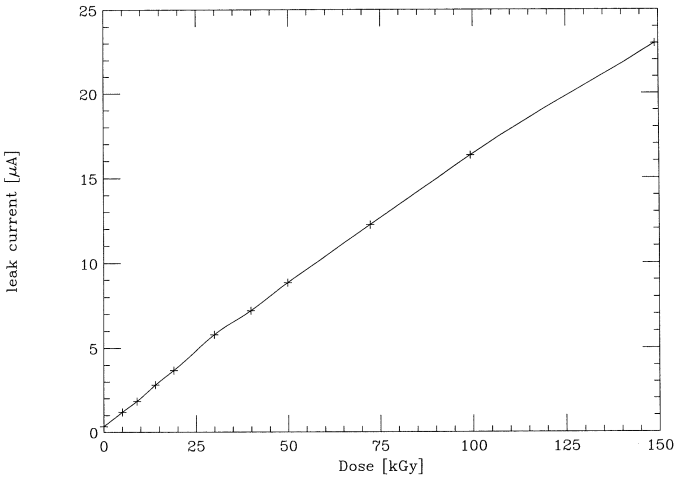

Fig.2. Change of leak current during the irradiation.

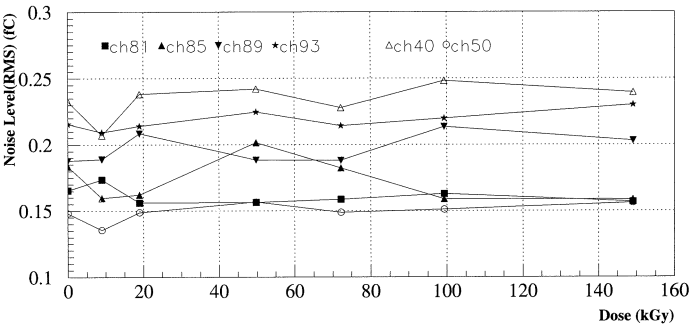

Fig.3. Noise level measured by noise level scan method. Closed and opened markers present strips where beam irradiated and did not, respectively.

§ 5. Summary

We have examined the radiation hardness of a silicon strip detector (SSD), which is to be used as a focal plane detector system of the scattered electron spectrometer for hypernuclear spectroscopy experiments in Hall C of Jefferson Lab. The SSD is required to work stable under high counting-rate and high radiation environment. Prior to the experiment at Jlab, the SSD was irradiated by 200 MeV electron at LNS and its performance was tested. Although leak current increased almost linearly up to the maximum applied dose of 150 kGy, noise

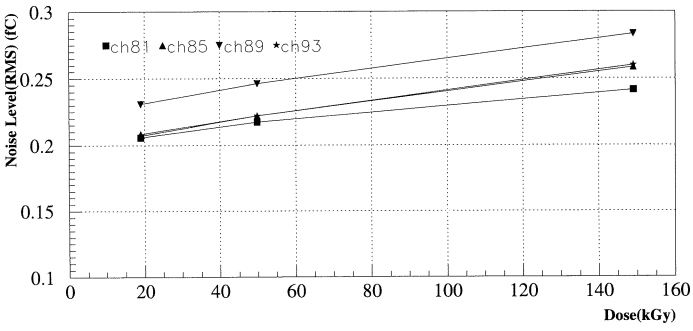

Fig.4. Noise level measured by random noise scan method.

level remained within an acceptable level.

We greatly thank to the staffs of LNS, especially Prof. Tamae, Dr. Konno, and Dr. Hinode for their effort for beam tuning. We also appreciate Prof. Terasawa for beam time arrangement, Mr. Miyamoto for taking operator shifts during his busy time.

References

[1] L. Tang, R. Chrien, E.V. Hungerford *et al.*: Jlab proposal E89-009 http://www.jlab.org/exp-prog/proposals/PR89-009. pdf.

[2] O. Hashimoto, L. Tang, E.V. Hungerford *et al.*: Jlab proposal E97-008.

[3] T. Miyoshi: Master Thesis, Tohoku University (in Japanese), 1998.

[4] C.J. Dale *et al.*: IEEE **NS33** (1989) 1208.

[5] T. Ohsugi *et al.*: Nucl. Instr. and Meth. **A342** (1993) 22.

[6] T. Ohsugi *et al.*: Nucl. Instr. and Meth. **A383** (1996) 166.

[7] E. Barberis *et al.*: Nucl. Phys. **B32** (1994) 513.

[8] E. Barberis *et al.*: IEEE **NS41** (1994) 785.

[9] R. Wunstorf *et al.*: Nucl. Instr. and Meth. **A377** (1996) 290.

Observation of S_{11} Resonance in Nuclei via (γ, η) Reactions

T. Yorita[2], H. Yamazaki[1], T. Kinoshita[1], T. Okuda[1], H. Matsui[1], J. Kasagi[1], T. Suda[3], H. Okuno[4], H. Shimizu[2] and T. Maruyama[5]

[1]*Laboratory of Nuclear Science, Tohoku University, Mikamine, Taihaku, Sendai 982-0826.*

[2]*Research Center for Nuclear Physics, Osaka University, Ibaraki Osaka 567-0047.*

[3]*Institute of Physical and chemical Research (RIKEN), Wako 351-0098.*

[4]*Institute of Particle and Nuclear Studies, (KEK-Tanashi), Tokyo 188-0002.*

[5]*College of Bioresource Sciences, Nihon University, Fujisawa 252-8510.*

The recent nuclear-photoabsorption cross sections have shown clear evidence of nuclear medium effects on nucleon resonances: enhancements in the cross section due to the effects of D_{13} (1520) and F_{15} (1680) resonances, clearly seen in the total photoabsorption measurements on hydrogen and deuteron [1], disappear on nuclei [2]. Large increase of the resonance width in nuclei was proposed as one of the interpretations for the disappearance. However, the resonances are overlapping and superimposed on continuous background, and, thus, it is hard to observe the respective resonance of large width. We have studied the S_{11} (1535) resonance in nuclei. Since it decays to the Nη channel with the branching ratio of about 50% and the elementary H(γ, η) H reaction reaction below 1.0 GeV is explained by the excitation of the S_{11} resonance without any background process, one can expect to excite only the S_{11} resonance in the (γ, η) reactions on nuclei below the photon energy of 1.0 GeV. Thus, we have measured the total(γ, η) cross sections on C, Al and Cu. Part of the present work has been published in ref. [3].

The experiments were performed using a tagged photon beam from the 1.3 GeV electron synchrotron at KEK-Tanashi (former INS). The intensity of the photon beam was 9×10^5/s for $0.68 \leq E_\gamma \leq 1.0$ GeV. Emitted η mesons were identified by the invariant mass analysis of two decay photons, which were detected by two sets of pure CsI calorimetere with plastic scintillators for charged particle veto. Differential cross sections of the C, Al, Cu (γ, η) reactions were measured for the polar angles from 0° to 90° in the laboratory system.

In Fig.1, we show the obtained total η photoproduction cross sections for C, Al, Cu (γ, η) reactions, respectively, with open circles, open squares and open triangles. A broad resonance due to the excitation and decay of the S_{11} resonance is cearly seen in C, Al and Cu nuclei for the first time. In order to deduce the resonance property more quantitatively, we have performed theoretical calculations based on the quantum molecular dynamics model, and have compared the experimental data with the calculations. The medium effects, such as the Fermi motion, the Pauli blocking, and N-η and N-N* collisions are incorporated in the calculation. The resonance energy and width of the S_{11} resonance is not uniquely determined. Thus, we employed two sets of the resonance parameter: The one is deduced by Kursche et al.[4], M_R = 1544 MeV and Γ = 212±20 MeV, and the other reported by Armstrong et

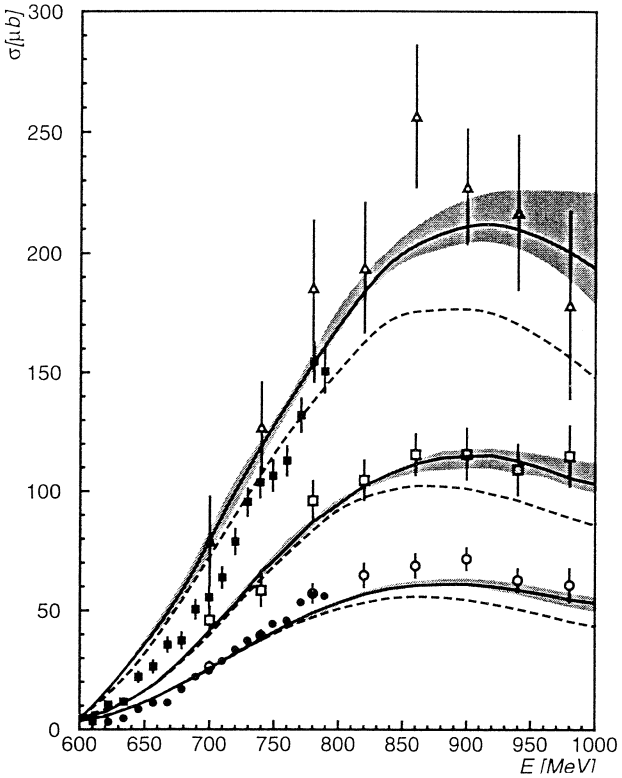

Fig.1. Total photo-η production cross sections on C (open circle), Al (open square) and Cu (open triangle). The results of the QMD calculations are also shown; the solid lines correspond to the resonance width of 212 MeV and the dashed lines to 154 MeV.

al.[5], M_R = 1532 MeV and Γ = 154±20 MeV. The latter parameter gives much better fit to the cross section of the elementary H(γ , η) reaction up to 1.1 GeV, althogh the former reproduces the data below 800 MeV very well.

The results of the calculations are also shown in Fig.1. Dashed curves are the results with Γ = 154 MeV and solid curves with Γ = 212 MeV. As shown, the solid curves generally reproduce the data very well and the dashed curves always underestimate the yields. It should be noted that the resonance parameter with Γ = 154 MeV can explain the H (γ , η) reaction very well. This indicates that the width of the S_{11} resonance might be changed in the nuclear medium; more than 60 MeV increased. It is difficult to consider such large increase of the width only due to collision broadening.

References

[1] T.A. Armstrong *et al.*: Nucl. Phys. B**41** (1972) 445.

[2] T. Frommhold *et al.*: Phys. Lett. B**295** (1992) 28.

[3] T. Yorita *et al.*: Phys. Lett. B**476** (2000) 226.

[4] B. Kursche *et al.*: Phys. Rev. Lett. **74** (1995) 3736.

[5] C.S. Armstrong *et al.*: Phys. Rev. D**60** (1999) 052004.

Momentum Distribution of η Meson on A(γ, η) Reaction

H. Yamazaki[1], T. Yorita[1]*, T. Kinoshita, T. Okuda[1], H. Matsui[1], J. Kasagi[1], T. Suda[2]†, K. Itoh[3], T. Miyakawa[3], H. Okuno[4], H. Shimizu[5]*, H.Y. Yoshida[5], T. Kinashi[5] and T. Maruyama[6]

[1]*Laboratory of Nuclear Science, Tohoku University, Mikamine, Sendai 982-0826.*
[2]*Department of Physics, Graduate School of Science, Tohoku University, Sendai 980-8578.*
[3]*Department of Applied Physics, Tokyo University of Agriculture and Technology, Koganei, Tokyo 184-8588.*
[4]*Institute of Particle and Nuclear Studies (KEK-Tanashi), Tanashi, Tokyo 188-0002.*
[5]*Department of Physics, Yamagata University, Yamagata 990-8560.*
[6]*Collage of Bio resource Sciences, Nihon University, Fujisawa 252-8510.*

The interaction between a meson and a nucleon is one of the most basic interactions to describe the nuclei. The charged pion reaction cross sections on a nucleon were measured in wide kinematic conditions, and the coupling constant $g_{\pi NN}$ was determined. On the other hand, we have little information on the interactions between a nucleon and heavier mesons, such as η and ρ mesons. They play a major role on the short range nuclear force. Thus, it is very important to investigate the interaction between a nucleon and heavier mesons. The measurement of the meson photo production cross sections is one of the useful ways to determine the meson-nucleon interaction, because interactions between photon and nucleon are well understood. Thus, we have measured the momentum differential cross section of photo-η meson production on C, Al and Cu.

Experimental details are described in ref. [1], and here, we report on the results of the analysis of the momentum distributions of η mesons.

In Fig.1, the differential η photo production cross sections are shown as a function of emitted η meson momentum. Open circles, closed circles and squares correspond to the obtained differential cross sections of the (γ,η) reaction on C, Al and Cu, respectively. The reaction cross sections on C, Al and Cu have similar dependence on emitted η momentum. The cross section shows the maximum value at around 400 MeV/c. In order to clarify the cause of the phenomena, we have performed the calculation based on the semi-classical model, Quantum Molecular Dynamics (QMD). QMD was originally developed to describe the high energy heavy ion reactions [2]. We have modified the QMD code to describe the photon induced η production. A solid line corresponds to the results of QMD calculation which assumes that the η-N reactions only occur via S_{11} (1535) nucleon resonance. In this calculation, the η reaction cross section was deduced from the detailed balance analysis of the $\pi^- p \rightarrow \eta n$ cross section. The deduced reaction cross section is displayed as the solid line in Fig.2. These results in Fig.1 almost reproduce the data, but have slightly higher peak positions. It means that assumed reaction cross section is overestimated at the low-momentum region less than 400 MeV/c, and underestimated at

*Present address : RCNP, Osaka University, Ibaraki, 567-0047.
†Present address : RIKEN, Wako, 351-0198.

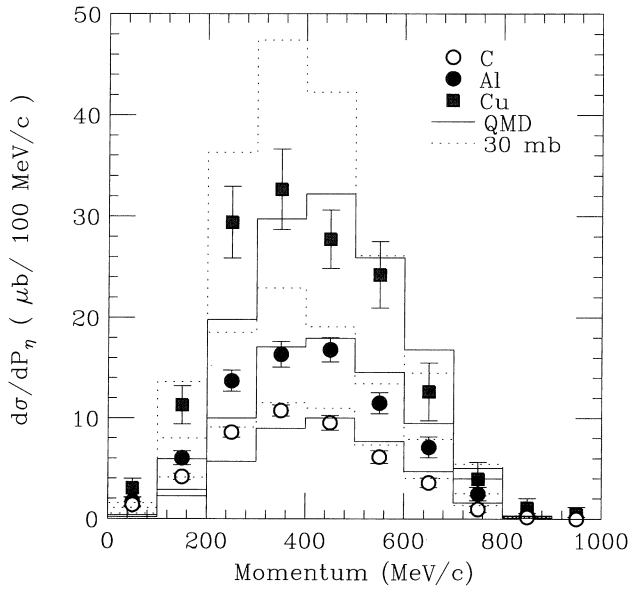

Fig.1. Differential cross sections of (γ,η) reactions on C, Al and Cu as a function of η momentum. Open circles, closed circles and squares show the results on C, Al and Cu, respectively. Solid lines show the results of QMD calculations assuming that the η-N reactions only occur via $S_{11}(1535)$ nucleon resonance. Dotted lines show the results assuming constant reaction cross sections of η mesons, 30 mb.

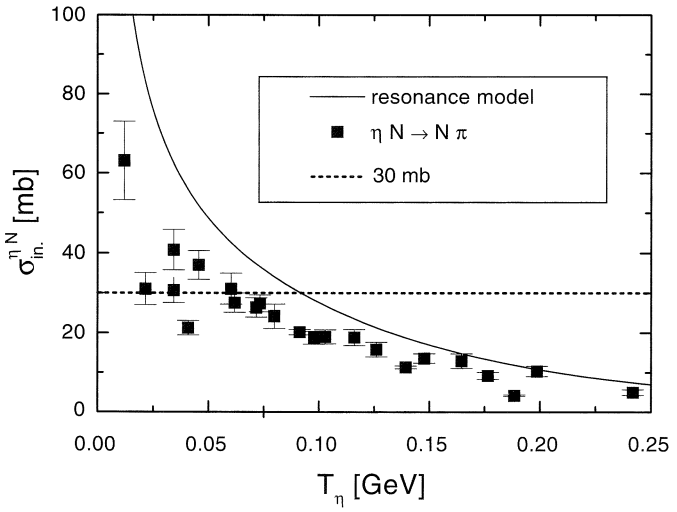

Fig.2. The absorption cross sections of η meson on nucleon, used in the QMD calculations. Squares show the η N $\rightarrow$ π N reaction cross sections deduced from the detailed balance analysis of the π p$\rightarrow$ η n cross section. Solid lines show the resonance model, and dotted line shows the constant reaction cross section of η mesons proposed by M. Effenberger *et al* [3].

the high-momentum region. As a comparison, another calculations are carried out by using constant η-N reaction cross section. Dotted lines correspond to constant reaction cross sections of η mesons, 30 mb, which were obtained by M. Effenberger and A. Sibirtsev from the analysis of the(γ,η) differential cross sections within the Glauber approximation [3]. Their analysis indicates that the η-N reaction cross section is almost independent of the η energy up to 200 MeV. These are the extreme examples that have the opposite momentum dependence to resonance model (see the dotted line in Fig.2). The results can reproduce the peak position, but fail to explain the absolute value of the cross section on Al and Cu. Future analysis to deduce the phenomenological η-N interaction are in progress.

References

[1] Y. Yorita *et al.*: Phys. Lett. **B476** (2000) 226.

[2] K. Niita *et al.*: Phys. Rev. C**52** (1995) 2620.

[3] M. Effenberger and A. Sibirtsev: Nucl. Phys. **A632** (1998) 99.

Experiments at MIT-Bates

T. Tamae

Laboratory of Nuclear Science, Tohoku University, Mikamine, Taihaku-ku, Sendai 982-0826

We have been collaborating with a group of University of Massachusetts since 1988 for experiments at MIT-Bates. Bates Experiment #89-09 (Measurement of the Elastic Magnetic Form Factor and the Threshold Breakup of ^{3}He at High Momentum Transfer) was accepted in 1989 and performed in 1997. Data analysis of the experiment was completed using one and a half years. A new proposal, Bates-Experiment #97-03 (Virtual Compton Scattering on the Proton Below Pion Threshold) has been scheduled in the early summer of 2000.

I. Bates Experiment #89-09 Measurement of the Elastic Magnetic Form Factor and the Threshold Breakup of ^{3}He at High Momentum Transfer[1]

The ^{3}He elastic magnetic form factor was measured at five different momentum transfers between $Q^2 = 5.75$ and 42.6 fm^{-2}; the two highest points are in the unexplored region. The experiment was performed at the MIT-Bates Linear Accelerator Center using a 1% duty-factor electron beam and a high-density cryogenic ^{3}He gas target. Scattered electrons were detected with a magnetic spectrometer (OHIPS) at a scattering angle of 160°. The ^{3}He target system was operated at a temperature of 23 K and a pressure of 50 atm. The length of the target cell was 19.6 cm. The spectrometer detector system consisted of two layers of vertical drift chambers for tracking, a gas Cherenkov detector and a lead-glass shower counter for particle identification, and three layers of plastic scintillators for triggering and timing.

Figure 1 compares our magnetic form factors to previously published values; Coulomb contributions were assessed from the sum-of-Gaussian fit to published results. The new data at $Q^2 =$ 18.8 and 21.8 fm^{-2} agree with existing data, which consequently strengthen the conclusion that the diffraction minimum lies close to $Q^2 = 18$ fm^{-2}. In contrast, data at $Q^2 = 36.3$ and 42.6 fm^{-2} appeared considerably smaller than what would be anticipated by extrapolating the existing Saclay results. The calculations represented in Fig.1 are by Hadjimichael *et al.* [1], Marcucci *et al.*[2], and Strueve *et al.*[3], as well as by impulse approximation (IA).

In calculations without non-nucleonic effects, a diffraction minimum of the squared magnetic form factor $|F_M(Q^2)|^2$ of ^{3}He due to a destructive interference between S- and D-state components of the

[1]Collaboration: Tohoku University (I. Nakagawa, T. Suda, T. Tamae), University of Massachusetts (J. Shaw, S. Churchwell, X. Jiang, B. Asavapibhop, M.C. Berisso, P.E. Bosted, K. Burchesky, R.S. Hicks, A. Hotta, R.A. Miskimen, G.A. Peterson, S.E. Rock, K. Wang), MIT-Bates (F. Casagrande, W. Turchinetz), University of Virginia (A. Cichocki), Teikyo University (T. Kobayashi)

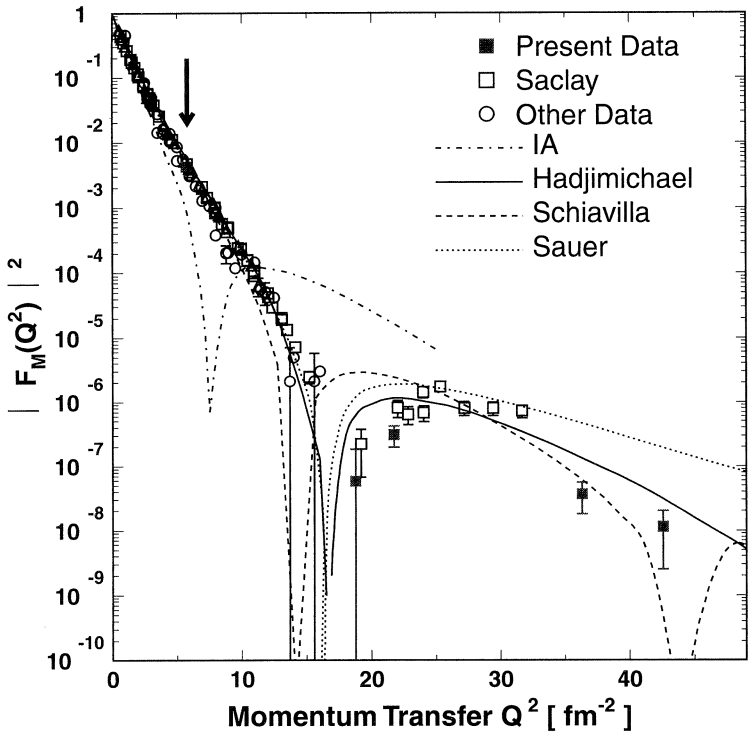

Fig.1. The elastic magnetic form factor of ^{3}He. Present results are represented by solid squares, Saclay data [4] by open squares, and other data [5] by open circles. The arrow indicates our measurement at Q^2 = 5.75 fm^{-2}.

ground state wave function lies near Q^2= 8 fm^{-2}, in striking disagreement with the experimental results. A dramatic upward shift in Q^2 is qualitatively explained by calculations that include meson-exchange and Δ-isobar currents. Significant differences are observed in the various theoretical predictions at $Q^2 \geq 30$ fm^{-2}. For the high momentum transfers probed in this experiment, the theoretical results are sensitive to the non-nucleonic effects, and also to the assumed form of the nucleon form factor. The calculation by Marcucci *et al.* predicts the first diffraction minimum at too low Q^2. The trend of the calculation by Strueve *et al.* is to overestimate the high Q^2 results by an order-of-magnitude. This may be due to the large Δ-isobar component in the model. Although the prediction of Hadjimichael *et al.* remains close to the experimental results for $F_M(Q^2)$ throughout the entire Q^2 range, the Coulomb form factor of ^{3}H calculated by this group lies far from the data. In conclusion no existing theoretical calculation satisfactorily accounts for the available data of the both trinucleons ^{3}H and ^{3}He. In the kinematical region spanned by our data there is mounting theoretical evidence of the need to consider relativistic dynamics and quark-gluon degrees-of-freedom. Additional incentive for further theoretical developments is provided by a planned experiment [6] at Jefferson Laboratory that seeks to measure the ^{3}He magnetic form factor out to $Q^2 > 60$ fm^{-2}.

References

[1] E. Hadjimichael, B. Goulard, and M. Bornais: Phys. Rev. C**27** (1993) 831.

[2] L.E. Marcucci, D.O. Riska, and R. Schiavilla: Phys. Rev. C**58** (1998) 3069.

[3] W. Strueve, Ch. Hajduk, P.U. Sauer, and W. Theis: Nucl. Phys. **A465** (1987) 651.

[4] J.M. Cavedon *et al.*: Phys. Rev. Lett. **49** (1982) 986.
A. Amroun *et al.*: Phys. Rev. Lett. **69** (1992) 253 ; Nucl. Phys. **A579** (1994) 596.

[5] H. Collard *et al.*: Phys. Rev. **138** (1965) B57.
M. Bernheim *et al.*: Lett. Nuovo Cimento **5** (1972) 431.
J.S. Mc Carthy *et al.*: Phys Rev. C**15** (1977) 1396.
P.C. Dunn *et al.*: Phys. Rev. C**27** (1983) 71.
C.R. Ottermann *et al.*: Nucl. Phys. **A436** (1985) 688.
D.H. Beck *et al.*: Phys. Rev. Lett. **59** (1987) 1537.

[6] G.G. Petratos *et al.*: JLab proposal E89-021.

Experiments at JLab

T. Terasawa

Laboratory of Nuclear Science, Tohoku University, Mikamine, Taihaku-ku, Sendai 982-0826

Several researchers in Tohoku group visited JLab for the preparations for the hypernuclear experiment. Tohoku group took charge of making a new scattering chamber and a vacuum duct, which were manufactured in Japan, and accomplished and send to JLab in 1998. Then, we waited for the completion of the septum magnets in order to allow experiments at very forward angles. The contract to make two super-conducting septum magnets was signed in September, 1998 between JLab and BWX Technologies at Lynchburg, VA. The initial schedule to ship the magnet to allow mapping and testing before 31 December 1999 delays about a year. The new schedule for the hypernuclear experiment will be after the 2001 summer shutdown. The hypernuclear experiment in Hall A is a collaboration among INFN, Tohoku University, University of Maryland, Florida International University and JLab. The meeting of the experiment is held always in JLab. Participation in such a meeting is one of the most important activities of the collaboration and we visited JLab to participate such meetings. They were, (1) T. Saito and H. Tsubota visited JLab in a period from 20th of May to 1st of June for the attendance of the Hall A meeting. (2) T. Saito and Y. Shibasaki visited JLab in a period from 30th of October to 10th of November for the attendance of the Hall A kaon collaboration meeting. (3) S.Kato visited JLab in a period from 30th of November to 6th of December for the attendance of the meeting of the septum magnet. (4) H. Tsubota visited JLab in a period from 8th to 19th of December for the attendance of the Hall A meeting. (5) T. Tamae and K. Maeda visited JLab from 20th of February to 19th of March for the attendance of the Hall A kaon collaboration meeting. In these meetings, a need to construct a Ring Image Cherenkov counter (RICH) is discussed which have a rejection of protons and pions of 10-4 compared with 0.05 obtained by the standard method using two aerogel Cherenkov counters. K. Takahashi visited Instituto Superiore di Sanita in Italy from 25th of May to 28th of February, 2000 for the construction of RICH. The standard method of PID were also developed by Frolida Intern. Univ., and a test experiment for the PID using aerogel Cherenkov counters was held in JLAB in August. T. Terasawa visited JLab from 30th of Jury to 10th of August for the participation of the experiment. Altogether 9 researchers visited JLab for the preparations of the hypernuclear experiment in Hall A for about 2 weeks per person. Our plan to run a hypernuclear experiment in Hall A is not yet realized. The reason that the experiment is behind the schedule is the delay of constructing super-conducting septum magnets. Most optimistic schedule to install the septum magnets in Hall A will be Spring, 2001. The travel money was paid from a grant-in-aid from the Japanese Ministry of Education, Science and

[1]The members of the group are T. Saito (representarive), O. Hashimoto, J. Kasagi, T. Nakagawa, H. Tsubota, T. Terasawa, T. Tamae, K. Maeda, O. Konno, H. Yamazaki, H. Ueno and S. Kato.

Culture with a contract number 10044055.

Ⅱ. Radiochemistry

Laser Induced Photoacoustic Spectroscopy Applied to a Study on Tc (IV) Colloid Coagulation Processes

T. Sekine, S. Kino, Y. Kino and H. Kudo

Department of Chemistry, Graduate School of Science, Tohoku University, Sendai 980-8578

Laser induced photoacoustic spectroscopy (LPAS) was applied to determination of the concentration and size of colloid particles in aqueous solutions. The intensity of photoacoustic signals for mono-dispersed polystyrene particles in different sizes was linearly increased with an increase of the polystyrene concentration, while the proportionality was dependent on the particle size. Furthermore, dynamic measurements of colloid-particle growing of gold sols produced by the reaction of aurate ions ($AuCl_4^-$) with sodium citrate was made by means of LPAS. The intensity of photoacoustic signals for polystyrene and gold particles was successfully calculated as a product of the number of particles and the absorption cross section per particle based on the Mie's light scattering theory. With this technique, the coagulation of Tc(IV) colloids prepared by the reduction of TcO_4^- with Sn(II) was observed. The observed growth rate of colloid particles was successfully analyzed by a newly developed collision model, in which both the distribution of the kinetic energy of particles and the potential barrier between the two particles played significant roles.

§ 1. Introduction

Nuclear waste management and disposal at deep underground has attracted interest in migration of long-lived radionuclides in the environment. One of the research subjects is elucidation of formation processes of colloids or pseudo-colloids of radionuclides [1-3], and their migration from a nuclear waste repository contacting with groundwater. Technetium-99 is one of the most important fission products with a long half-life (2.1×10^5 y). In deep groundwater under reducing conditions, pertechnetate is reduced to Tc(IV) in the chemical form of $TcO(OH)_2$(aq) at neutral pH. It has been suggested that if the concentration of technetium exceeds the solubility of $TcO_2\cdot nH_2O$ (solid), real-colloids of Tc(IV) is formed [4]. In addition to the formation of real-colloids, aqueous Tc(IV) is adsorbed on naturally occurring colloid particles in groundwater, giving pseudo-colloids owing to the strong adsorption properties of aqueous Tc (IV) [5,6]. However, little attention has been paid to the colloidal technetium species and knowledge on the formation as well as the stability of its real-colloids or pseudo-colloids in aqueous solutions is limited. In order to study the formation and coagulation (or flocculation) processes of colloids, dynamic measurement of changes in concentration and sizes of particles is essential.

LPAS is a well-known powerful tool not only for the speciation of chemical species in trace amounts in a solution [7,8], but also sensitive for detection of colloid particles. Sawada *et al.* [9, 10] reported the detection of ppb order of Te and $BaSO_4$ colloids. Kim *et al.* [8] observed the occurrence of plutonium hydroxide colloids from a change of intensity in photoacoustic signals in aqueous solution. Recent

advances in quantification of particles in solutions have been appeared in some reports [11-13] in which the counting of particle number and the analysis of its composition were simultaneously performed by laser induced break down spectroscopy (LIBS). Although LPAS or LIBS is highly sensitive, a relation between the intensity of normal photoacoustic signals from particles and the concentration or size of colloids has not been well generalized.

A laser light scattering method is useful for the determination of the size and concentration of particles. It is, however, normally said that the scattering method is effective to determine particle sizes larger than about 50 nm, because the scattered light disperses isotropically for smaller particles owing to an increase of the scattering cross section at larger angles. In such meaning, light absorption by particles is more effective to detection of fine particles with the size of nanometers.

In this paper, laser induced photoacoustic spectroscopy (LPAS) with the light absorption, has been applied to *in situ* observation of coagulation processes of colloid particles. In analysis of the intensity of photoacoustic signals from polystyrene particles and gold sols in different sizes and concentrations, we have adopted an absorption cross section of light per particle derived from the Mie's light scattering theory [14]. This technique is further applied for the observation of coagulation of Tc (IV) colloids, for which the formation has not been well known, and the feature of colloid particle growth is explained by a particle collision model based on the DLVO (Derjaguin-Landau-Verwey-Overbeek) theory.

§ 2. Experimental

Mono-dispersed polystyrene latex particles (diameter; 102, 212, 230, 312, 394, 474, 905, 2020, 2810 nm) were purchased from Nissin EM Co., Ltd., Bio-Rad Co., and Dow Chemical Co. The particle size was reconfirmed by means of a Scanning Electron Microscope (SEM, JEOL JFM6320F). The concentration of polystyrene in aqueous solutions was in the range from 1 to 20 $\mu g \cdot mL^{-1}$ for the LPAS measurement.

Gold particles were prepared by a method reported by Turkevich *et al.* [15]. Five milliliters of sodium citrate ($Na_3C_6H_5O_7$) solution (3.2 mmol $\cdot L^{-1}$) was added to a chloroauric acid ($HAuCl_4$) solution (5 mL, 0.48 mmol $\cdot L^{-1}$) at 60℃, and the mixture was rigorously stirred. The color of the solution gradually changed from bluish-purple to wine red as the reaction proceeded. The particle size of gold sols was measured as a function of the reaction time with a Transmission Electron Microscope (TEM, JEOL JEM-2000 EXII) and the mean size was evaluated. The amount of gold sols was determined by ultrafiltration (Ultra Filter UK-10, Toyo Roshi Kaisha. Ltd.) using a gold solution labeled with a radioactive tracer, ^{196}Au or ^{198}Au. Gold-196 was produced by the irradiation of gold foils with bremsstrahlung from a LINAC at the Laboratory of Nuclear Science, Tohoku University. Gold-198 was produced by neutron irradiation in the JRR-2 reactor of the Japan Atomic Energy Research Institute.

Ammonium pertechnetate ($NH_4{}^{99}TcO_4$) was purchased from the Radiochemical Center, Amersham. Technetium-99 was labeled with ^{95m}Tc produced by the $^{93}Nb(\alpha, 2n)\ ^{95m}Tc$ reaction [16] at Cyclotron Radioisotope Center, Tohoku University. To the labeled pertechnetate solution (60 μmol $\cdot L^{-1}$), a drop of stannous chloride solution was added to produce Tc(IV) colloids (pH = 4.4, ionic strength 10^{-4}). The amount of the Sn^{2+} ion was adjusted less than that needed for the stoichiometric reduction of

pertechnetate in the solution. The size distribution was evaluated by analysis of the sedimentation velocity of colloids in solution based on the Stokes' law, by measuring γ-rays emitted from ^{95m}Tc [17].

The LPAS system includes a nitrogen gas laser (Laser Photonics Co., UV24) and a dye laser (Laser Photonics Co., DL14) to get a suitable monochromatic pulse laser beam. The wavelength of the excitation beam was adjusted to 500 nm with a Coumarin-500 dye material. A sample solution (5 mL) in a quartz cell (1 cm×1 cm×5 cm) was submitted to the LPAS measurement, and the photoacoustic signals were detected with piezo-electric transducers (PZT) in a home made detector box of brass [18]. The photoacoustic signals from the reference solution of auric acid irradiated simultaneously were used as an index of the laser beam intensity for the normalization of sample signals. The signals were amplified with a low noise preamplifier (NF Co., AE-912) and averaged for 100 laser pulses with a digital oscilloscope (Sony Tektronix, TDS-460). The photoacoustic signal amplitude (PA) was evaluated as the intensity of main component (around 140 kHz) after the Fast Fourier Transform analysis [18,19].

§ 3. Photoacoustic Signal Intensity of Colloidal Solutions

Compression waves are generated through a thermoelastic process caused by the light absorption [20], resulting photoacoustic signals. The sound waves, generated from a particle, propagate through water and are finally converted into a voltage variation of the PZT detector. The amplitude of signals normalized to the laser power might be expressed as follows :

$$I(W, d) = \Gamma \cdot N(d) \cdot Q_{abs}(W, d) \cdot l, \tag{1}$$

where $I(W, d)$ is the PA intensity from particles with the size d in diameter, $N(d)$ the number of particles in unit volume of solution, $Q_{abs}(W, d)$ the absorption cross section of light per one particle at a given wavelength (W) of the light, l the path length of a quartz cell, and Γ a constant given for the present system.

The absorption cross section of light by spherical particles can be calculated by introducing a complex index, $x + iy$, of refraction [21]. The wave number of light, z, changes inside the particle by a factor of $(x + iy)$, and gives $z' = (x + iy)\, z$. Thus the spherical wave inside the particle is expressed as

$$e^{iz'r} = e^{ixzr} \cdot e^{-yzr}, \tag{2}$$

where r is the distance from the center of particle. The second term in Eq. (2) represents damping of the spherical wave in the particle, that is the absorption.

Based on the above concept, we can calculate the absorption cross section for polystyrene and gold sols by assuming that the particle is a sphere [21]. The calculated cross sections per one particle at wavelength of 500 nm are plotted against the size of particles in Fig.1. (a) and (b), for polystyrene and gold sols, respectively. The complex indexes of refraction for polystyrene and gold were taken from the literature [22], but the value of y for polystyrene was not reported and assumed as 0.08. This value was reasonably adopted to give a consistency between experimental and calculated values with Eq. (1) shown later. The absorption cross section of polystyrene is smaller than the scattering cross section in the range up to 1.5 μm, suggesting that the scattering method might be superior to LPAS method to

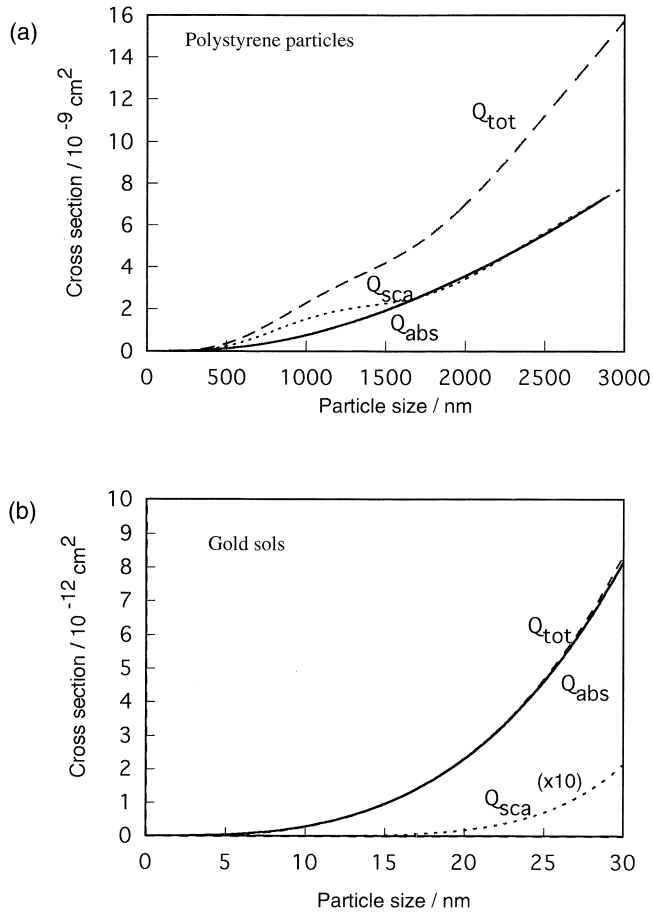

Fig.1. The calculated cross sections per one particle at wavelength of 500 nm. (a) polystyrene particles (the complex index of refraction; x = 1.6, y = 0.08) (b) gold particles (the complex index of refraction; x = 1.0, y = 2.4) solid line: absorption cross section (Q_{abs}), dotted line : scattering cross section (Q_{sca}), broken line; total extinction cross section (Q_{tot}).

effectively detect particles with the size around 1 μm. More or less the same is true for a larger size of polystyrene. On the other hand, the absorption cross section for the gold particle of nanometers is much larger than the scattering cross section. Hence, the LPAS method with light absorption would be more effective to detect the ultrafine particles.

The experimentally obtained amplitude of photoacoustic signals was compared with the theoretical values calculated from the relation of Eq.(1) for polystyrene and gold particles.

§ 4. Results and Discussion

4-1. Polystyrene particles

The PA intensity (the peak height around 140 kHz peak after the FFT analysis) is plotted against the concentration of polystyrene in Fig. 2. A linear relation is observed for each polystyrene sample, while the proportionality is different. The fact suggests that the PA intensity does not depend only on the amount of polystyrene in the solution. In order to clarify the relation between the PA intensity and the polystyrene concentration depending on the particle size, the PA intensity measured at the constant concentration (10 μg・mL^{-1}) is plotted against the particle size in Fig. 3. The PA intensity increases with an increase of the particle size, and reaches a maximum around 250 nm, and then gradually decreases in a region of larger sizes. A broken line in Fig.3 shows the values calculated by Eq.(1) with

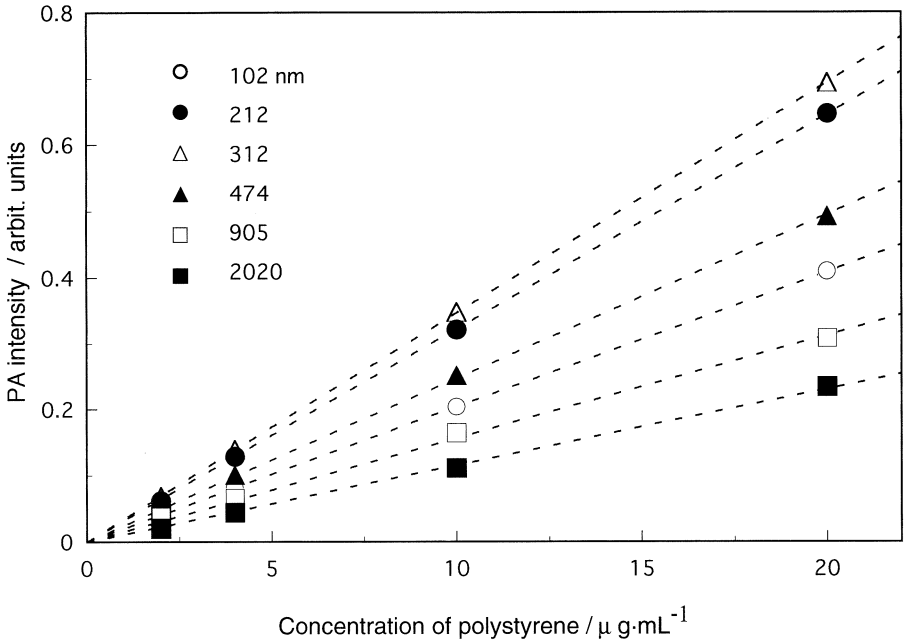

Fig.2. The relation between the PA intensity and the concentration of polystyrene.

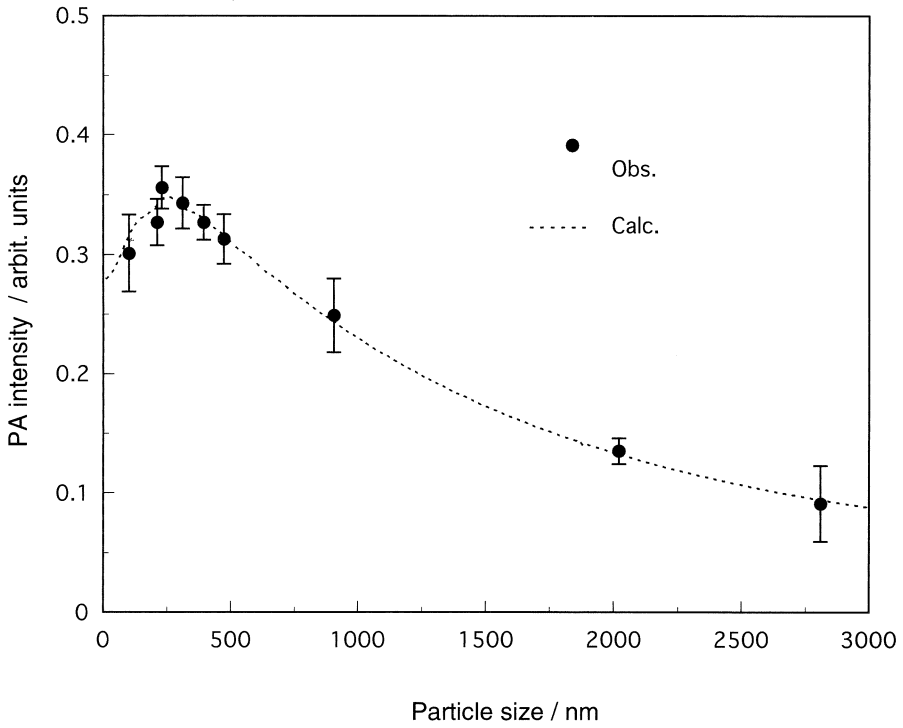

Fig.3. The PA intensity change depending on the polystyrene particle size at the constant concentration of polystyrene ($10\,\mu g \cdot mL^{-1}$). The broken line shows the calculated PA intensity using Eq. (1).

the absorption cross section shown in Fig.1(a) and the number of particles in the unit volume of solution. The calculated values agree reasonably with the experimental values when the constant, Γ, in Eq.(1) is 16.5.

The characteristic features on the PA intensity from particles are as follows. If the size of the particle is much smaller than $1 / z \cdot y$ (reciprocal of product of wave number and imaginary part of optical constant), the PA intensity is approximately in proportion to $\varepsilon \cdot C$ (product of molecular absorption

coefficient and concentration). In general, however, absorption depends strongly on the interference between incoming and outgoing wave, which sometimes causes a resonance, and the light path in the particle, which is actually described by the partial wave expansion [21]. Calculating the absorption cross section Q_{abs} in Eq.(1), we took these effects into account exactly with the Mie' s framework.

Kitamori *et al.* [23] reported anomalous enhancement of photoacoustic signals, when the particle size of polystyrene is close to the wavelength of an excitation beam. They accounted this enhancement for the effect of resonance scattering. However, we have not observed such a scattering effect. We used a pulse laser beam in our LPAS system, while they used CW laser system. The photoacoustic sounds generated in a pulse system would reach the detector after the scattered light gave noise signals. In the present measurement, the duration of a laser pulse was short (10 ns), and the real signals from the light absorption were completely separated from the noise signals due to the scattering.

The validity of the model for the calculation of the PA intensity of polystyrene particles based on the absorption of light by particles, expressed by Eq.(1), was confirmed in the present experiment with pulsed laser.

4-2. Gold sols

The experimental results on the average particle size and the amount of colloids formed for gold sols are summarized in Table 1. The size of gold sols formed in a mixture of auric acid and sodium citrate solutions was determined by TEM. This observation revealed that the particle shape was spherical as a whole. The average size of gold sols changed with the reaction time. The size was gradually enlarged as the reaction proceeded, from 5 nm at 30 min to 20 nm at 4 h, and reached a constant size. A similar tendency was also reported by Takiyama [24] and Seshadri *et al.* [25].

The quantity of gold sols, determined by ultrafiltration, was found to increase with increasing time (Table 1). Although both the size and the amount of sols increased, the number of particles in the solution, which was calculated from the mean size and amount of gold sols, decreased with time (Table

Table 1. The results of the size and amount of gold sols depending on the rection time.

Reaction time/min	Average size of partiles*/nm	Amount of colloids $/10^{-4}$ mol · L^{-1}	Number of particles** $/10^{11}$ mL^{-1}	Q_{abs}** $/10^{-14}$ cm^2
30	4.5±1.2	0.20±0.07	43	2.5
60	8.5±1.4	0.43±0.07	13.7	17.0
90	12±1.1	0.58±0.06	6.5	48.3
120	15±0.8	0.76±0.05	4.4	95.2
180	18±0.9	1.13±0.06	3.8	166
240	19±1.0	1.25±0.06	3.6	197
360	20±1.0	1.16±0.06	3.1	213
480	20±1.0	1.18±0.06	2.8	230

*Average for 250 particles observed by TEM, and the mean error is shown.

**Number of particle in the unit volume of solution calculated from the average size and amount of gold sols.

***The calculated absorption cross section of gold particles at wavelength of 500 nm (the complex index of refraction; $x = 1.0$, $y = 1.6$).

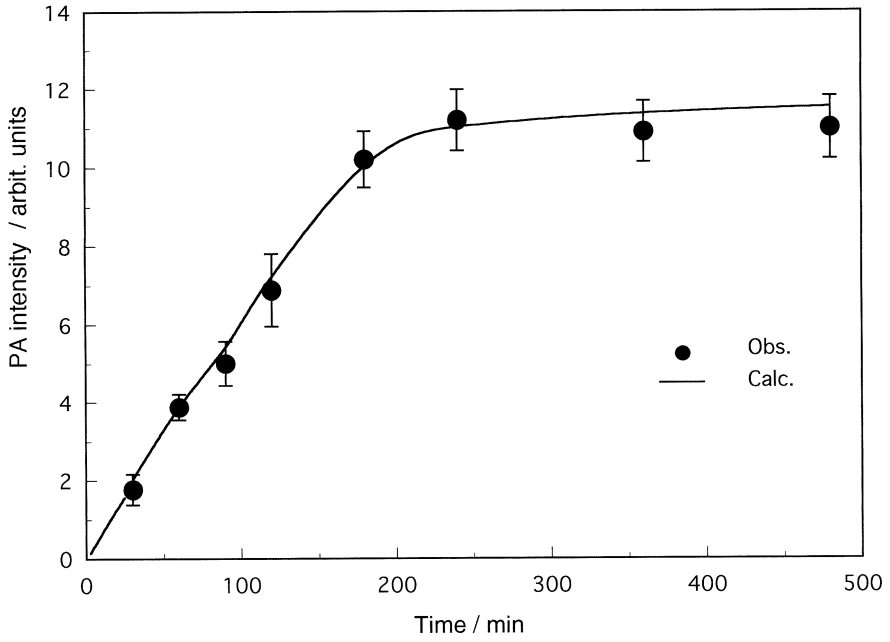

Fig.4. The PA intensity change of the gold sols solution depending on the reaction time. The solid line exhibits the calculated PA intensity using Eq.(1).

1). The result suggests that the gold sols were formed not only through the reduction of the aurate ions to feed gold atoms, but also through simultaneous coagulation of small particles.

The PA intensity was changed with the reaction time as shown in Fig.4. Reliability of the model to obtain the PA intensity was examined by introducing the number of particles in the unit volume of solution and the absorption cross section per one particle (in Fig. 1(b)). The evaluated PA intensity is shown with a solid line in Fig.4 with the Γ value of 16.5 that was given in the case of polystyrene particles. The constant Γ in Eq.(1) that was independently calculated from the data for gold sols was given as 16.5 $\pm$ 0.2. The calculated values agreed well with the observed values, and the reliability of the model was confirmed. Furthermore, the value of Γ is consistent with that given for polystyrene particles described above. Conclusively, the evaluation of the absorption cross section is reasonable for the cases of polystyrene and gold particles.

Thus, the sensitivity of particles can be calculated by Eq.(1). The PA intensity strongly depends on the absorption cross section per particle, Q_{abs}, in Eq.(1), as shown in Table 1. Since our LPAS system has detection limit of $10^{-4} \sim 10^{-3}$ cm^{-1}, the detection limit as particle number per unit volume varied from 10^{9} to 10^{6} cm^{-3} with the diameter change from 5 to 20 nm for gold sols, and varied from 10^{7} to 10^{3} cm^{-3} with the diameter from 100 to 2800 nm for polystyrene particles.

4-3. Tc(IV) colloids

The colloid formation of Tc(IV) has not been well understood, although the colloids would be formed at the concentration region near its solubility [26]. We examined the colloid formation through reduction of pertechnetate with stannous ions in the technetium concentration from 10^{-8} to 10^{-4} mol $\cdot$ L^{-1}, and found the gradual coagulation even at concentration as low as 60 μmol $\cdot$ L^{-1}. We have applied the LPAS method to the observation of this coagulation process.

The PA intensity observed for the pertechnetate solution after addition of stannous ions decreased

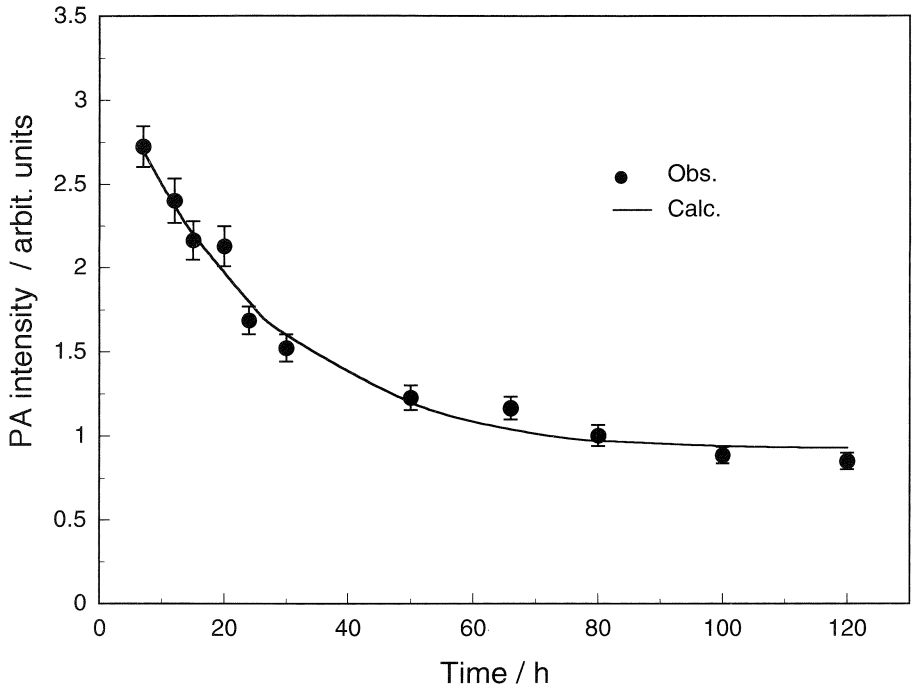

Fig.5. The PA intensity change for the solution containing Tc(IV) colloids against the standing time. The calculated PA intensity assuming the complex index of refraction of Tc(IV) colloids as $x = 1.3$ and $y = 0.6$ is shown as the solid line.

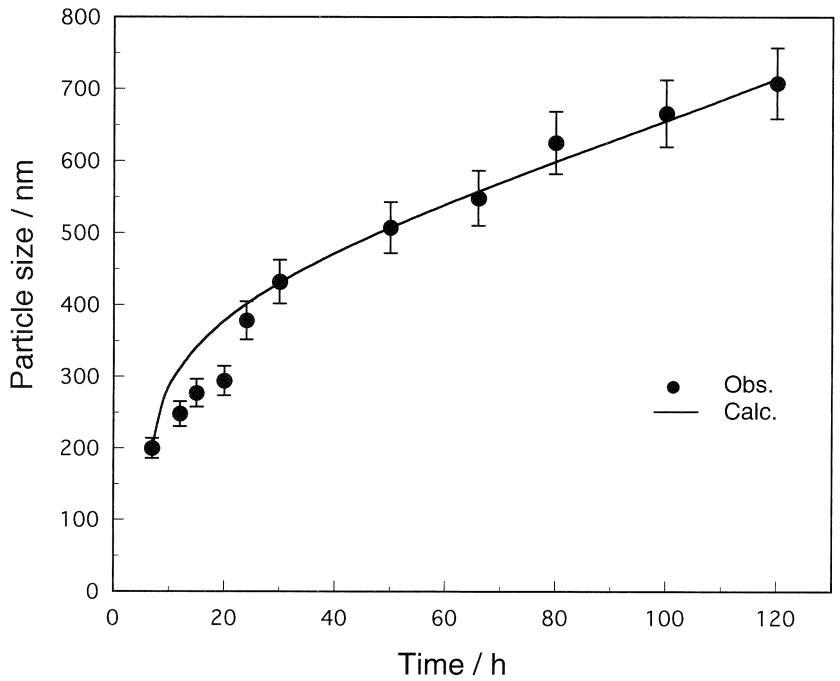

Fig.6. Size of Tc(IV) colloid particles in aqueous solution (pH 4.4, ionic strength 10^{-4}) against standing time. Data in the figure are the averaged values for 5 times experiments. The solid line is the result calculated based on the coagulation model described in the text (the Hamaker coefficient $1.8 \cdot 10^{-19}$ J, the surface potential 24 mV).

monotonously with increasing time as shown in Fig.5. The size of the particles increased from 200 nm at 7 h to 700 nm at 120 h as shown in Fig.6, while the total amount of colloids in the solution was constant (concentration of technetium as colloids = $4 \cdot 10^{-5}$ mol $\cdot$ L^{-1}) independent of the standing time up to 5 days [17]. The results reveal that the particles have grown only by the coagulation process of

small particles formed at the initial stage, in contrast to the case of gold sols.

Using Eq.(1) with Γ = 16.5, we have calculated the optical parameters of the complex index of refraction for Tc(IV) colloids at 500 nm. The best fit (a solid line in Fig.5) was obtained with x = 1.3 and y = 0.6. When we compare the absorption cross section with the scattering cross section calculated with these set of refractive indexes, the absorption cross section is larger than the scattering cross section up to the particle size of about 0.5 μm. The result indicates that the LPAS method employed here is effective to observe the colloid formation process of ultrafine particles.

4-4. Analysis of coagulation of Tc(IV) colloid particles

A particle collision model or the DLVO (Derjaguin-Landau-Verwey-Overbeek) theory [27] is used to explain coagulation of colloids. The theory is based on the short range attraction inside the repulsive Coulomb barrier, ΔE. We applied the following model to explain the growth of Tc(IV) colloids as an example.

To solve the problem practically, we assume the Maxwell-Boltzmann distribution

$$P(v) = \sqrt{\frac{2}{\pi}}\left(\frac{m}{kT}\right)^{\frac{3}{2}} v^2 \exp\left(-\frac{mv^2}{2kT}\right) \quad , \tag{3}$$

for the number of colloid particles with kinetic energy $E = mv^2/2$, where m, v are particle weight and velocity, respectively, and k the Boltzmann constant, T the temperature. It is reasonable to consider that the particles with kinetic energy high enough to exceed the barrier can coagulate each other in collision from the DLVO theory.

The number of particles, N, in the unit volume of solution is given by

$$N = \frac{CM}{m} = \frac{3CM}{4\pi a^3 \rho_P} \quad , \tag{4}$$

where C is the mole concentration, M the molecular weight, a the particle radius and ρ_p the density of colloid particles. From Eq.(4) the differential change in the number of particles dN/dt is given by

$$\frac{\mathrm{d}N}{\mathrm{d}t} = -\frac{9CM}{4\pi a^4 \rho_P}\frac{\mathrm{d}a}{\mathrm{d}t} \quad , \tag{5}$$

On the other hand, since a decrease of the number of particles is due to coagulation of the colloid particles, dN/dt is also given by

$$\frac{\mathrm{d}N}{\mathrm{d}t} = -\int_{v_x}^{\infty} v_c N \sigma(v) P(v) dv \quad , \tag{6}$$

where, $v_x = \sqrt{\frac{2\Delta E}{m}}$ is the minimum velocity which exceeds the barrier, $\sqrt{\sigma}(v)$ the coagulation cross section described below and v_c the relative velocity between the two particles. For the value of v_c, we actually use $\sqrt{2}$, which is averaged over the collision angle.

Because the strong attractive potential in DLVO potential exists near the surface of the particles, we have to take the centrifugal barrier into account in addition to the DLVO interaction. The centrifugal potential $V_{cen}(r)$ is given by

$$V_{cen}(r) = \frac{(\mu b v_c)^2}{2\mu}\frac{1}{r^2} = E\frac{b^2}{r^2} \quad , \tag{7}$$

where $\mu = m/2$ is the reduced mass of two particles, b the impact parameter, r the distance between two particles. Note here, $E = mv^2/2 = \mu v_c{}^2/2$. Setting $r = 2a$ in Eq.(6), the total barrier between the two particles is estimated at $\Delta E + E \cdot b^2/(4a^2)$. The following condition needs to be satisfied in order that coagulation takes place.

$$\Delta E + E\frac{b^2}{4a^2} \le E \quad , \tag{8}$$

and then

$$\pi b^2 \le 4\pi a^2\left(1 - \frac{\Delta E}{E}\right) \quad , \tag{9}$$

Here, $4\pi a^2$ corresponds to the geometrical cross section. If the kinetic energy is the same as ΔE, only a head-on reaction takes place. Otherwise, if the kinetic energy is high enough, a peripheral reaction is also possible. Therefore, it is appropriate to assume the coagulation cross section as

$$\sigma(v) = 4\pi a^2\left(1 - \frac{\Delta E}{E}\right) \quad , \tag{10}$$

From above Eqs. we have

$$-\frac{9CM}{4\pi a^4 \rho_P}\frac{\mathrm{d}a}{\mathrm{d}t} = -\int_{v_x}^{\infty}\sqrt{2}v\frac{3CM}{4\pi a^3\rho_P}\sigma(v)\sqrt{\frac{2}{\pi}}\left(\frac{m}{kT}\right)^{\frac{3}{2}}v^2\exp\left(-\frac{mv^2}{2kT}\right)\mathrm{d}v \quad , \tag{11}$$

With analytical integration for the integral term in Eq.(11), we reach the following differential equation for the particle radius

$$\frac{\mathrm{d}a}{\mathrm{d}t} = \frac{2\sqrt{3}}{\pi}\frac{CM\sqrt{kT}}{\rho_P{}^{3/2}}\exp\left(-\frac{\Delta E}{kT}\right)a^{-3/2} \quad , \tag{12}$$

We can solve the Eq. (12) numerically to simulate the growth of colloid particles.

The fitting was performed on the experimental results for the gradual coagulation at 10^{-4} of ionic strength. In the fitting, we have set the density of Tc(IV) colloids as a constant irrespective to the particle growth. The x-square fit was made using the Hamaker coefficient and the surface potential involved in the DLVO interaction as the fitting parameters. In practical calculations, a choice of these parameters was strongly limited, because of the non-linearity of the equation and the singularity at a = 0. The results of fitting are shown as a solid line in Fig. 6, together with the experimental data. The

Hamaker coefficient was obtained as $1.8 \cdot 10^{-19}$ J and the surface potential was 24 mV. These values seem reasonable compared with generally accepted for other kind of colloids [28]. Although density and surface potential were assumed to be constant irrespective of the particle sizes in the calculation, the solid line in Fig.5 shows it reliable to explain the growth of Tc(IV) colloid particles through coagulation.

§ 5. Conclusion

The PA intensity due to light absorption in colloid particles was quantitatively expressed as a product of the number of particles and the absorption cross section of particles irrespective of kind of particles. The LPAS method employed here is applicable to examining the colloid formation and coagulation processes with a wide range of particle size from nanometer to micrometer. Furthermore, the present method was useful for the determination of a refractive index of particles suspended even in a liquid medium.

By applying the DLVO theory to analysis of experimental data, the growth of Tc(IV) colloid particles was found to proceed through coagulation of small particles. Namely, the coagulation took place between two small particles whose kinetic energy was larger than the potential barrier.

Acknowledgment

The authors acknowledge to Dr. T. Ohtsuki and the machine groups of LINAC at the Laboratory of Nuclear Science, Tohoku University, and the crew of Cyclotron Radioisotope Center, Tohoku University, for their assistance in irradiation. They also wish to thank Prof. Dr. Y. Shono and Dr. M. Kikuchi of Institute for Materials Research, Tohoku University, and the staff of High Voltage Electron Microscope Laboratory, Tohoku University, for their help in the measurement of micro particles by SEM and TEM.

References

[1] J.I. Kim, B. Delakowitz, P. Zeh, D. Klotz and D. Lazik : Radiochim. Acta **66/67** (1994) 165.

[2] D.I. Kaplan, P. M. Bertsch, D.C. Adriano and K. A. Orlandini : ibid. **66/67** (1994) 181.

[3] S.Nagasaki, S. Tanaka and A. Suzuki : ibid. **66/67** (1994) 207.

[4] J.A. Rard: In : Lawrence Livermore Nat. Lab. Report UCRL-53440, 1983.

[5] K.H. Lieser, B. Gleistsmann and Th. Steinkopff : Radiochim. Acta **40** (1986) 33.

[6] K.H. Lieser and Ch. Bauscher : ibid. **42** (1987) 205.

[7] T. Kitamori, K Suzuki, Y. Gohshi and K. Motojima : Anal. Chem. **58** (1986) 2275.

[8] J.I. Kim, R. Stumpe and R. Klenze : in Topics in Current Chemsitry 157 (K.Yoshihara ed.). Springer-Verlag, Berlin, 1990, p.129, and references herein.

[9] S. Oda, T. Sawada, T. Moriguchi and H. Kamada : Anal. Chem. **52** (1980) 650.

[10] M. Nomura, S. Oda and T. Sawada : J. Photoacoustics **1** (1982) 121.

[11] T. Kitamori, T. Matsui, M. Sakagami and T. Sawada : Chem. Lett. (1989) 2205.

[12] R. Knopp, F.J. Scherbaum and J.I. Kim : Fresenius' J. Anal. Chem. **355** (1996) 16.

[13] F. J. Scherbaum, R. Knopp and J.I. Kim : Appl. Phys. **B63** (1996) 299.

[14] G.Mie : Ann. Phys. (Leipzig) **25** (1908) 377.

[15] J. Turkevich, P.C. Stevenson and J. Hillier : Trans Faraday Soc. **11** (1951) 55.

[16] T. Sekine, M. Konishi, H. Kudo, K. Tagami and S. Uchida : J. Radioanal. Nucl. Chem. **239** (1999) 483.

[17] S. Naito, T. Sekine, Y. Kino and H. Kudo : Radiochim. Acta **82** (1998) 129.

[18] S. Naito, T. Sekine and H. Kudo : in Proc. Symposium on Environmental Radioactive Nuclides Impact in Asia, Sep. 6 - 8, 1996, Taipei, p.89.

[19] T. Sekine, M. Hiraga, T. Fujita, A. Mutalib and K. Yoshihara : J. Nucl. Sci. Technol. **30** (1993) 1131.

[20] C.K. Patel and A.C. Tam : Rev. Mod. Phys. **53** (1981) 517.

[21] P.W. Barber and S.C. Hill : Light Scattering by particles : Computational Methods, World Sci. Pub. Co., 1990.

[22] In : Handbook of Optics (M. Bass ed.), McGraw-Hill, New York, 1995.

[23] T. Kitamori, K. Suzuki, T. Sawada and Y. Gohshi : Anal. Chem. **59** (1987) 2519.

[24] K. Takiyama : Bull. Chem. Soc. Japan **31** (1958) 977.

[25] R. Seshadri, G.N. Subbanna, V. Vijayakrishnan, G.U. Kulkarni, G. Ananthakrishna and C.N.R. Rao : J. Phys. Chem. **99** (1995) 5639.

[26] R.E. Meyer, W.P. Arnold, F.I. Case and G.D. O'Kelley : Radiochim. Acta **55** (1991) 11.

[27] R.J. Hunter: in Foundations of Colloid Science. Vol. 1., Oxford Univ. Press, (Clarendon), London/New York, 1986.

[28] J. Visser : Adv. Colloid Interface Sci. **3** (1972) 331.

Enhanced Separation of Yttrium(III) from Iron(III) in the Presence of Complexing Agents through Supported Liquid Membrane

A. Tsuyoshi, T. Abiko, H. Hoshi and K. Akiba

Institute for Advanced Materials Processing, Tohoku University, Katahira-2, Aoba-ku, Sendai, 980-8577

The selective transport of yttrium(III) in the presence of iron(III) through a supported liquid membrane (SLM) has been performed by employing di(2-ethylhexyl)phosphoric acid (DEHPA) as a mobile carrier. Yttrium was preferentially transported across the SLM from the feed solution into the product solution of 1 M H_2SO_4. The transport of iron(III) was suppressed in the presence of complexing agents in the feed solution, and the separation of yttrium(III) from iron(III) was sufficiently enhanced by the addition of phosphoric acid or EDTA.

§ 1. Introduction

The separation of rare earth (RE) elements from iron(III) is an important subject in material processing, and solvent extraction with acidic organophosphorus compounds has been widely used for the extraction separation of RE elements [1,2]. The preferential extraction of yttrium(III) with DEHPA in the presence of iron(III) was previously performed based on the fast kinetics for yttrium extraction[3]. The extraction system is applied to the transport of metal species across a liquid membrane employing an extractant as a mobile carrier. The previous studies have demonstrated the SLM transport system, and the selective transport of yttrium(III) in the presence of iron(III) was accomplished by employing a mobile carrier of acidic organophosphorous compounds [4,5].

The present study has been performed for the improvement in the separation of yttrium(III) from iron(III) through an SLM with the aid of complexing agents for the suppression of the transport of iron(III) .

§ 2. Experimental

2.1 Materials

Di(2-ethylhexyl)phosphoric acid (DEHPA) (Daihachi Chem. Ind. Co., Ltd.) was diluted with kerosene. A radioisotope, ^{88}Y, was produced from the $^{89}Y(\gamma, n)^{88}Y$ reaction by the bremsstrahlung from a linear electron accelerator of Tohoku University, and ^{59}Fe (DuPont/NEN Research Products) was obtained as a hydrochloric acid solution. A PTFE membrane (Fluoropore FP045, Sumitomo Electric Ind.) used as an inert support has an average pore size of 0.45 μm, a porosity of 74% and a thickness of 80 μm.

2.2 Liquid membrane transport

An equipment for membrane transport comprised of an inner and outer compartments separated

by a supported liquid membrane (SLM) of 26 cm^2 impregnated with 0.02 M (M = mol dm^{-3}) $(DEHPA)_2$ (as a dimer) in kerosene. A feed solution (100 cm^3) containing 10^{-4} M each yttrium(III) and iron(III) respectively labeled with ^{88}Y and ^{59}Fe was put in the outer compartment. A stripping solution (10 cm^3) of 1 M sulfuric acid was placed in the inner compartment. These transport compartments were horizontally shaken at 100 strokes/min at 25℃. Samples were withdrawn from the feed and product solutions, and their radioactivities were measured with a well-type NaI (Tl) scintillation detector.

§ 3. Results and Discussion

3.1 Liquid-membrane transport

The transport of yttrium(III) and iron(III) was carried out through the liquid membrane impregnated with 0.02 M $(DEHPA)_2$ in kerosene. Figure 1 shows the time-dependent fractions of metal species in the feed solution of 0.5 M (H,Na)Cl_2CHCOO (pH 2.0) and the stripping product solution of 1 M H_2SO_4. The fraction of yttrium(III) in the feed solution decreases with time and that in the product solution increases and approaches to the fraction of 1 after 300 min. The transport profiles for both sides are closely symmetrical, indicating that metal species retained in SLM are negligibly small. As for iron(III), the transport is rather low, and the fraction of iron(III) transported after 300 min was about 0.7. For the sufficient separation of yttrium(III) from ion(III), it is important to suppress the iron(III) transport.

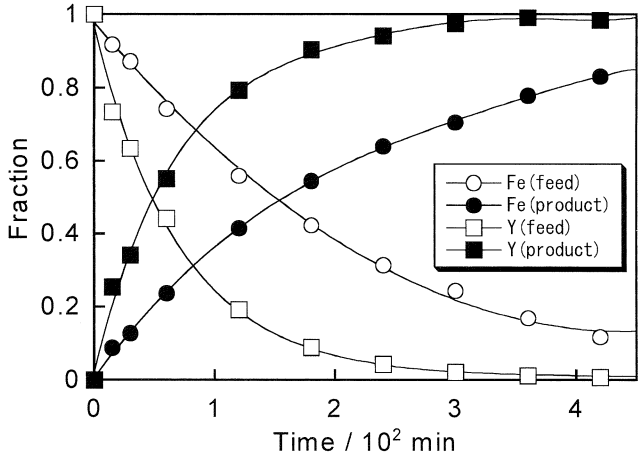

Fig.1. Transport of Y(III) and Fe(III) through SLM. SLM : 0.02 M $(DEHPA)_2$ in kerosene. Feed : 0.5 M (H,Na) Cl_2CHCOO, pH 2.0, 10^{-4} M Y(III) and Fe(III) ; product : 1 M H_2SO_4 ; 25℃.

3.2 Effect of phosphoric acid in the feed solution

Conditions on the feed side were examined by the addition of complexing agents in order to enhance the mutual separation of yttrium(III) from iron(III). Figure 2 shows the metal transport across the SLM in the presence of 0.5 M phosphate buffer (pH 2.0). The transport profiles for yttrium(III) are similar to those in the absence of phosphate, whereas the transport of iron(III) is extremely depressed due to the formation of phosphate complexes.

Figure 3 shows plots of ln $([M]_{f,t}/[M]_{f,0})$ against time t, where $[M]_{f,0}$ and $[M]_{f,t}$ are the concentrations of metal ion in the feed solution at time zero and a given time, t(s), respectively. As Fig.3 shows, a linear

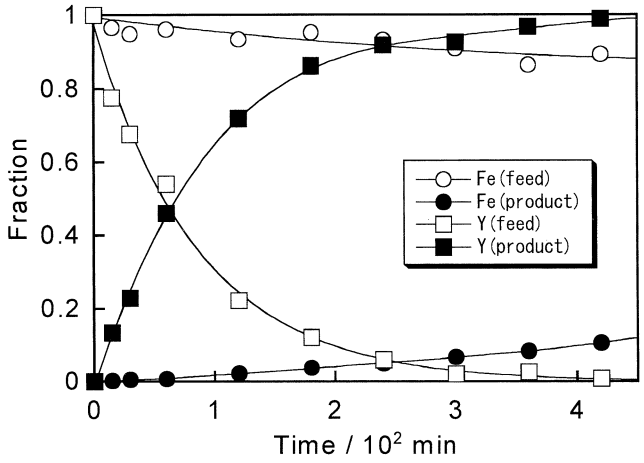

Fig.2. Transport of Y(III) and Fe(III) through SLM. SLM: 0.02 M $(DEHPA)_2$ in kerosene. Feed: 0.5 M (H,Na) H_2PO_4, pH 2.0; product: 1 M H_2SO_4.

correlation was obtained as :

$$\ln ([M]_{f,t}/[M]_{f,0}) = -k_{obs}\, t \qquad (1)$$

The apparent rate constant for metal transport, k_{obs}, can be evaluated from the slope of the linear line. Variations in k_{obs} values against phosphate buffer concentration are shown in Fig.4. The values for yttrium(III) are large and only slightly decrease with increasing concentration of phosphate buffer, while those for iron(III) more sharply decrease.

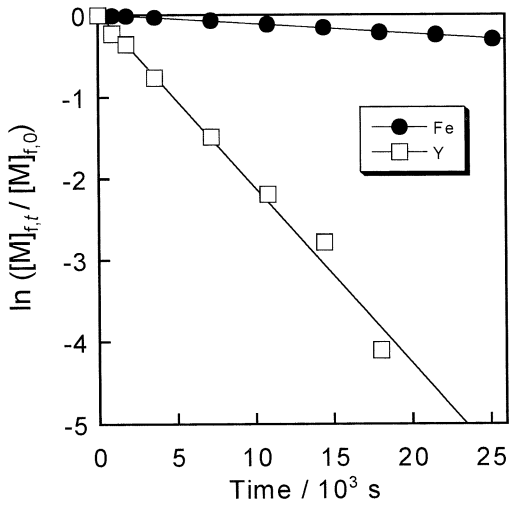

Fig.3. Decreases in the fractions of metal species on the feed side. SLM: 0.02 M $(DEHPA)_2$ in kerosene. Feed: 0.25 M (H, Na)H_2PO_4, pH 2.0; product: 1M H_2SO_4.

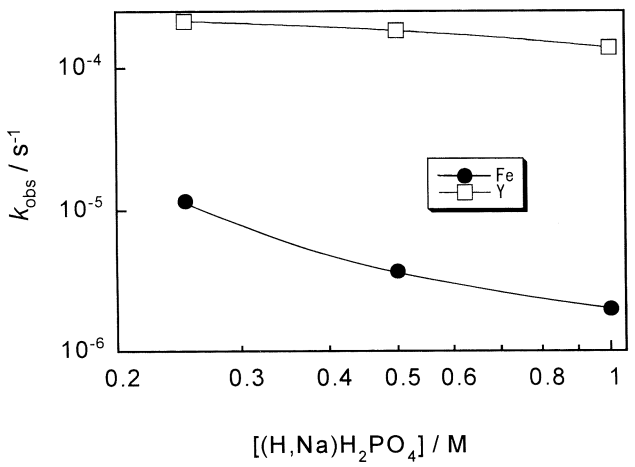

Fig.4. Effect of the concentration of phosphate buffer in the feed solution on k_{obs}. The other conditions are the same as those in Fig.2.

The separation factor in liquid membrane transport at time, α_T, can be expressed by the ratio of the $k_{obs,1}$ and $k_{obs,2}$ values for desired metals, M_1 and M_2, respectively,

$$\alpha_T = k_{obs,2} / k_{obs,1} \qquad (2)$$

The separation factor for yttrium(III) over iron(III) rises with increasing concentration of phosphate buffer, and reached to 70 in the presence of 1 M (H,Na)H_2PO_4.

Transport experiment was carried out to examine extraction conditions by varying pH at constant

0.5 M (H,Na)H_2PO_4 in the feed solution. Figure 5 shows plots of k_{obs} against pH in the feed solution. The values for yttrium(III) remain practically constant irrespective of pH, while those for iron(III) increase with increase in pH. The separation factors are reduced from above 10^3 around pH 1.5 to 20 around pH 2.5.

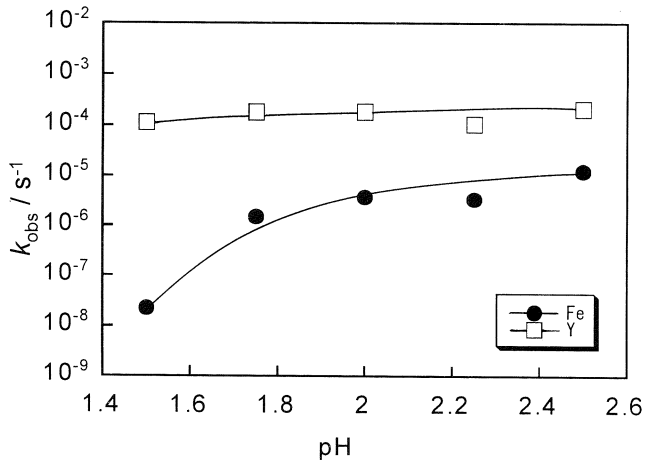

Fig.5. Effect of pH of the feed solution on k_{obs}. The other conditions are the same as those in Fig.2.

3.3 Effect of EDTA in the feed solution

Transport of iron(III) species across the membrane would be probably depressed in the presence of a complexing agent, ethylenediamine-N,N,N',N'- tetraacetic acid (EDTA). The metal transport was performed in the presence of 5 x 10^{-4} M EDTA. As Fig.6 shows, the transport of yttrium is similar to that in the absence of EDTA, while almost no transport of iron(III) was observed due to the complex formation of iron(III) with EDTA.

The values of k_{obs} for both yttrium(III) and iron(III) are illustrated as a function of pH in Fig.7. The k_{obs} value for yttrium(III) slightly decreases with increasing pH, while that for iron(III) remains very low level of 10^{-7}, in which transport of iron(III) is negligibly small. The α_T values exceed 10^3 at pH 1-

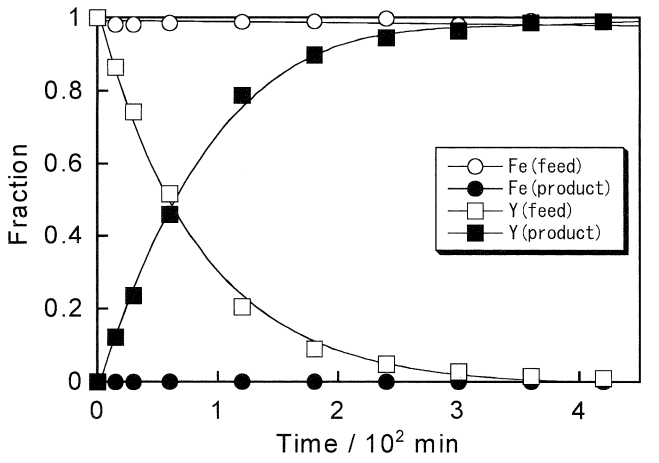

Fig.6. Transport of Y(III) and Fe(III) through SLM. SLM : 0.02 M $(DEHPA)_2$ in kerosene. Feed : 0.5 M (H,Na)Cl_2CHCOO, pH 1.5, 5 x 10^{-4} M EDTA ; product : 1 M H_2SO_4.

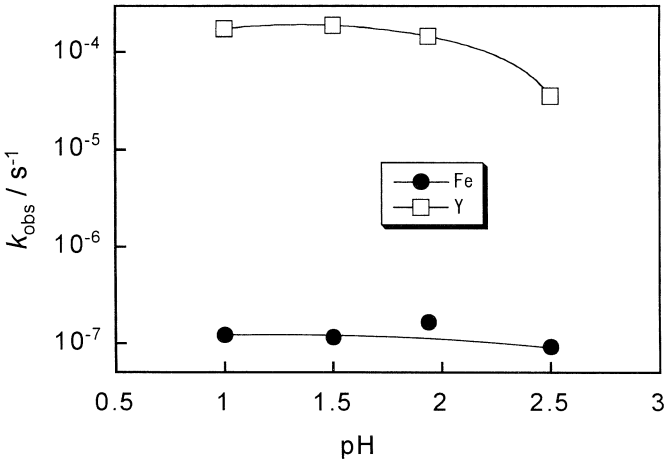

Fig.7. Effect of EDTA concentration on k_{obs}. The other conditions are the same as those in Fig. 6.

1.5, and decrease with rising pH above 1.5. The transport of iron(III) was thoroughly suppressed with EDTA, and quantitative separation of yttrium was accomplished. The separation of yettrium from iron(III) was thus enhanced by controlling pH in the presence of complexing agents.

Acknowledgement

The authors thank the staff of Laboratory of Nuclear Science, Tohoku University for its technical corporation in the preparation of the radioisotope ^{88}Y.

References

[1] D. F. Peppard, G. W. Mason, J. L. Maier and W. J. Driscoll : J. Inorg. Nucl. Chem. **4** (1957) 334.

[2] K. Akiba, K. Yamada and N. Nakamura : J. Chem. Soc. Japan (1993) 555.

[3] K. Akiba and H. Hashimoto : Solvent Extr. Res. Develop. **1** (1994) 137.

[4] K. Akiba, M. Ito and S. Nakamura : J. Membrane Sci. **129** (1997) 9.

[5] A. Tsuyoshi, H. Ito, H. Hoshi, K. Akiba and S. Nakamura : J. Radioanal. Nucl. Chem. **242** (1999) 56.

Formation of New Materials in Fullerenes by Using Nuclear Recoil

T. Ohtsuki[1], K. Ohno[2], K. Shiga[3], Y. Kawazoe[3], Y. Maruyama[4], K. Shikano[5] and K. Masumoto[6]

[1]*Laboratory of Nuclear Science, Tohoku University, Mikamine, Taihaku, Sendai 982-0826*
[2]*Department of Physics, Faculty of Engineering Yokohama National University, Tokiwadai, Hodogaya, Yokohama, 240-8501*
[3]*Institute for Materials Research, Tohoku University, Katahira, Aoba-ku, Sendai 980-8577*
[4]*National Industrial Research Institute of Nagoya (NIRIN), 1-1 Hirate-cho, Kita-ku, Nagoya 462-8510*
[5]*NTT Opto-Electronics Laboratories, Tokai, Ibaraki, 319-11*
[6]*Radiation Science Center, KEK, Tanashi, Tokyo 188-8501*

The formation of Sb or Te atom-incorporated fullerenes has been investigated by using radionuclides produced by nuclear reactions. From the trace of radioactivities of ^{120}Sb (^{122}Sb) or ^{121}Te after High Pressure Liquid Chromatography (HPLC), it was found that the formation of endohedral fullerenes or heterofullerenes in atoms of Sb or Te is possible by a recoil process following the nuclear reactions. To confirm the produced materials, *ab initio* molecular-dynamics simulations based on an all-electron mixed-basis approach was carried out. We present possibility of the formation of endohedral fullerenes or substitutional heterofullerenes incorporated with Sb or Te atoms.

§ 1. Introduction

Chemical interaction between C_{60} and a variety of atoms is becoming a very new field of cluster research. So far, numerous experimental studies for endohedrally doped [1-10] or exohedrally doped [11-13] fullerenes with foreigh atoms have been undertaken by resorting to are-desorption or laser-vaporization techniques. On the other hand, it has become possible to synthesize the heterofullerenes, where the foreign atom is incorporated into the carbon cage. Experimentally, heterofullerenes deped with foreign atoms, such as boron(B) [14,15], nitrogen(N) [16,17], silicon(Si) [22,23] have been reported. In our previous studies, we have studied not only the endohedral doping of Kr and Xe [26] but also the substitutinal doping of ^{11}C [18,19], ^{13}N [20], ^{69}Ge and ^{72}As [21] by a recoil-implantation process following nuclear reactions. In spite of the intense research, only partial facts for the formation process and the produced materials have been unveiled on the nature of the chemical interaction between a foreign atom and a fullerene cage. Therefore, it is very important and intriguing to synthesize new plastic materials, such as several atom-incorporated fullerenes, and their properties should be investigated for getting in quantities and opening up a new application in the future.

In this paper, we show evidence of Sb (or Te) atom-incorporated fullerenes on the collision between a C_{60} cage and an Sb (Te) atom, which was generated from a recoil process following nuclear reactions. We performed *ab initio* molecular-dynamics (MD) simulations: whether the Sb (Te) atom can be incorporated in the fullerene with the endohedral doping; Sb@C_{60} (Te@C_{60}), or the substitutional

doping ; SbC_{59} (TeC_{59}). Fuerthermore, the doping process of the Sb (Te) atom in a fullerene is compared with that of an As atom or a noble-gas atom.

§ 2. Experimental Procedure

According to the source nuclide used, high-energy bremsstrahlung or charged particle irradiation was used. In Table I, nuclide produced, characteristic γ-ray, half-life and reaction are listed for each material used here. About 10 mg of C_{60} fullerene powder was mixed homogeneously with 10 mg of Sb_2O_3, and used to the target material. (1) For production of ^{120}Sb(^{122}Sb)-doping fullerene, the samples were irradiated with bremsstrahlung of E_{max} = 50 MeV which originated from the bombardment of a Pt plate of 2 mm in thickness with an electron beam which was provided by a 300 MeV electron linac, Laboratory of Nuclear Science, Tohoku University. Two radioisotopes of ^{120}Sb and ^{122}Sb can be produced by photonuclear reaction, (γ, n) reactions, by an irradiation on a natural Sb. Irradiation time was set to about 8 hour and the average beam current was typically 120 μA. The sample was cooled with water bath during the irradiation. (2) For production of ^{121}Te-doping fullerene, deuteron irradiation with beam energy of 16 MeV was performed at the Cyclotron Radio-Isotope Center (CYRIC), Tohoku University. Radioisotopes of ^{121}Te can be produced by (d, 2n) reaction by an irradiation on a natural Sb. The beam current was typically 5 μA and the irradiation time was about 1 hour. The sample was cooled with He-gas during irradiation.

After the irradiation, the samples were left for one day to cool down the several kinds of short-lived radioactivities of byproducts. After the one-day cooling, radioactivities, such as ^{11}C or ^{13}N (*e.g.*, ^{11}C decays to ^{11}B with $T_{1/2}$ = 20 min), the radioactivities of ^{120}Sb (^{122}Sb) or ^{121}Te could be measured with its characteristic γ-rays (see Table I).

The fullerene samples were dissolved in *o*-dichlorobenzene after being filtrated to remove insoluble materials through a membrane filter (pore size = 0.45 μm). The soluble fraction was injected into a high-pressure liquid chromatograph (HPLC) equipped with a 5PBB (silica-bonded with the pentabromobenzyl group) column of 10 mm (inner diameter)× 250 mm (length), at a flow rate of 3 ml/min. The eluted solution was passed through a UV detector, the wavelength of which was adjusted to 290 nm in order to measure the amount of fullerenes and their derivatives.

The fraction was collected at 30 sec intervals, and the γ-ray activities of each fraction were measured with a Ge-detector coupled to the 4096-channel pulse-height analyzer whose conversion gain was set to 0.5 keV per channel. Therefore, the existence of ^{120}Sb (^{122}Sb) or ^{121}Te could be confirmed by

Table 1. Nuclear data and experimental condition for the radioactive fullerenes

Nuclide produced	γ-ray*	Half-life	Reaction	Material** and abundance (%)
^{120}Sb	197 keV	5.76 d	^{121}Sb(γ, n)^{120}Sb	^{121}Sb, 57.4
^{122}Sb	564 keV	2.70 d	^{123}Sb(γ, n)^{122}Sb	^{123}Sb, 42.6
^{121}Te	573 keV	16.80 d	^{121}Sb(d, 2n) ^{121}Te	^{121}Sb, 57.4

* : γ-ray used for the analysis [27].
** : Irradiated material as a target (both for the case of Sb and Te) : Sb_2O_3.

their characteristic γ -rays [27].

§ 3. Results and Discussion

Figure 1 shows three elution curves of the C_{60} sample irradiated by bremsstrahlung of E_{max} = 50 MeV, open circles for ^{120}Sb and solid circles for ^{122}Sb radioactivities, respectively, and by a UV detector (solid line). The horizontal axis indicates the retention time after injection into the HPLC and the vertical one the counting rate of the ^{120}Sb or ^{122}Sb radioactivities.

A strong absorption peak was observed at the retention time of 6.5 - 7 min in the elution curve (solid line) which was measured by the UV detector. This peak position corresponds to the retention time of C_{60} which was confirmed by the calibration run using the C_{60} sample before the irradiation. Following the first peak, two peaks at around 9 - 9.5 min and 13 - 16 min were consecutively observed in the UV chromatogram. For characterization of the components, the fraction corresponding to the second peak in the sample of C_{60} irradiated was collected and examined with MALDI TOF (matrix-assisted laser-desorption ionization time-of-flight) masss pectrometry in a separate run. The mass spectrum of the fraction exhibited a series of peaks at m/z $1440-24n$ (n = 1-4) corresponding to the molecular ion peak of C_{120}-nC_2 in addition to the peak for C_{60} as a base peak [24]. This fact indicates that the second and smaller third peaks can be assigned to C_{60} dimers and C_{60} trimers, respectively. These materials can be produced by the interaction between C_{60}'s in coalescence reactions after ionization by incident γ -rays or produced charged particles [26,28].

Three peaks appeared in the curve of the radioactivities ^{120}Sb (^{122}Sb) in the radiochromatogram. Aside from a slight delay, the first peak (7 min) corresponds to the C_{60} UV absorption peak. The second as well as the relatively broad third peaks were observed at the retention time of 9 - 11 min, and of 14 - 20 min, respectively. Though there is a delay in the elution peaks of the radioactivities against that of

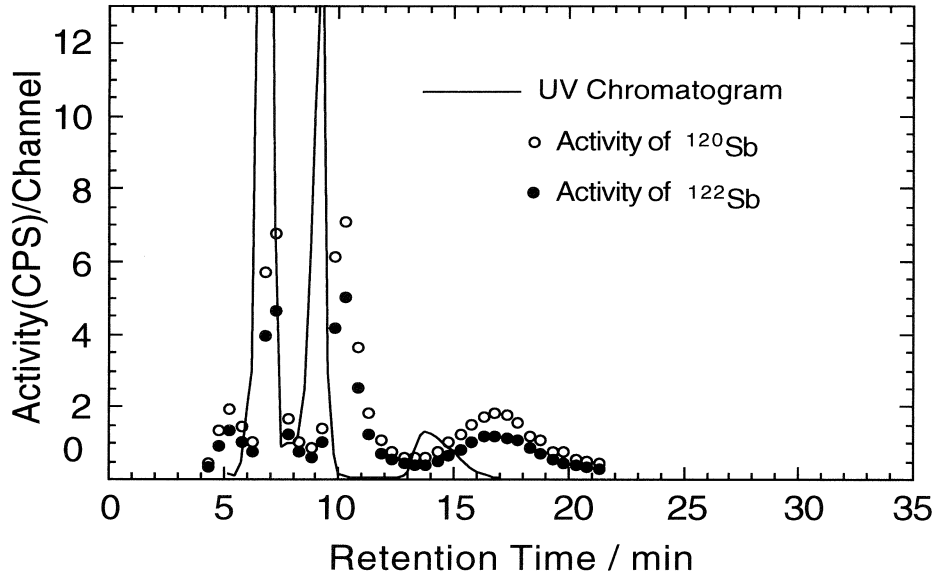

Fig.1. HPLC elution curves of the soluble portion of the crude extracted in the γ -ray-irradiated sample of C_{60} mixed with Sb_2O_3. The horizontal axis indicates retention time, and the vertical axis represents the counting rate of the radioactivities of ^{120}Sb or ^{122}Sb measured with a Ge-detector.

the UV absorption peaks, it seems that the elution behavior is similar. This result indicates that the radioactive fullerene monomers and their polymers (dimers and tetramers) labeled with ^{120}Sb (^{122}Sb) possibly exist in the final fractions. In our previous study, a similar trend was also observed in the elution curve of Kr or Xe case [26]. The amount of the Sb-incorporated radioactive fullerenes produced here is estimated to be about $10^{10}\sim10^{11}$ molecules.

The elution curves shown by solid line and solid circles in Fig.2 indicate the absorbance monitored continuously by a UV detector and γ-counting rate of ^{121}Te measured by a Ge-detector, respectively. The horizontal and the vertical axes are also same as Fig.1. From the mass measurements, three components in the UV chromatogram can be also attributed to C_{60} monomers, their dimers and trimers, respectively. Three populations of ^{121}Te are appeared at retention times of 7 min, 10 min and 14 - 18 min in Fig.2. The amount of the radioactive fullerenes seems to be the same order of magnitude of that of the Sb case.

Here, it should be noted that no evidence of exohedral molecules with a covalent nature has been presented so far by an extraction in the soluble portion. Such molecules can be removed out during the solvation process if they are exohedral. Therefore, two possibilities should be considered in the present results; (1) endohedrally Sb (Te) atom-doped fullerenes, Sb@C_{60} (Te@C_{60}), (2) substitutionally Sb (Te) atom-doped heterofullerenes as a part of the cage, SbC_{59} (TeC_{59}).

In order to understand the present experimental results, *ab initio* molecular-dynamics simulations were carried out. The method, which is used here, is based on the all-electron mixed-basis approach [25,26,28-31] using both plane waves (PW's) and atomic orbitals (AO's) as a basis set within the framework of the local density approximation (LDA). In the present study, all the core atomic orbitals are determined numerically by a standard atomic calculation based on Herman-Skillman's framework with logarithmic radial meshes [25]. For the present system, we use 313 numerical AO's and 4,169

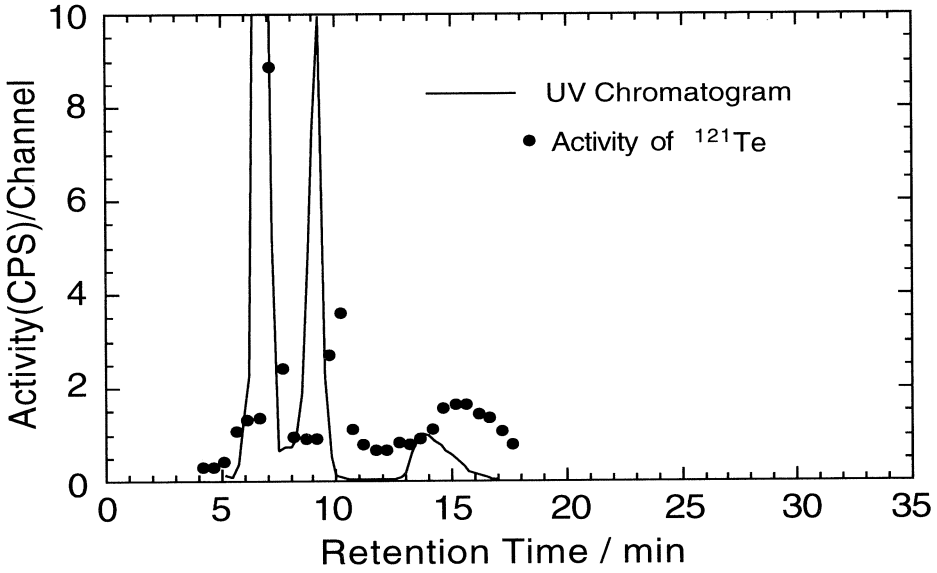

Fig.2. HPLC elution curves of the soluble portion of the crude extracted in the deuteron-irradiated sample of C_{60} mixed with Sb_2O_3. The horizontal axis indicates retention time, and the vertical axis represents the counting rate of the radioactivities of ^{121}Te measured with a Ge-detector.

PW's corresponding to a 7 Ry cutoff energy. For dynamics, we assume the adiabatic approximation where the electronic structure is always in the ground state. We utilize a supercell composed of 64×64 ×64 meshes, where one mesh corresponds to 0.196 Å. We set the basic time step as Δt = 0.1 fs and perform five steepest descent (SD) iterations after each updation of atomic positions. We do not impose any velocity control, so that the system is almost microcanonical with a little energy dissipation from the SD algorithm.

We performed the following three types of simulations for As or Te case; (A) insertion between one Sb atom and one C atom in C_{60} cage, and (B) structural stability of SbC_{59}. (C) insertion of Te atom through a six-membered ring of C_{60} (u-C_6).

Here, we describe the results of the present simulations. (A) First, we shift one of the C atoms of C_{60} outward by 1.3 Å and put additionally one Sb atom on the same radial axis by 1.3 Å inward from the original C position (see Fig.3). Then, starting the simulation with zero initial velocity, we found that there is a force acting on the Sb atom to move innerward to encapsulate (~135 fs). On the other hand, the C atom of C_{60} placed outward by 1.3 Å induced a force acting to move innerward as if it would create one of the membering u-C_6, and finally u-C_6 recovered its original configuration of C_{60}. This results may indicate the formation of $Sb@C_{60}$. (B) Second, one Sb atom was put at 1.3 Å outward from

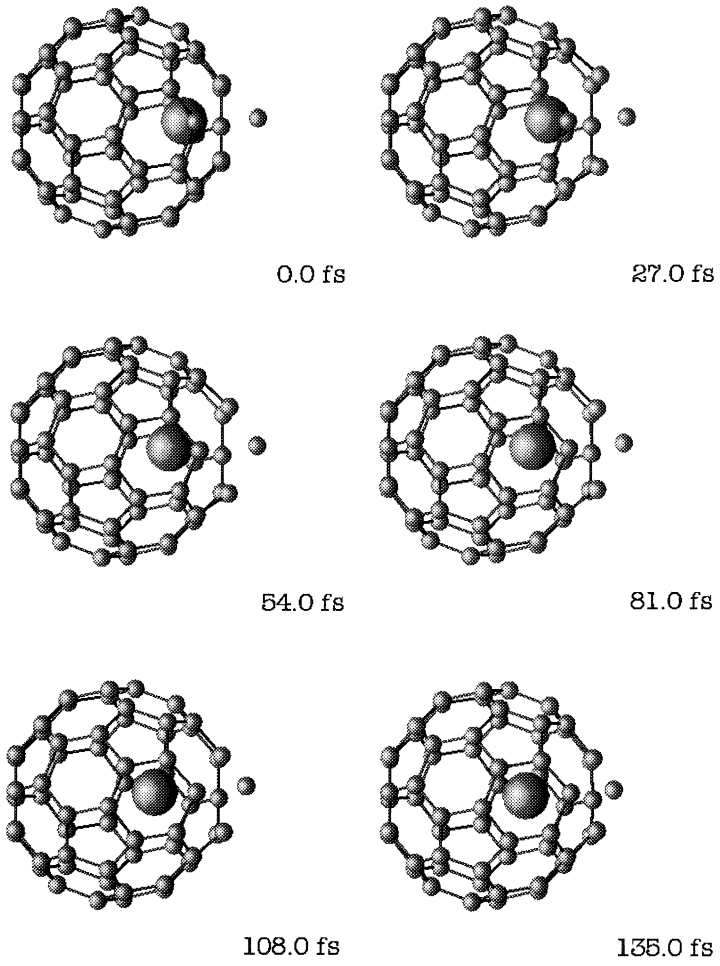

Fig.3. Simulation of the structural stability of $Sb@C_{60}$ or SbC_{59} : Change from an unstable innerside (Sb atom) and outer side (C atom) with an initial kinetic energy of 0 eV to a final stabilized configuration.

the cage sphere, instead of one C atom of u-C_6. Then, starting the simulation with zero initial velocity, we found that there is a slight moving force acting on the Sb atom against the cage, but still staying near by the initial position even after full relaxation (t = 500 fs) with some rotational inertia in the system of SbC_{59}. Therefore, it seems that the Sb atom, when put outside the cage, can be stable to create a heterofullerene such as SbC_{59}. (C) Third, in the case of Te, Te atom with the initial kinetic energy (K.E.) of 40 eV can penetrate into the cage of C_{60} through the center of u-C_6 without difficulty, Figure 4 shows several snapshots (~150 fs) of the Te atom insertion with 40 eV (K.E.). In the figure, after the Te atom first touches u-C_6, carbon atoms are pushed to open u-C_6 and goes through. But the u-C_6 recovers soon its initial configuration. Finally the Te atom bounced at the other side and come back towards the center of the cage. The result of simulations changes, of course, according to the impact energy, impact point and angle. For relatively low initial K.E., C_{60} shows a tendency to recover its original shape within the simulation period. For higher initial kinetic energies six C_2 losses occur simultaneously from the upper side of C_{60}. If an atom is inserted toward off-center positions of a six-or five-membered ring, the damage suffered on C_{60} increases significantly.

It is interesting to note that the nature of the doping process of the Sb atom in the C_{60} cage can be compared with that of As atom, because the As and Sb atoms are the same 5B group element. In our

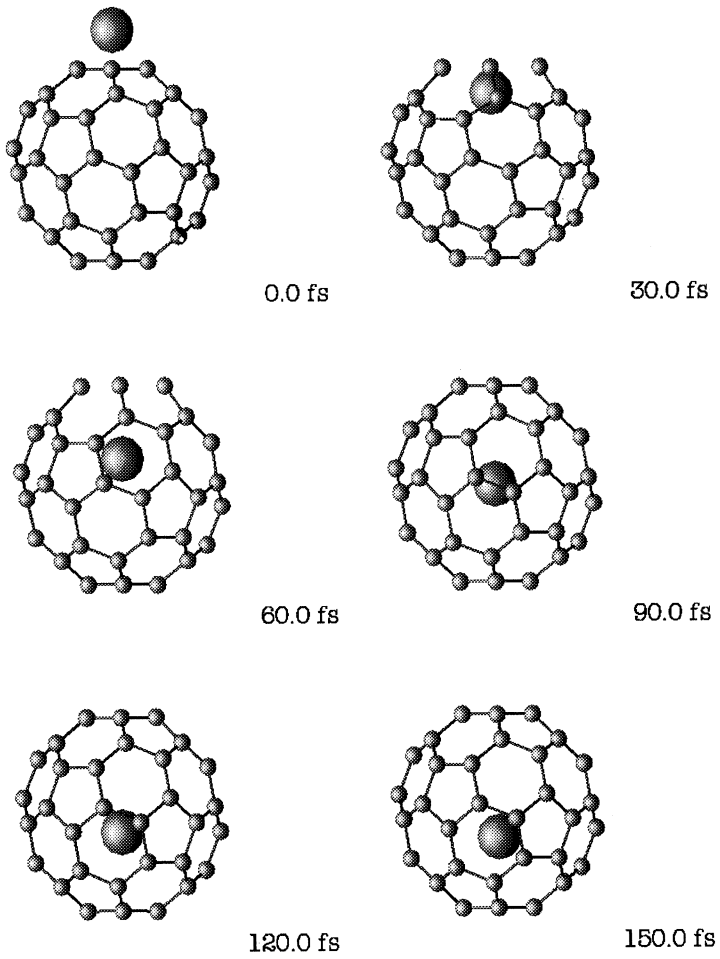

Fig.4. Simulation of Te hitting the center of a six-membered ring of C_{60} with a kinetic energy of 40 eV. Here, local skeleton disappears from the figure when the bond-length is elongated more than by 1.5Å.

previous study, we also performed similar simulations in the case of As atom [21]. From the simulations, the As atom put inside the cage is quite unstable and has a strong tendency to repel the closest C atom of C_{60} and, stabilized slightly outside the cage sphere, to create AsC_{59} (even if the As atom is put outside the cage). Therefore, we confirmed that a heterofullerene, such as AsC_{59}, may exist stably under realistic conditions. In the present results, however, it seems that the formation of $Sb@C_{60}$ is rather more likely than the formation of SbC_{59} for the interaction between the Sb atom and the C_{60} cage. But it may still remain the local stable point around the cage sphere to create a heterofullerene (SbC_{59}). In the case of Te, we found that the insertion of the Te atom through *u*-C_6 seems to be rather easier than that in the case of a noble-gas atom [26] : the Te atom can penetrate the *u*-C_6 in the K.E. of 40 eV, which is relatively lower K.E. than the case of Kr or Xe (Kr ; 80 - 150 eV, or Xe ; 130 - 200 eV). The difference can be due mainly to the magnitude of the covalent bonding between the C atom and the Sb (or As, Te) atom; it seems that the magnitude of the covalent bonding in the case Sb (Te) is weaker than that in the case of As.

In our previous study, several fourth~fifth-cycle elements in periodic table have been investigated by a recoil implantation following nuclear reactions. Schematic view of a periodic table is shown in Fig. 5, § indicates the elements investigated in the present/previous studies). In the figure, element, which is experimentally and/or theoretically confirmed as an atom-incorporated fullerene, can be limitted to (1) a small atom (like Li, Be), (2) a noble-gas atom (~Kr, Xe) and (3) a 4B~6B element. While other elements, like alkali, alkali-earth and transitional metals (Na, Ca, Sc, etc.), may destroy most of the fullerene cage in the same process, due to strong chemical reactivity between atoms and fullerenes. It is interesting to note that the group elements such as 4B~6B, even in fifth-cycle elements (like Sb or Te), can be possible for a formation of endohedrally doping fullerene or a substitutionally doping heterofullerene.

The results of analyses of the present work have to be further supported by some other experimental data such as direct mass measurements by a Time-of-Flight Mass Spectrometry (TOFMAS). Finally, we briefly comment on the experimental works now in progress.

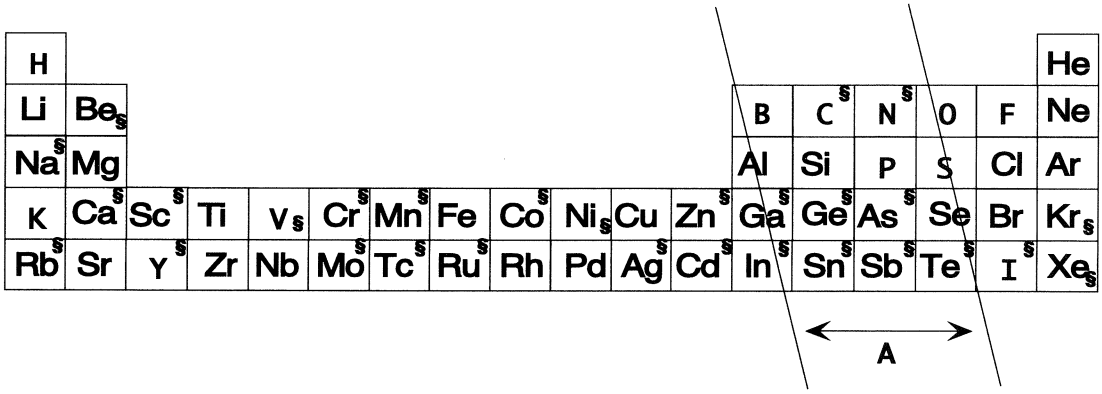

Fig.5. Schematic view of periodic table. In the figure, section (§) indicates the elements investigated in the present and/or previous experiments. "A" denotes the region of atom-incorporated fullerene investigated in 4B~6B elements.

§ 4. Conclusion

In this study, the formation of atom-incorporated fullerenes has been investigated by the traces of radioactivity of ^{120}Sb (or ^{122}Sb, ^{121}Te) produced by nuclear reactions. It was found that 5B～6B elements, like Sb or Te, remained in the final C_{60} portion after a HPLC process. This fact suggests that the formation of endohedral fullerenes, Sb@C_{60} (Te@C_{60}) and their polymers, (or substituted heterofullerenes, SbC_{59} and their polymers), can be possible by a recoil process following nuclear reactions. Carrying out *ab-initio* molecular-dynamics (MD) simulations on the basis of the all-electron mixed basis approach, we confirmed that endohedral fullerenes of Sb (Te) atoms inside the C_{60} cage can be possible. From the difference between the case of Sb (Te) and the case of As, the chemical nature of a doping atom seems to play an important role in the process of endohedrally doping or substitutionally doping in fullerenes.

Acknowledgments

The authors are grateful to the staff of the Laboratory of Nuclear Science (LNS) for handling the beam, and are grateful to the technical staff, working at IMR, Tohoku University, for their continuous support, for the supercomputing facilities of HITAC S3800. This work was supported by the Grants-in-Aid for Co-operative Research No. 12640532 from the Ministry of Education, Science and Culture of Japan.

References

[1] Y. Chai *et al.*: Phys. Chem. **95** (1991) 7564.
[2] R.D. Johnson *et al.*: Nature (London) **355** (1992) 239.
[3] J.H. Weaver *et al.*: Chem. Phys. Lett. **190** (1992) 460.
[4] H. Shinohara *et al.*: Nature (London) **357** (1992) 52.
[5] M. Takata *et al.*: Nature (London) **377** (1995) 46.
[6] W. Sato *et al.*: Phys. Rev. Lett. **80** (1998) 133.
[7] M. Saunders *et al.*: Science **271** (1996) 1693.
[8] T. Braun and H. Rausch: Chem. Phys. Lett. **288** (1998) 179.
[9] T. Braun and H. Rausch: Chem. Phys. Lett. **237** (1995) 443.
[10] G.E. Gadd *et al.*: J. Am. Chem. Soc. **120** (1998) 10322.
[11] L.M. Roth *et al.*: J. Am. Chem. Soc. **113** (1991) 6298.
[12] Y. Huang and B.S. Freiser: J. Am. Chem. Soc. **113** (1991) 9418.
[13] S.W. McElvany *et al.*: J. Phys. Chem. **96** (1992) 4935.
[14] T. Guo *et al.*: J. Phys. Chem. **95** (1991) 4948.
[15] H.J. Muhr *et al.*: Chem. Phys. Lett. **249** (1996) 399.
[16] T. Pradeep *et al.*: J. Phys. Chem. **95** (1991) 10564.
[17] J.F. Christian *et al.*: J. Phys. Chem. **96** (1992) 10597.
[18] T. Ohtsuki *et al.*: J. Am. Chem. Soc. **117** (1995) 12869.
[19] T. Ohtsuki *et al.*: Material Sci. Eng. **217/218** (1996) 38.

[20] T. Ohtsuki *et al.*: J. Radioanal. Nucl. Chem. **239** (1999) 365.

[21] T. Ohtsuki *et al.*: Phys. Rev. **B60** (1999) 1531.

[22] M. Pellarin *et al.*: Chem. Phys. Lett. **277** (1997) 96.

[23] C. Ray *et al.*: Phys. Rev. Lett. **80** (1998) 5365.

[24] T. Ohtsuki *et al.*: Chem. Phys. Lett. **300** (1999) 661.

[25] K. Ohno *et al.*: Phys. Rev. **B56** (1997) 1009.

[26] T. Ohtsuki *et al.*: Phys. Rev. Lett. **81** (1998) 967.

[27] R.B. Firestone *et al.*: Eds. Table of Isotopes, 8th Ed. Vol.I. John Wiley & Sons, Inc. 1996.

[28] T. Ohtsuki *et al.*: J. Chem. Phys. **112** (2000) 2834.

[29] T. Ohtsuki *et al.*: Phys. Rev. Lett. **77** (1996) 3522.

[30] K. Ohno *et al.*: Phys. Rev. Lett. **76** (1996) 3590.

[31] K. Shiga *et al.*: Modelling Simul. Mater. Sci. Eng. **7** (1999) 621.

Ⅲ. Accelerator and Synchrotron Radiation

凹面鏡からの後方遷移放射

柴田行男[1]，佐々木理志[1]，伊師君弘[1]，蔦谷　勉[1]，大坂俊明[2]
近藤秦洋[2]，日出富士雄[3]，松山正佳[3]，小山田正幸[3]

[1]東北大学科学計測研究所（980-8577　仙台市青葉区片平2-1-1）
[2]東北大学大学院工学研究科（980-8579　仙台市青葉区荒巻字青葉）
[3]東北大学原子核理学研究施設（982-0826　仙台市太白区三神峰1-2-1）

Backward Transition Radiation from a Concave Mirror

Y. Shibata[1], S. Sasaki[1], K. Ishi[1], T. Tsutaya[1], T. Ohsaka[1], Y. Kondo[2],
F. Hinide[3], M. Matsuyama[3] and M. Oyamada[3]

[1]*Research Institute for Scientific Measurements, Tohoku University,*
Katahira 2-1-1, Aoba-ku, Sendai 980-8577
[2]*Faculty of Engineering, Graduate School of Engineering, Tohoku University,*
Aramaki aza-aoba, Aoba-ku, Sendai, 980-8579
[3]*Laboratory of Nuclear Science, Tohoku University,*
Mikamine 1-2-1, Taihaku-ku, Sendai 982-0826

Coherent backward transition radiation (BTR), emitted from bunched electrons passing through a concave mirror, was observed in the far-infrared region. The BTR from the mirror showed more concentration into the direction of the specular reflection than BTR from a flat mirror. The concentration was prominent toward decrease of the wavelength.

§1．序　論

電子ライナックの短バンチな電子ビームからの放射は，遠赤外・ミリ波域では，個々の電子からの放射の位相がそろったコヒーレントな放射である[1-3]。コヒーレントな放射のスペクトルはバンチの電子分布と相関しているため，コヒーレントな放射の解析からバンチの縦（進行）方向電子分布を求めることが出来る[4,5]。そのようなビーム診断にしばしば利用されるのは，電子ビームが金属箔を通過する際に発せられる遷移放射である。

電子ビームが金属箔を通過するとき，軌道に沿って電子の進行方向に前方遷移放射が放射され，金属箔の鏡面反射方向に後方遷移放射が放射される。前方・後方両遷移放射ともにバンチ診断に利用されている。高エネルギーな電子の場合，前方遷移放射は，境界面の凹凸には極めて鈍感で，境界面の局所的な平面構造によらず，電子軌道に沿った方向に集中して放射される。それに対し，後方遷移放射は境界面の平坦さや凹凸に敏感であると考えられている。高エネルギーな電子ビームが周囲の物質との相互作用で光を発生する場合，類推として，電子を仮想光子と想定しその平面波が入射し物質により反射・透過・回折されるとして発生する光の様子を考察することが出来る場合がある。そのように考えた場合，球面鏡からの後方遷移放射は鏡の焦点距離の位置に集光されると予想される。

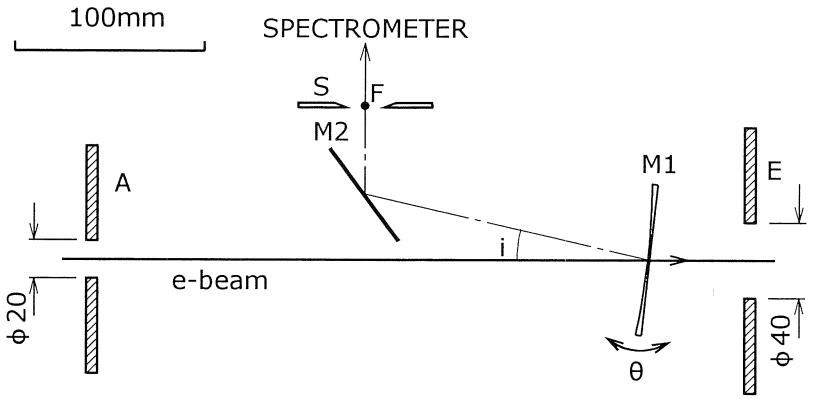

第1図　実験配置図。M1：球面鏡，M2：平面鏡，S：スリット，A：開口衝立，E：エコソーブ。平面鏡からの後方遷移放射を測定する場合は球面鏡M1を平面鏡に交換する。

そこで，電子ビームが凹面球面鏡を通過する場合の後方遷移放射の角分布測定を試みた。その場合，上期類推にもかかわらず実験結果の理論との比較は容易ではない。何となれば，通常，遷移放射は真空と物質（金属）との境界が平面と仮定して定式化されているためである。それゆえ，性質の明らかな平面鏡からの後方遷移放射を比較の基準として測定し，球面鏡からの後方遷移放射の性質を調べた。このような実験は，遷移放射に関する基礎的な実験であるにもかかわらず，これまでに明らかにされていない。実験結果は未だ解析中であるが，ここでは主な実験結果を報告する。

§2．実　験

実験は核理研のSバンドライナックを用いてビーム偏向室で行った。実験配置を第1図に示す。電子ビームは合成石英の凹面球面鏡M1を通過し，遷移放射を発生する。鏡M1は焦点距離が200mm，直径80mmの円形で中心部の肉厚が1mmである。電子軌道にそって平面波が入射したときの球面鏡M2による結像点がFであり，その位置に両開きスリットSが設置されている。測定光学系は点Fを仮想光源として調整されており，受光角は70mradである。鏡M1からの後方遷移放射は平面鏡M2で回折格子型分光計に導かれ，極低温ボロメーターで検出される。電子ビームの軌道と測定用光軸は床面に水平な面をなす。球面鏡M1は鏡の中心を通る垂直軸のまわりにパルスモーター制御で回転でき，後方遷移放射の放射角分布が測定できる。

この実験系を納めた真空容器は，ライナックに直結する，より高真空な上流部とは真空的には切断されている。すなわち，鏡M1の上流約1.35mのところで厚さ15ミクロンのアルミ箔ガスケットを境に上流と下流は，別々の真空度に保たれている。下流の実験系の真空度は，典型的には10^{-6}torrであった。電子ビームがそのアルミ箔を通過する際，前方遷移放射が発せられる。その前方遷移放射が鏡M1で集光され，測定系に導かれるのを防ぐため，鏡M1の上流290mmの軌道上にアクリルとアルミ箔からなるマスクAを置いた。電子ビームはマスクAに開けられた直径20mmの円形開口を通過する。従って真空仕切り用アルミ箔からの前方遷移放射は殆どマスクAで遮蔽されるが，一部は開口を通して鏡M1で反射され測定系に入射する。また，電子ビームがマスクを通過するときや，平面鏡M2の近くを通過するときには前方回折放射が発せられ，それがやはり鏡M1により測定系に導かれる。それゆえ，測定された光は，純粋に球面鏡からの後方遷移放射だけでは無く，以上の放射の重ね合わせである。鏡M1からの前方遷移放射が下流の真空容器壁により反射され測定系に検出されるのを防ぐため，M1の下流にもエコソーブ（サブミリ・ミリ波吸収体）の衝立Eを配置した。

参照基準となる平面鏡からの後方遷移放射を測定する場合は，球面鏡を直径80mmで厚さ1mmの合成石

英平面鏡に交換した。使用した鏡はすべてアルミ蒸着鏡である。

実験に使用した電子ビームのエネルギーは 150MeV で，エネルギー幅は0.5％，マクロパルス幅は1.5 μs であった。そのマクロパルスの繰り返しは 16.7Hz, 平均ビーム電流は 0.6 μA であった。マクロパルスは約4,300個のバンチからなり，バンチ当たり電子数は 5.3×10^7である。また，ビーム径はほぼ円形で約 5mm であった。

電子ビームは種々の原因により，ビーム軌道やバンチ構造が変動し，その変動の時間スケールも多岐にわたっている。それをビーム電流計の出力のみで補正することは出来ない。そこで M1 の下流約 1m の軌道上にアルミ箔を置き，電子ビームが通過するときに発せられるコヒーレントな遷移放射を別のシリコンボロメーターで受光し，変動補正用モニターとして使用した。

§ 3．結果と考察

実験配置図 1 のスリットを 10mm にし，球面鏡 M1 を回転することにより測定した放射の角分布を第 2 図に， M1 を平面鏡に置換した場合の測定結果を第 3 図に示す。測定波長 λ は0.5, 0.85, 1.3および 2.3mm であり，角度は光軸（鏡面反射）方向が零で，鏡 M1 の時計回りの方向が正の増加方向を示す。実線が水平方向の偏光成分を表し，点線が垂直偏光成分を表す。また，スリット幅を 23mm にした場合の同様の測定結果を第 4，5 図に示す。これら 4 図の強度分布は同一スケールで描いてあり，ビーム電流の変動による測定強度の揺らぎは補正してある。

第 3 図および第 5 図に明らかなように，平面鏡からの後方遷移放射は鏡面反射方向に対してほぼ対称的で

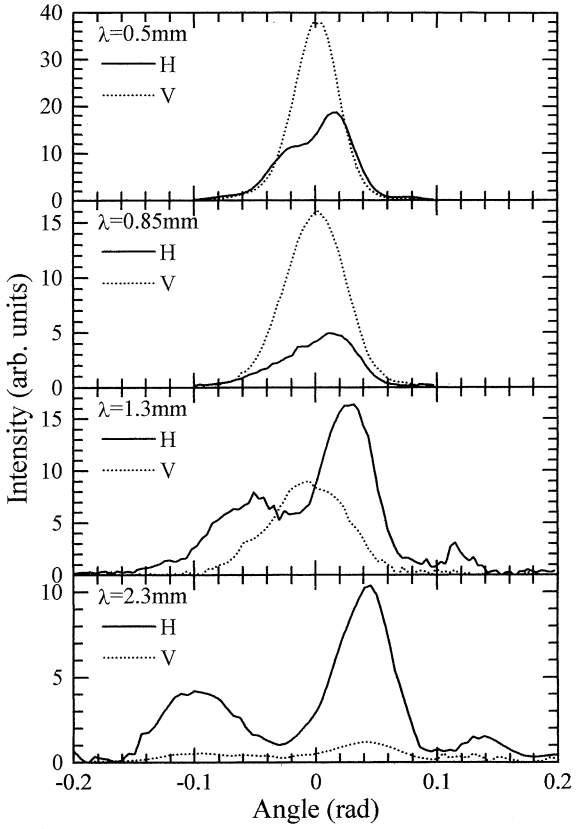

第 2 図　球面鏡からの後方遷移放射の角分布。スリット幅は 10mm。実線は水平偏光成分の分布を，点線は垂直偏光成分の結果を表す。

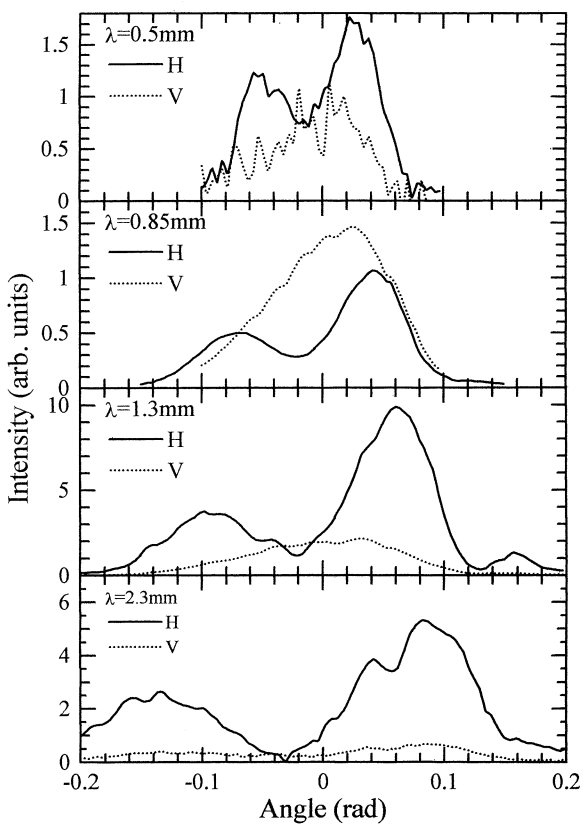

第 3 図　平面鏡からの後方遷移放射の角分布。スリット幅は 10mm。実線は水平偏光成分の分布を，点線は垂直偏光成分の結果を表す。

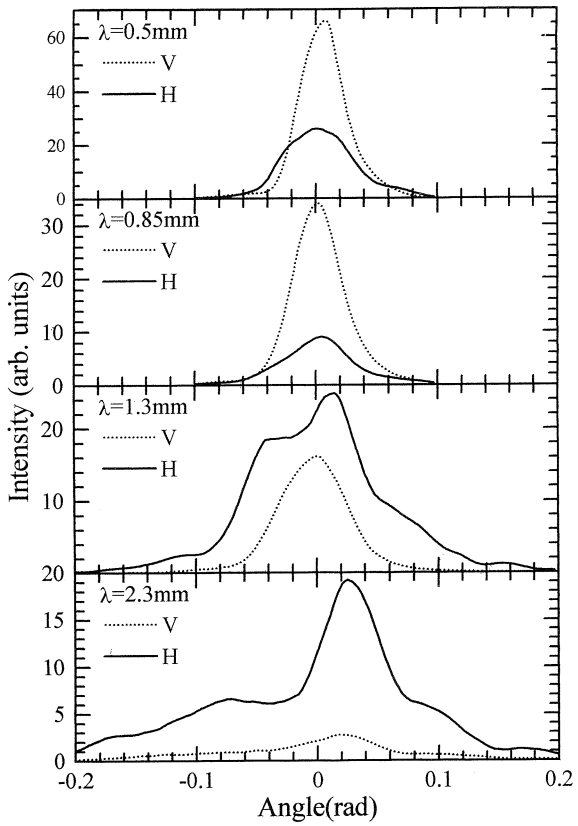

第４図　球面鏡からの後方遷移放射の角分布。スリット幅は 23mm。実線は水平偏光成分の分布を，点線は垂直偏光成分の結果を表す。

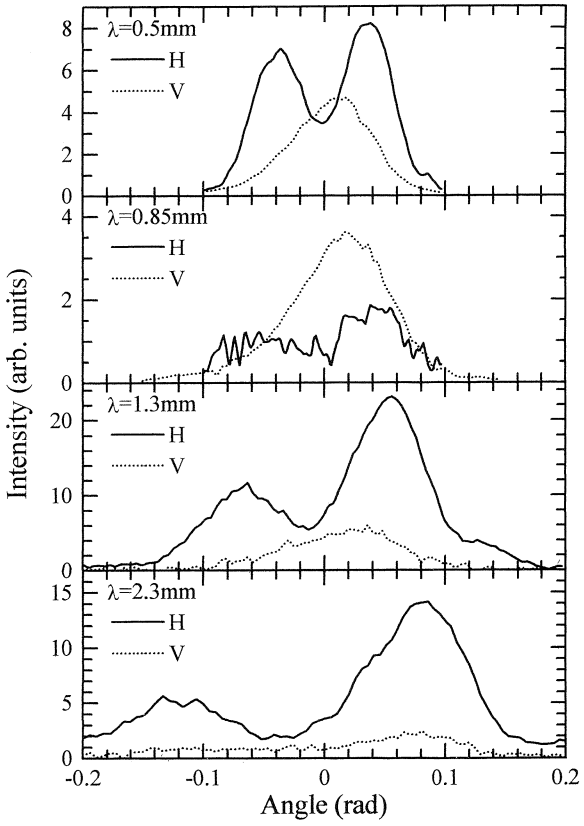

第５図　平面鏡からの後方遷移放射の角分布。スリット幅は 23mm。実線は水平偏光成分の分布を，点線は垂直偏光成分の結果を表す。

あり，水平偏光成分ではふた山のピーク構造を示しそのピーク角は長波長ほど大きくなる。垂直偏光成分では鏡面反射方向にピークのあるひと山構造を示す。また，波長 1.3mm 近辺で測定強度が最大である。

球面鏡からの後方放射は，やはりほぼ対称に分布しているが，平面鏡の場合と比較し可成り顕著な相違があり，次の特徴を示している。

1）水平・垂直両偏光成分ともその放射分布は鏡面反射方向に集中している。すなわち，水平偏光成分は波長 1.3mm および 2.3mm ではふた山構造を示すが，ピーク各および各ピークの半値幅は，平面鏡からの放射に比較し小さい。また短波長では，スリット 10mm 波長 0.5mm の場合を除き，ふた山に分離できずひと山構造のように見える。垂直偏光成分でもピークの半値幅は平面鏡の場合のそれより明らかに小さい。

2）放射強度が平面鏡の場合の強度に比較し強い。その傾向は短波長ほど顕著である。例えば，スリット 10mm の場合，球面鏡の場合の放射強度は水平・垂直両偏光成分とも平面鏡の場合の10倍以上の強度を示すが，波長 2.3mm では２倍程度である。また，測定波長範囲では球面鏡の場合は，波長が短くなるほどピーク強度も強くなっている。

一般に，波長が短い場合に比較し，波長が長いほどその波長にとって球面と平面との差は相対的に小さくなる。その効果が，短波長の測定ほど平面鏡と球面鏡との差が顕著となって現われているのであろう。

この結果は，球面鏡からの後方遷移放射の集光効果を示唆している。しかし，球面鏡の焦点に集光しているならば，水平偏光成分も中心に集中したひと山構造となるはずであるが実験結果はそうなってはいない。それゆえ，実験配置を考慮に入れた解析が必要である。この実験では後方遷移放射のみを測定しているので

はなく，上流からの放射の影響や回折放射が一緒に測定されているとして実験結果を解釈しなければならない。例えば，長波長になるほど回折の効果が大きくなるのでそれを避けて，測定波長 0.5mm，スリット幅 23mm の結果について幾何光学的に考察する。鏡 M1 の約 1.35 m上流にある真空隔絶のためのアルミ箔からは前方遷移放射が放射される。そのビーム軸にそった19mradの光は，マスクＡを通りぬけ鏡 M1 に入射する。鏡 M1 が平面鏡の場合，その入射光は測定系の方に反射され，その約88％はスリットを通過し測定系に検出される。それゆえ M1 が平面鏡の場合の結果は，近似的にはアルミ箔からの前方遷移放射と平面鏡からの後方遷移放射の重ね合わせと考えられる。また，鏡 M1 が球面鏡の場合は，上流からの入射光は球面鏡 M1で反射された後スリットＳを通過しＦ点から約 3cm 離れた所に収束し，その後発散光となって測定系に導かれる。それゆえ，この場合もアルミ箔からの前方遷移放射と球面鏡からの後方遷移放射の重ね合わせとみなせる。それゆえ，数値計算を基に解析を進めてゆく必要がある。

実験結果は，球面鏡の後方放射は平面鏡の場合とかなり顕著な相違があることを示した。この結果は，穴開き球面鏡の穴を電子ビームが通過する場合の後方回折放射も，球面鏡からの後方遷移放射と同様の効果を有することを示唆している。穴開き球面鏡を有効に利用したバンチ計測用光学系を工夫すると，光強度が強くなりS/N比が改善される可能性がある。

本研究は，東北大学理学研究科附属原子核理学研究施設のライナックを用いて行われた。実験においてはマシングループをはじめとして多数の職員から種々の支援を戴いた。ここに記して感謝する。

References

[1] T. Nakazato, M. Oyamada, N. Niimura, S. Urasawa, O. Konno, A. Kagaya, R. Kato, T. Kamiyama, Y. Torizuka, T. Nanba, Y. Kondo, Y. Shibata, K. Ishi, T. Ohsaka, and M. Ikezawa: Phys. Rev. Lett. **63** (1989) 1245.

[2] K. Ishi, Y. Shibata, T. Takahashi, H. Mishiro, T. Ohsaka, M. Ikezawa, Y. Kondo, T. Nakazato, S. Urasawa, N. Niimura, R. Kato, Y. Shibasaki, and M. Oyamada: Phys. Rev. A**43** (1991) 5597.

[3] Y. Shibata, K. Ishi, T. Takahashi, T. Kanai, F. Arai, S. Kimura, T. Ohsaka, M. Ikezawa, Y. Kondo, R. Kato, S. Urasawa, T. Nakazato, S. Niwano, M. Yoshioka, and M. Oyamada: Phys. Rev. E**49** (1994) 785.

[4] Y. Shibata, T. Takahashi, T. Kanai, K. Ishi, M. Ikezawa, J. Ohkuma, S. Okuda, and T. Okada: Phys. Rev. E**50** (1994) 1479.

[5] R. Lai and A.J. Sievers: in *Microbunches Workshop* AIP conf.proc. **367** ed. by E.B. Blum, M. Dienes, J.B. Murphy, (AIP press, New York 1996) p312.

IV. 1999 Status Report on the Accelerator

平成11年度加速器報告

小山田正幸，栗原　亮，今野　收，柴崎義信，神藤勝啓，高橋重伸
玉江忠明，七尾晶士，濱　広幸，日出富士雄，武藤正勝

東北大学原子核理学研究施設（982-0826　仙台市太白区三神峯1-2-1）

§1. はじめに

核理研研究報告には共同利用開始以来，マシン報告として電子ライナックに関した事柄が報告されてきた。昭和56年度には 150MeV ストレチャーリング（SSTR）が建設されたが，プロトタイプのユーザーマシンとして位置づけられ，原子核物理の研究者が保守・改良・運転を担ってきた。

平成７，８年度には 1.2GeV ストレッチャー・ブースタリング（STB）の建設費が認められたが，建屋の建設費や付帯設備費は含まれていなかった。そのため第２実験室内のパルス中性子源の撤去費用，ビーム輸送系を通すためのビーム偏向室を新たに建設するための費用，新しい加速器に冷却水を供給する装置の新設費，特高変電所から電気室までの高圧ケーブルの更新や電気室内の再配置の費用などは，大学施設部，理学部中央事務の特別な配慮や施設維持費のやりくりで，ようやく完成に漕ぎ着くことができた。

加速器のコミッショニングは冷却系，電気工事の完了引き渡しを受けた平成９年10月以降に開始した。ストレッチャー・ブースタリングは電子ライナックからのパルス電子線を連続電子線に変換するストレッチャーモードと電子ライナックから打ち込まれた電子を 1.2GeV まで加速するブースターモードの２つの機能を併せ持っている。この２つの機能の性能を充分高めた後，平成10年６月に科学技術庁による施設検査を受け，７月に検査合格の証書を交付された。

ストレッチャー・ブースタリングを用いた共同利用は平成10年９月からストレッチャーモードのテスト実験から開始した。約半年間の運転実績からストレッチャー・ブースタリングに関して二つの大きな問題点があることが判明した。先ず第１にリングの周辺の放射線レベルが高く，制御系やモニタ系に用いているパーソナルコンピュータ（PC）やプログラマブルコントローラ（PLC）が頻繁に停止し，加速器の運転に支障をきたすことである。次にリングから大型電子線スペクトロメータ（LDM）までのビーム輸送系の調整に多大な労力と時間を要し，加えて標的上のビームに含まれるハローが実験データのバックグラウンドの原因として無視できないレベルにあることである。これらの問題の早期解決が平成11年度の最重要課題であった。

§2. 概　況

30年以上の電子ライナック運転経験から加速器の維持・改良のための定期点検と工事の日程を次のように配置している。原則として定期点検は毎月前半，後半に各１日，そのうち１回はドアインターロックの点検を含む。１週間から10日の小規模工事期間を偶数月の上旬に定期的に設ける。８月は１ヶ月連続して運転を停止し，大規模な工事をこなすと同時に，夏季消費電力増大期に節電に協力して見返りとして電力料金の割引を受けることにしている。

平成11年度は上記課題を解決するため３月下旬から５月連休まで40日間を工事期間に設定した。主な工事はリングのビーム取り出しからスペクトロメータ(LDM)までのビーム輸送系の大改造とリング周辺に配置してあった制御系・モニタ系のPC，PLCを放射線の影響のない隣接の空調機械室への移設である。これらの対策の結果，制御系・モニタ系の停止の問題はほぼ解決し，ビーム輸送系の透過率は大幅に改善した。

ストレッチャー・ブースタリングが本格的に運転を開始したことに対して付近住民の理解を深めて貰うために一般公開を10月17日に開催した。一般人に加速器をごく近くで見て貰うためにコンクリートブロックや鉛板を用いて要所をシールドした。一般公開後，標識ガンマ線を取り出すため，リングの偏向ダクトを本来の枝付きダクトに交換した。これらの一連の工事のため10月は工事期間に当て，その代わりに例年と違って８月を共同利用に当てた。

偏向ダクト交換後ストレッチャー･ブースタリングの運転を再開したところ，従来と同じエネルギーでビームを入射したにも関わらず同じ電流（磁場）ではビームが回らず，電流を1.5%程多くまたは少なくしなければならなくなった。更にブースターモードでは加速周波数も従来より低くして軌道長を長くしなければならないことが分かった。しかもビームが回るパラメータの範囲が非常に狭くなった。なぜそうなったかの理由はなかなか分からず，共同利用のストレッチャーモードの運転やブースターモードのマシンスタディに勢力を消耗した。平成12年４月の徹底的なマシンスタディの結果，交換したダクト近傍の中心軌道近くに障害物があると確信し，５月に真空を破って調べたところ，このダクトの大気圧によるつぶれを防ぐ支柱が製作ミスから設計位置をはずれ丁度中心軌道の位置にあることが分かった。この件に関する詳報は平成12年度の加速器報告に譲る。

§3. 共同利用

第１表に平成11年度のマシンタイム加速器運転シフト数を示す。加速器不調のため後日保証したシフト数を含めてあるので，公式実施シフト数とは必ずしも一致しない。また前年度割り当てでも，加速器の故障などで実施が平成11年度に延期された分を含んでいる。日程まで含めた加速器運転状況を第２表の平成11年度前期後期マシンタイムに示す。土日および祝祭日であっても，連続実験で加速器を運転した場合は表に記載した。

第１表　平成11年度マシンタイム加速器運転シフト数

課　題　分　野	実施シフト数
原子核　ストレッチャーモード	102
RI	30
コヒーレント放射	44
その他（音響検出器開発）	5
原子核　ストレッチャーモードテスト実験	23
マシンスタディストレッチャーモード	7
マシンスタディブースターモード	19
マシンスタディ電子ライナック	2
合　計	232

§4. 保守改良

ここでは加速器の保守・改良・故障状況についてやや詳しく記述する。

○4月

・制御系，モニタ系のPC，PLCを第2空調機械室に移設

・ビーム輸送系の大改造

四極電磁石の移設と増設　TQ5,6 を上流へ，TQ8,9 を上流へ，TQ10,11 を増設

スクリーンモニタを増設　TM2 の上流，TM4 の上流，TQ10 の上流

コリメータの設置　TQ4 の下流，TM2 の上流，TM4 の上流

ステアリングコイルの移設

ビーム取り出しラインに四極電磁石を増設

・ビーム輸送系のアラインメント

・ビーム輸送系の変更にともなって制御系画面の変更

・TAGX電磁石搬入前にリング電磁石のアラインメント測量

・リング偏向電磁石（BM）の電流立ち上がり時間を1秒に短縮

テスト運転中に IGBT 破損　全数交換。IGBT 駆動方式の抜本的改良

・前年度末納入されたライナック用サイラトロンのエージング

○5月

・ストレッチャーモードでのテスト運転　ビーム輸送系のビーム透過率大幅に改善

・ライナックのクライストロンパルサー電源電圧が 190V まで低下

トランスの一次側タップを 6800V から 6600V に切り替える

・クライストロンパルサ＃3のサイラトロンを交換

・17日から31日朝までストレッチャーモード連続運転

○6月

・ライナックのクライストロンヒータ，サイラトロンヒータ・リザーバ回路に交流安定化　電源を合計10台入れる。以後ライナック運転が安定になる

・クライストロンパルサー＃4高圧側コネクタが破損したので交換

チャージングコイルタンクの油が劣化しているので交換

・リング北側に TAGX 用レール敷設

・リング偏向電磁石（BM）電源を抜本的に改造　IGBT 全数を完全独立動作に変更

・30日豪雨のため管理棟配線ピット浸水し実験中断

○7月

・リングのターボ分子ポンプの故障頻発

・11日豪雨　実験室ビームキャッチャー漏水

・TAGX 電磁石搬入据え付け

○8月
・ペアスペクトロメータ電磁石搬入
・クライストロンパルサー＃３のクライストロン冷却系熱交換機容器を交換　予備なし
・15日豪雨　ビームキャッチャー，管理棟配線ピット浸水
・リングのキッカー＃３動作不良

○9月
・１日濱赴任
・キッカー＃３のサイラトロン交換
・リングの入射ラインにスクリーンモニタ増設
・７日から19日朝までストレチャーモード連続運転
・クライストロン＃３のガスケット不良によりタンク内に水漏れ　修理

○10月
・サイラトロン＃３およびクライストロン＃３交換
・一般公開のためリング周辺シールドを増強
・17日一般公開
・リング偏向ダクト（BM4）ガンマ線取り出し窓付きのものに交換
・27日豪雨　ビームキャッチャー，管理棟配線ピット浸水，
　クライストロンパルサ＃２天井雨漏り
・クライストロン＃４交換

○11月
・リングのテスト　BM の電流従来の 181A ではビーム回らず　178A，184A では回る
・STB冷却系電動２方弁増設　既設の２方弁と合わせて３方弁的な動作になる
・16日神藤赴任
・ビームキャッチャー防水工事
・電子銃タンク冷却配管より水漏れ　応急修理

○12月
・ライナック運転用のマイクロVAXの動作不調

○１月
・KEK よりリング用クライストロンを管理換え

○２月
・22日より３月４日朝までストレッチャーモードで連続運転

○3月

・キッカー＃３のドライバのパルストランス断線　修理

・電子銃タンクの冷却管水漏れ本格的修理

§5. おわりに

ストレッチャー・ブースタリングの運転パラメータの許容範囲が11月以降非常にセンシティブになった。これは偏向電磁石のダクトを交換した時期に一致している。この原因を追及することが次年度への緊急の宿題となった。年度始めの４月にはこの問題を最重点に取り上げて解決する予定である。

加えて急がなければならないのは，ライナックの制御系の更新である。用いているコンピュータは非常に古く，いつ動かなくなっても不思議ではない。この問題は担当するチーム体制の確立から始めなければならない。

今年度は加速器担当の人の動きが目立った。平成11年の３月末で浦澤が定年退官した後，９月１日に分子研から濱が赴任し，11月16日からはKEKから神藤が赴任した。更に今野が平成12年４月１日付けで一関工業高等専門学校に赴任した。

核理研の加速器の保守・改良に対して活躍された研究支援の松田一衛氏および木須三男氏に深く感謝します。

4月	曜日	マシンタイム	5月	曜日	マシンタイム	6月	曜日	マシンタイム	7月	曜日	マシンタイム	8月	曜日	マシンタイム	9月	曜日	マシンタイム
1	木	工　事	1	土	－休日－	1	火	工　事	1	木	CR/CR	1	日	－休日－	1	水	CR/CR
2	金	工　事	2	日	－休日－	2	水	AD	2	金	CR/CR	2	月	工　事	2	木	CR/CR
3	土	－休日－	3	月	－休日－	3	木	AD	3	土	－休日－	3	火	工　事	3	金	RI
4	日	－休日－	4	火	－休日－	4	金	RI	4	日	－休日－	4	水	工　事	4	土	－休日－
5	月	工　事	5	水	－休日－	5	土	－休日－	5	月	工　事	5	木	工　事	5	日	－休日－
6	火	STB	6	木	工　事	6	日	－休日－	6	火	工　事	6	金	工　事	6	月	工　事
7	水	STB	7	金	RI	7	月	工　事	7	水	工　事	7	土	－休日－	7	火	een/een
8	木	STB	8	土	－休日－	8	火	工　事	8	木	工　事	8	日	－休日－	8	水	een/een
9	金	RI	9	日	－休日－	9	水	工　事	9	金	工　事	9	月	工　事	9	木	een/een
10	土	－休日－	10	月	停電	10	木	工　事	10	土	－休日－	10	火	工　事	10	金	een
11	日	－休日－	11	火	RI(II)	11	金	工　事	11	日	－休日－	11	水	工　事	11	土	een/een
12	月	工　事	12	水	LDM	12	土	－休日－	12	月	STB	12	木	工　事	12	日	een/een
13	火	工　事	13	木	LDM	13	日	－休日－	13	火	STB	13	金	工　事	13	月	een/een
14	水	工　事	14	金	LDM/LDM	14	月	RI	14	水	STB	14	土	－休日－	14	火	een/een
15	木	工　事	15	土	LDM	15	火	eep/eep	15	木	STB	15	日	－休日－	15	水	een/een
16	金	工　事	16	日	－休日－	16	水	eep/eep	16	金	RI	16	月	工　事	16	木	een/een
17	土	－休日－	17	月	V	17	木	V/V	17	土	－休日－	17	火	een	17	金	een/een
18	日	－休日－	18	火	V/V	18	金	150MeV	18	日	－休日－	18	水	een	18	土	een/een
19	月	工　事	19	水	eep/eep	19	土	－休日－	19	月	工　事	19	木	een/een	19	日	－休日－
20	火	工　事	20	木	eep/eep	20	日	－休日－	20	火	－休日－	20	金	een	20	月	工　事
21	水	工　事	21	金	eep/eep	21	月	CR/CR	21	水	CR/CR	21	土	－休日－	21	火	AD
22	木	工　事	22	土	eep/eep	22	火	工事/CR	22	木	CR/CR	22	日	－休日	22	水	工　事
23	金	RI	23	日	eep/eep	23	水	CR/CR	23	金	CR/CR	23	月	工　事	23	木	－休日－
24	土	－休日－	24	月	eep/eep	24	木	CR	24	土	－休日－	24	火	入射テスト	24	金	RI
25	日	－休日－	25	火	eep/eep	25	金	RI	25	日	－休日－	25	水	6色	25	土	－休日－
26	月	工　事	26	水	eep/eep	26	土	－休日－	26	月	een/een	26	木	工　事	26	日	－休日－
27	火	工　事	27	木	eep/eep	27	日	－休日－	27	火	een/een	27	金	RI	27	月	1.2GeV
28	水	工　事	28	金	eep/eep	28	月	工　事	28	水	een/een	28	土	－休日－	28	火	1.2GeV
29	木	－休日－	29	土	eep/eep	29	火	CR/CR	29	木	150MeV	29	日	－休日－	29	水	1.2GeV
30	金	工　事	30	日	eep/eep	30	水	大雨/CR	30	金	RI	30	月	RI	30	木	1.2GeV
			31	月	RI				31	土	－休日－	31	火	CR/CR			1.2GeV

マシンタイム内容　STB：ストレッチャーモードマシンテスト，1.2GeV：ブースターモードマシンテスト，6色：6色問題マシンテスト，LDM：ストレッチャーモードテスト実験　150MeV：ストレッチャーモードテスト実験　V：V系テスト実験　eep：(e,e′p) 原子核実験，een：(e,e′n) 原子核実験，eef：(e,e′fission) 原子核実験，Tag：標識ガンマ線原子核実験，RI：アイソトープ製造・照射実験，CR：コヒーレント放射実験，AD：音響検出器開発実験

10月	曜日	マシンタイム	11月	曜日	マシンタイム	12月	曜日	マシンタイム	1月	曜日	マシンタイム	2月	曜日	マシンタイム	3月	曜日	マシンタイム
1	金	1.2GeV	1	月	工　事	1	水	工　事	1	土	－休日－	1	火	定期点検	1	水	een/een
2	土	－休日－	2	火	工　事	2	木	工　事	2	日	－休日－	2	水	工　事	2	木	een/een
3	日	－休日－	3	水	－休日－	3	金	停電	3	月	－休日－	3	木	工　事	3	金	een/een
4	月	定期点検	4	木	定期点検	4	土	－休日－	4	火	定期点検	4	金	工　事	4	土	－休日－
5	火	工　事	5	金	RI	5	日	－休日－	5	水	工　事	5	土	－休日－	5	日	－休日－
6	水	工　事	6	土	－休日－	6	月	定期点検	6	木	工　事	6	日	－休日－	6	月	定期点検
7	木	工　事	7	日	－休日－	7	火	工　事	7	金	工　事	7	月	工　事	7	火	工　事
8	金	工　事	8	月	RI	8	水	CR/CR	8	土	－休日－	8	火	工　事	8	水	AD
9	土	－休日－	9	火	RI	9	木	CR/CR	9	日	－休日－	9	水	工　事	9	木	AD
10	日	－休日－	10	水	V/V	10	金	RI	10	月	－休日－	10	木	RI	10	金	工　事
11	月	－休日－	11	木	V/V	11	土	－休日－	11	火	工事/π0	11	金	－休日－	11	土	－休日－
12	火	工　事	12	金	V/V	12	日	－休日－	12	水	π0/π0	12	土	－休日－	12	日	－休日－
13	水	工　事	13	土	V/V	13	月	工　事	13	木	π0/π0	13	日	－休日－	13	月	工　事
14	木	工　事	14	日	V	14	火	1.2GeV	14	金	RI	14	月	RI	14	火	CR/CR
15	金	工　事	15	月	定期点検/eef	15	水	1.2GeV	15	土	－休日－	15	火	CR/CR	15	水	CR/CR
16	土	－休日－	16	火	eef	16	木	1.2GeV	16	日	－休日－	16	水	CR/CR	16	木	CR/CR
17	日	一般公開	17	水	eef/eef	17	金	1.2GeV	17	月	RI	17	木	CR/CR	17	金	RI
18	月	定期点検	18	木	eef/eef	18	土	－休日－	18	火	定期点検	18	金	RI	18	土	－休日－
19	火	工　事	19	金	eef/eef	19	日	－休日－	19	水	CR/CR	19	土	－休日－	19	日	－休日－
20	水	工　事	20	土	eef	20	月	RI	20	木	CR/CR	20	日	－休日－	20	月	－休日－
21	木	工　事	21	日	－休日－	21	火	定期点検/Tag	21	金	RI	21	月	定期点検	21	火	定期点検
22	金	工　事	22	月	RI	22	水	Tag/Tag	22	土	－休日－	22	火	een	22	水	1.2GeV
23	土	－休日－	23	火	－休日－	23	木	Tag/Tag	23	日	－休日－	23	水	een/een	23	木	1.2GeV
24	日	－休日－	24	水	1.2GeV	24	金	Tag/Tag	24	月	V/V	24	木	een/een	24	金	1.2GeV
25	月	工　事	25	木	1.2GeV	25	土	Tag	25	火	1.2GeV	25	金	een/een	25	土	－休日－
26	火	工　事	26	金	1.2GeV	26	日	－休日－	26	水	1.2GeV	26	土	een	26	日	－休日－
27	水	工　事	27	土	－休日－	27	月	工　事	27	木	1.2GeV	27	日	een/een	27	月	RI
28	木	工　事	28	日	－休日－	28	火	工　事	28	金	1.2GeV	28	月	een	28	火	工　事
29	金	RI	29	月	工　事	29	水	－休日－	29	土	－休日－	29	火	een	29	水	工　事
30	土	－休日－	30	火	工　事	30	木	－休日－	30	日	－休日－	30	木	工　事			1.2GeV
31	日	－休日－				31	金	－休日－	31	月	RI				31	金	工　事

マシンタイム内容　STB：ストレッチャーモードマシンテスト，1.2GeV：ブースターモードマシンテスト，6色：6色問題マシンテスト，LDM：ストレッチャーモードテスト実験　150MeV：ストレッチャーモードテスト実験　V：V系テスト実験　eep：(e,e′p) 原子核実験，een：(e,e′n) 原子核実験，eef：(e,e′fission) 原子核実験，Tag：標識ガンマ線原子核実験，RI：アイソトープ製造・照射実験，CR：コヒーレント放射実験，AD：音響検出器開発実験

V. List of Publications

List of Publications（論文リスト）(1999.1～1999.12)

Papers Published in Refereed Journals

1. Measurement of the ^{6}Li(e,e'p) Reaction Cross Sections at Low Momentum Transfer.
   T. Hotta, T. Tamae, T. Miyase, I. Nakagawa, T. Suda, M. Sugawara, T. Tadokoro, A. Takahashi, E. Tanaka, H. Tsubota
   Nucl. Phys. **A645** (1999) 492-508.
2. Anomalous Enhancement of DD Reactions in Pd and Au/Pd/PdO Heterostructure Targets under a Low Energy Deuteron Bombardment.
   H. Yuki, J. Kasagi, A.G. Lipson, T. Ohtsuki, T. Baba, T. Noda, B.F. Lyakhov and N. Asami
   JETP Letters **68** (1999) 785-790.
3. Measurement of Proton-Proton Bremsstrahlung at 389 MeV.
   K. Yasuda, H. Akimune, T. Hotta, K. Imai, M. Kato, M. Kawabata, Y. Maeda, M. Matsuoka, T. Matsuzuka, Y. Mizuno, T. Murakami, J. Murata, I. Nakagawa, N. Nomachi, T. Noro, Y. Sugaya, K. Takahisa, T. Tamae, K. Tamura, H. Tsubota, Y. Yokota, H.P. Yoshida, M. Yoshimura, and Y. Yuasa
   Phys. Rev. Lett. **82** (1999) 4775-4778.
4. Subthreshold ρ^{0} Photoproduction on ^{3}He.
   M.A. Kagarlis, Z. Papandreou, G.M. Huber, G.J. Lolos, A. Shinozuka, E.J. Brash, F. Farzanpay, M. Iurescu, A. Weinerman, G. Garino, K. Maruyama, O. Konno, K. Maeda, T. Terasawa, H. Yamazaki, T. Emura, H. Hirosawa, K. Niwa, H. Yamashita, S. Endo, K. Miyamoto, Y. Sumi, A. Leone, R. Perrino, T. Maki, A. Sasaki, and J.C. Kim
   Phys. Rev. C**60** (1999) 025203.
5. Symmetric and Asymmetric Scission Properties: Identical Shape Elongations of Fissioning Nuclei.
   Y.L. Zhao, I. Nishinaka, Y. Nagame, M. Tanikawa, K. Tsukada, S. Ichikawa, K. Sueki, Y. Oura, H. Ikezoe, S. Mitsuoka, H. Kudo, T. Ohtsuki, and H. Nakahara
   Phys. Rev. Lett. **82** (1999) 3408-3411.
6. Perofrmance of n-γ Pulse-shape Discrimination with Simple Pile-up Rejection at High γ-ray Count Rates.
   T. Okuda, H. Yamazaki, M. Kawabata, J. Kasagi and H. Harada
   Nucl. Instr. and Meth. **A426** (1999) 497-502.
7. Bresstrahlung Emission in α-decay of ^{212}Po,
   T. Ohtsuki, J. Kasagi, N. Kasajima, H. Yamazaki, H. Yuki and M. Yukishima
   J. Radioanal. Nucl. Chem. **239** (1999) 123-126.
8. Separation of Yttrium (III) from Iron (III) through Liquid Membrane Impregnated with Di (2-ethylhexyl) phosphoric Acid.
   Akira Tsuyoshi, Hiromichi Ito, Harutaka Hoshi, Kenichi Akiba and Shigeto Nakamura
   J. Radioanal. Nucl. Chem. **242** (1999) 451-456.

9. Separation of Cesium and Strontium by Potassium Nickel Hexacyanoferrate (II)-Loaded Zeolite.
   A.H. Mimura, M. Kimura, K. Akiba and Y. Onodera
   J. Nucl. Sci. Technol. **36** (1999) 307-310.
10. Reinvestigation of Low-lying Levels of ^{221}Th.
   H. Yuki, K. Nakazawa, T. Ohtsuki, J. Kasagi and T. Mitsugashira
   J. Radioanal. Nucl. Chem. **239** (1999) 151-153.
11. Observation of Radioactive Hetero-fullerenes Using Radiochemical Techniques.
   T. Ohtsuki, K. Masumoto, K. Sueki, K. Shikano, T. Shigematsu
   J. Radioanal. Nucl. Chem. **239** (1999) 365-370.
12. Direct Preparation of Radioactive Carbon Labeled Fullerenes Using Nuclear Reaction.
   K. Masumoto, T. Ohtsuki, K. Sueki, K. Kikuchi, T. Mitsygashira
   J. Radioanal. Nucl. Chem. **239** (1999) 201-206.
13. Characteristics of Binary Scission Configuration in Proton Induced Fission of Actinides.
   L.Y. Zhao, T. Ohtsuki, Y. Nagame, I. Nishinaka, K. Tsukada, S. Ichikawa, H. Ikezoe,
   Y. Hatsukawa, K. Hata, M. Tanikawa, Z. Qin, K. Sueki, Y. Oura, H. Kudo, H. Nakahara
   J. Radioanal. Nucl. Chem. **239** (1999) 113-116.
14. Formation of Dimer, Trimer and Tetramer of C60 and C70 by Gamma-ray, Charged-particle Irradiation, and Their HPLC Separation.
   T. Ohtsuki, K. Masumoto, T. Tanaka, K. Komatsu
   Chem. Phys. Lett. **300** (1999) 661-666.
15. Systematisc of Bimodal Nature in Actinide Fission.
   Y. Nagame, I. Nishinaka, Y.L. Zhao, K. Tsukada, S. Ichikawa, H. Ikezoe, M. Tanikawa,
   T. Ohtsuki, Y. Oura, K. Sueki, H. Nakahara, H. Kudo, Y. Hamajima, K. Takamiya,
   K. Nakanishi, H. Baba
   J. Radioanal. Nucl. Chem. **239** (1999) 97-101.
16. Recent Results from the JAERI Recoil Mass Separator.
   S. Mitsuoka, H. Ikezoe, T. Ikuta, S. Hamada, Y. Nagame, K. Tsukada, I. Nishinaka,
   T. Ohtsuki
   J. Radioanal. Nucl. Chem. **239** (1999) 155-157.
17. Photon Activation Analysis of I, Tl, and U in Environmental Materials.
   K. Masumoto, T. Ohtsuki, Y. Miyamoto, J.H. Zaidi, A. Kajiwara, H. Haba, K. Sakamoto
   J. Radioanal. Nucl. Chem. **239** (1999) 495-500.
18. Formation of As-and Ge-doped Heterofullerenes.
   T. Ohtsuki, K. Ohno, K. Shiga, Y. Kawazoe, Y. Maruyama, K. Masumoto
   Phys. Rev. **B60** (1999) 1531-1534.
19. Production and Purification of Organic Reagents Labeled with Radioisotopes Produced by an Accelerator.
   K. Shikano, K. Masumoto, T. Ohtsuki, M. Kato
   J. Radioanal. Nucl. Chem. **241** (1999) 75-82.

20. Ab Initio Molecular Dynamics in an All-electron Mixed-basis Approach:Application to Atomic Insertions to C-60.

    K. Shiga, K. Ohno, Y. Maruyama, Y. Kawazoe, T. Ohtsuki

    Modelling Simul. Mater. Sci. Eng. **7** (1999) 621-630.

21. Direct Preparation of Radioactive Fullerenes as a Tracer for Applications.

    T. Ohtsuki, K. Masumoto, K. Shikano, K. Sueki, T. Tanaka, K. Komatsu

    Biologcal Trace Element Research. **71** (1999) 489-498.

22. 中性子散乱実験用遮蔽体の放射化量評価と解体.

    桝本和義, 大槻　勤, 笠木治郎太, 泉　雄一, 大和一朗

    保健物理 **34(2)** (1999) 151-160.

23. Transport Efficiency of JAERI Recoil Mass Separator.

    T. Kuzumaki, H. Ikezoe, S. Mitsuoka, T. Ikuta, S. Hamada, Y. Nagame, I. Nishinaka, T. Ohtsuki, O. Hashimoto

    Nucl. Instr. and Meth. **A437** (1999) 107-113.

24. A Perturbative Formulation of Nonlinear Dispersion for Particle Motion in Storage Ring.

    H. Tanaka, M. Takao, K. Soutome, H. Hama and M. Hosaka

    Nucl. Instr. and Meth. **431** (1999) 396-408.

25. Longitudinal Beam Dynamics and FEL Interaction on a Negative Momentum Compaction Storage Ring.

    H. Hama and M. Hosaka, Nulc. Instr. and Meth. **A429** (1999) 172-178.

26. Influence of Electron Beam Properties on Spontaneous Radiation from an Optical Klystron.

    M. Hosaka, H. Hama, J. Yamazaki

    Nucl. Instr. and Meth. **A429** (1999) 191-196.

27. Longitudinal Impedance Tuner Using New Material FINEMET.

    K. Koba, D. Arakawa, M. Fujieda, K. Ikegami, Y. Ishi, Y. Kanai, C. Kubota, S. Machida, Y. Mori, C. Ohmori, K. Shinto, S. Shibuya, A. Takagi, T. Toyama, T. Uesugi, T. Watanabe, M. Yamamoto, T. Yokoi and M. Yoshii

    Rev. Sci. Instrum. **70** (1999) 2988-2992.

Papers Published in Intnational Conference Proceedings

1. S_{11} Resonance in Nuclei Studied in the C (γ , η) Reaction.

    T. Yorita, H. Yamazaki, T. Kinoshita, T. Okuda, H. Matsui, T. Maruyama, J. Kasagi, T. Suda, K. Itoh, T. Miyakawa, H. Okuno, H. Shimizu, H.Y. Yoshida, and T. Kinashi

    Proc. Int. Conf. Meson and Light Nuclei '98 (World Scientific, 1999) 90-93.

2. Medium Effects: Nuclear Reactions in Solids and Nucleon Resonances in Nuclei.

    J. Kasagi

    Proc. RCNP International Symposium on Nuclear Responses and Medium Effects (Universal Academy Press Inc.), (1999) 229-236.

3. Bremsstrahlung Emission in α-decay and Tunneling Motion of α Particles.

J. Kasagi, H. Yamazaki, N. Kasajima, T. Ohtsuki and H. Yuki

Proceedings of the 3rd Japan China Joint Nuclear Physics Symposium on Recent Topics in Nuclear Physics (Tohoku Univ.), (1999) 173-178.

Review

1. Bimodal Nature of Actinide Fission.

T. Ohtsuki, Y. Nagame, H. Nakahara

Heavy Elements and Related New Phenomena, Edited by Walter Greiner and Raj K. Gupta (World Scientific Publishing Co Pte Ltd.) (1999) 507-535.

2. フラーレンをラジオアイソトープでラベルする．炭素第三の同素体：フラーレンの科学.

大槻　勤

季刊化学総説（日本化学会）**43** (1999) 180-181.

VI. Approved Experiments

平成11年度前期採択課題一覧表

課題番号	課　　題　　名	申込責任者	採　択 シフト数
原子核関連分野			
2330	^{12}C(e, e'p)準弾性散乱反応機構の研究	玉江　忠明	18
2332	^{40}Ca(γ, n)反応に於ける２フォノン巨大共鳴励起の探索	寺沢　辰生	10
2333	(e, e'n)テスト実験	斉藤悌二郎	4
放射科学・物性関連分野			
2338	陰イオン交換クロマトグラフィーによるグラム規模のネプツニウム精製システムの開発	山村　朝雄	1
2339	フッ化サマリウム共沈法による低レベルアクチニド核種の測定法に関する研究	三頭　聡明	1
2340	軽元素の光量子放射化分析のための迅速化学分離法の開発	桝本　和義	2
2341	光量子放射化分析法による隕石試料中のハロゲン元素の定量	海老　原充	2
2342	標識化による金属内包フラーレン及びヘテロフラーレンの研究（III）	大槻　　勤	3
2343	軽元素薄膜標準試料の光量子放射化分析	鹿野　弘二	1
2344	中長寿命核種を利用する湖底堆積物の機器光量子放射化分析	輿水　達司	1
2345	水溶性大環状金属錯体固相系における光核反応に伴なう反跳現象の解析とその応用（続）	荘司　　準	1
2346	SiC及び金属における拡散	藤川辰一郎	1
2347	長寿命放射性核種の環境中移行における基礎化学反応研究	関根　　勉	3
2348	水生無セキツイ動物中の金属元素の光量子放射化分析	福島美智子	2
2349	Ｖ系材料の残留放射能に関する研究	塩川　佳伸	1

平成11年度後期採択課題一覧表

課題番号	課題名	申込責任者	採択シフト数
原子核関連分野			
2350	^{10}B (e, e′n)反応の研究	上野　博昭	13
2351	^{12}C (γ, n),^{12}C (γ, np) 反応による光吸収機構の研究	前田　和茂	20
2353	1.1GeV photon tagging systemの開発	山崎　寛仁	20
放射光関連分野			
2355	コヒーレント回析放射を用いたバンチ計測の研究（2）	小山田正幸	8
2356	コヒーレント放射によるオンラインバンチ計測の研究	柴田　行男	6
2357	マイクロバンチFELの出力向上の研究	池沢　幹彦	6
加速器測定器関連分野			
2358	粒子音響検出器の開発研究（2）	樋口　正人	3
放射科学・物性関連分野			
2359	水生無セキツイ動物中の金属元素の光量子放射化分析	福島美智子	2
2360	光核反応 (γ, π^+), (γ, π^-xn), 光核破砕及び光核分裂の放射化学的研究	坂本　浩	2
2361	長寿命放射性核種の環境中移行における基礎化学反応研究	関根　勉	1
2362	光量子放射化分析法による隕石試料中のハロゲン元素の定量	海老原　充	2
2363	軽元素薄膜標準試料の光量子放射化分析	鹿野　弘二	1
2364	軽元素の光量子放射化分析のための迅速化学分離法の開発	桝本　和義	2
2365	Th-229mの製造とその崩壊特性	三頭　聡明	1
2366	水溶性大環状金属錯体固相系における光核反応に伴う反跳現象の研究（続）	荘司　準	1
2367	標識化による金属内包フラーレン及びヘテロフラーレンの研究（継続）	大槻　勤	3
2368	先端材料における拡散	藤川辰一郎	1
2369	ネプツニウム精製システム開発を目的としたイオン交換クロマトグラフィーの過負荷状態の解析	山村　朝雄	1
2370	バイオポリマーを用いた機能性材料の包括固定および核種分離への応用	秋葉　健一	1

核理研研究報告　第33巻

2000年12月発行

発行所　東北大学大学院理学研究科
附属原子核理学研究施設
仙台市太白区三神峯1-2-1（郵便番号982－0826）
電話　022－743－3400

印刷所　株式会社　東北プリント
仙台市青葉区立町24番24号
TEL　022（263）1166㈹

RESEARCH REPORT OF
LABORATORY OF NUCLEAR SCIENCE
TOHOKU UNIVERSITY

Volume 33 December 2000

Laboratory of Nuclear Science, Tohoku University,
1-2-1, Mikamine, Taihaku, Sendai 982-0826, Japan

東北大学大学院理学研究科

原 子 核 理 学 研 究 施 設